

University of Louisville

ThinkIR: The University of Louisville's Institutional Repository

Electronic Theses and Dissertations

12-2016

Strategies and techniques for fabricating MEMS bistable thermal actuators.

Dilan Ratnayake
University of Louisville

Follow this and additional works at: <https://ir.library.louisville.edu/etd>



Part of the [Electronic Devices and Semiconductor Manufacturing Commons](#), and the [Nanotechnology Fabrication Commons](#)

Recommended Citation

Ratnayake, Dilan, "Strategies and techniques for fabricating MEMS bistable thermal actuators." (2016). *Electronic Theses and Dissertations*. Paper 2586.
<https://doi.org/10.18297/etd/2586>

This Doctoral Dissertation is brought to you for free and open access by ThinkIR: The University of Louisville's Institutional Repository. It has been accepted for inclusion in Electronic Theses and Dissertations by an authorized administrator of ThinkIR: The University of Louisville's Institutional Repository. This title appears here courtesy of the author, who has retained all other copyrights. For more information, please contact thinkir@louisville.edu.

STRATEGIES AND TECHNIQUES FOR FABRICATING MEMS BISTABLE
THERMAL ACTUATORS

By

Dilan Ratnayake

B.S., University of Peradeniya, Sri Lanka, 2009

M.S., University of Louisville, KY, USA, 2012

A Dissertation

Submitted to the Faculty of the

J.B Speed School of Engineering of the University of Louisville

in Partial Fulfillment of the Requirements

for the Degree of

Doctor of Philosophy in Electrical Engineering

Department of Electrical and Computer Engineering

University of Louisville

Louisville, Kentucky

December 2016

STRATEGIES AND TECHNIQUES FOR FABRICATING MEMS BISTABLE
THERMAL ACTUATORS

By

Dilan Ratnayake

B.S., University of Peradeniya, Sri Lanka, 2009

M.S., University of Louisville, KY, USA, 2012

A Dissertation Approved on

November 15, 2016

by the following Dissertation Committee:

Dissertation Director: Kevin M. Walsh, PhD

Shamus McNamara, PhD

Gamini Sumanasekera, PhD

Thomas Berfield, PhD

Cindy Harnett, PhD

DEDICATION

This dissertation is dedicated to my parents and my family.

ACKNOWLEDGMENTS

I am most grateful to my advisor and dissertation chair, Dr. Kevin Walsh for his guidance, endless support and patience during past few years. His unique ideas helped me develop some of the most interesting experiments that I got to work on and I am grateful to his for being a continuous source of motivation and inspiration. I believe, the skills that I have learnt from him past few years have largely contributed to making me a better researcher. I am very grateful to Dr. Thomas Berfield, Dr. Shamus McNamara, Dr. Gamini Sumansekera and Dr. Cindy Harnett for being on my committee and giving me valuable feedback on my research project and manuscript over the past four years.

I would like to thank the Micro/Nano Technology Center staff of the University of Louisville for their invaluable help and great teaching experience and for providing me with equipment. Specially, I would like to thank Dr. Julia Aebersold, Dr. Hiren Trada, Curt McKenna, Michael Martin and Don Yeager teaching me the microfabrication inside the cleanroom facility.

Finally, I would like to thank my parents and my brother for their encouragement and guidance. I would not have gone this far in my education if it was not for their encouragement which has been generously given to me since my childhood. I am so thankful to my wife, Roshanthi for all her love, understanding, encouragement and great support given to me throughout my studies. I also want to thank her for giving birth to our lovely princess, Rayani Arya, who is now our family's biggest source of happiness.

ABSTRACT

STRATEGIES AND TECHNIQUES FOR FABRICATING MEMS BISTABLE THERMAL ACTUATORS

Dilan Ratnayake

November 15, 2016

Bistable elements are beginning to appear in the field of MEMS (microelectromechanical systems) as they allow engineers to design sensors and actuators which require no electrical power and possess mechanical memory. This research focuses on the development of novel strategies and techniques for fabricating MEMS bistable structures to serve as no electrical power (NEP) thermal actuators. Two parallel strategies were explored for the design and fabrication of the critical bistable element. Both strategies involved an extensive material study on candidate thin film materials to determine their temperature coefficient of expansion and as-deposited internal stress properties. Materials investigated included titanium tungsten, Invar, silicon nitride and amorphous silicon deposited using either sputtering or plasma-enhanced chemical vapor deposition (PECVD). Deposition parameters were experimentally determined to produce tensile, compressive and stress-free films. A full set of graphs are presented. To address the 3D MEMS topology challenge required for bistability, this research explored two different strategies for fabricating 3D non-planar hemispherical dome structures using minimal processing steps. The first approach used the thermal/chemical reflow of resist, along

with traditional binary lithography with a single photomask. Specific thermal/chemical reflow conditions were experimentally developed to produce hemispherical dome structures over a wide range of diameters from 200 μm to 1100 μm . The second approach introduced a novel maskless procedure for fabricating the dome structures using grayscale lithography. After evaluating the above results, it was decided to use engineered compressive stress in released thin film sandwiches to form the 3D dome structures required for bistable actuation. Three different types of released multi-layer diaphragms were studied: 1) oxide-polyimide diaphragms, 2) oxide-aluminum diaphragms, and 3) oxide-aluminum-polyimide diaphragms. In all three cases, thermally grown oxide was used to form the required compressive layer and backside DRIE was implemented to release the diaphragm. Due to the fragile nature of the thin oxide film, a structural layer was needed to provide mechanical stability and produce uniform unwrinkled domes. Polyimide was determined to be a suitable candidate material for the thick structural layer. Other materials were investigated to serve as the structural layer, such as thick aluminum, but stress related problems were encountered in the thick aluminum films during the high temperature polyimide anneal process. While thick aluminum was unsatisfactory for the structural layer, thin aluminum was found to function well for the required thermal actuation element as long as the actuation temperature was maintained below 150 $^{\circ}\text{C}$. The final design of the thermal bistable switch consisted of 0.45 μm of oxide, 0.3 μm of aluminum, and 1.7 μm of polyimide. Successful thermal actuation was achieved at approximately 100 $^{\circ}\text{C}$ for 400 μm diameter devices. This research also included room temperature and thermal modeling of the buckled structures and determination of regions of bistability versus diaphragm diameter.

TABLE OF CONTENTS

	PAGES
ACKNOWLEDGEMENTS.....	iv
ABSTRACT.....	v
LIST OF TABLES.....	x
LIST OF FIGURES.....	xi
I. INTRODUCTION.....	1
1.1 Inspiration: The “Bimetallic Disc”.....	3
1.2 Background Material on MEMS Bistable Devices.....	6
1.3 Purpose of Dissertation Research.....	9
II. MATERIAL STUDY.....	11
2.1 Titanium Tungsten Films.....	12
2.2 Invar Films.....	13
2.2.1 Elemental analysis.....	14
2.2.2 Stress analysis.....	15
2.2.3 Linear thermal expansion coefficient of invar thin films.....	16
2.3 Silicon Nitride Films.....	19
2.4 Amorphous Silicon Films.....	21
2.5 Discussion and Conclusion.....	22

III.	TOPOLOGY STUDY-FABRICATING THREE DIMENSIONAL STRUCTURES WITH MINIMAL PROCESSING.....	27
3.1	Reflow of Photoresist.....	28
3.1.1	Thermal Reflow.....	29
3.1.2	Chemical Reflow.....	30
3.1.3	Fabrication Process.....	31
3.1.4	Results and Discussion.....	34
3.1.4.1	Thermal Reflow Only.....	34
3.1.4.2	Combining Chemical and Thermal Reflow.....	37
3.2	Grayscale Lithography.....	40
3.2.1	Microstructure Design and Conversion.....	43
3.2.2	Grayscale Lithographic Equipment.....	46
3.2.3	Grayscale Fabrication Process.....	47
3.2.4	Results and Discussion.....	48
IV.	DEVELOPING MEMS BISTABLE ACTUATORS.....	53
4.1	Introduction.....	53
4.2	Buckling Theory for Circular Diaphragms.....	56
4.3	Candidate Materials for the Diaphragm.....	64
4.3.1	Thermal Oxide.....	64
4.3.2	Polyimide.....	69
4.3.3	Aluminum.....	70
4.4	Fabrication Process.....	71
4.4.1	Wafer Cleaning Process.....	73

4.4.2	Thermal Oxidation.....	73
4.4.3	Sputtered Thin Film Deposition.....	75
4.4.4	Polyimide Deposition and Curing.....	77
4.4.5	Photolithography.....	79
4.4.6	Deep Reactive Ion Etch (DRIE).....	82
4.5	Results and Discussion.....	85
4.5.1	Oxide -PI Diaphragms.....	85
4.5.2	Oxide -Al Diaphragms.....	89
4.5.3	Oxide-Al-PI diaphragms.....	99
V.	CONCLUSIONS AND RECOMMENDATIONS.....	104
5.1	Conclusions.....	104
5.2	Recommendations.....	109
	REFERENCES.....	111
	CURRICULUM VITAE.....	121

LIST OF TABLES

TABLE	PAGE
2.1 Process parameters.....	15
2.2 EDAX Quantification.....	15
2.3 Process Settings for PECVD SiN _x Deposition.....	19
2.4 Process Settings for PECVD α -Si Deposition.....	22
3.1 Optimized Lithography Parameters.....	33
3.2 LPG specifications.....	47
4.1 Properties of thermal oxide.....	67
4.2 Optimized spread and spin speeds to produce 1 μ m of Polyimide.....	78
4.3 Optimized spread and spin speed.....	81

LIST OF FIGURES

FIGURE	PAGE
1.1 Trillion sensor vision.....	02
1.2 Final output representation.....	02
1.3 Commercial bimetallic discs.....	05
1.4 Qualitative characteristic of a thermos bimetal snap disc.....	05
1.5 Potential energy vs position showing the concept of bistability.....	06
1.6 (a) Bi-stable MEMS diaphragms fabricated using thermal oxidation, polyimide spinning, and deep reactive ion etching (DRIE). (b) Theory vs. experimental diaphragm deflection to pressure demonstrating a snapping displacement of +/- 35 μm at the center of the 900 μm diameter buckled diaphragm.....	08
1.7 (a) Cross-section of the UofL bi-stable, normally-open, vacuum-actuated, SPST MEMS switch. (b) Switch conductance versus pressure for 4 iterations of vacuum followed by applied pressure. Contact resistance of the switch was less than 200 ohms when closed.....	08
1.8 1 st approach: Overview of the MEMS temperature switch using 3D topology....	10
1.9 2nd approach: Overview of the MEMS temperature switch using buckled diaphragms.....	10
2.1 Stress in sputtered TiW thin films with and without substrate bias.....	13

2.2. The Y-axis shows the counts (number of X-rays received and processed by the detector) and the X-axis shows the energy level of those counts.....	15
2.3 Stress in sputtered Invar thin films with and without substrate bias.....	16
2.4 Invar film deposited on 4" (100) Si.....	18
2.5 Invar film deposited on 4" Quartz.....	18
2.6 Linear expansion coefficient variation with temperature.....	19
2.7 SiN _x Film Stress vs HF Pulse Percentage (at 400°C).....	20
2.8 Stress on SiN _x film vs Pressure with 100% HF.....	21
2.9 Stress on α -Si film vs Temperature.....	22
2.10 Optical image of PECVD amorphous silicon film deposited by breaking vacuum after the SiN _x deposition step (left) and without breaking vacuum (in-situ, right)....	24
2.11 DEKTAK profile of one of the larger PECVD amorphous silicon micro-bubbles deposited on low-stress nitride. Diameter = 134 μ m, height = 7.3 μ m.....	24
2.12 Optical image of amorphous silicon micro-bubbles which were PECVD deposited on low stress silicon nitride after breaking vacuum. Notice the two fractured bubbles in upper left corner of the image exposing underlying nitride layer (left), and SEM of a fractured micro-bubble (right).....	25
2.13 Raman spectra of PECVD amorphous silicon films versus deposited temperature.....	26

3.1 Thermal reflow mechanism between the edges.....	30
3.2 Cross-section of resist structures at increasing bake temperatures (AZ® ECI 3000). Source: AZ-EM® AZ® ECI 3000 Product Data Sheet.....	30
3.3 Features on the photomask (containing circular features from 200µm to 1100µm in diameter).....	32
3.4 Fabrication flow.....	32
3.5 Teflon sample holder.....	35
3.6 Dektak profile of the structure Hot plate: 2 minutes at 150°C.....	34
3.7 Dektak profile of the structure: Hot plate: 1 hour at 150°C.....	35
3.8 Study of profile vs time on a 400 µm diameter disc at a constant temperature of 150 °C.....	36
3.9 Study of profile vs time on 500 µm diameter disc at a constant temperature of 150 °C.....	36
3.10 Combination of chemical and thermal reflow: 700 µm dome exposed to NMP vapor for 3 minutes at 60°C and then placed on a hot plate for 1 hour at 150°C.....	37
3.11 Comparison of the 700 µm dome profile after each critical processing step....	38
3.12 Chemical-thermal reflow.....	38
3.13 Variation of the structure with changing chemical reflow times.....	39

3.14 Comparison between lithographic exposure methods. (a) Traditional (binary) exposure results in completely unaffected photoresist regions, and completely exposed regions; and (b) conversely, grayscale lithography allows for varying UV intensity in each region, resulting in partial photoresist development and allows for generated of complex surface geometry.....	41
3.15 Sample ramp structure (a) and associated grayscale mask file (b). Due to simplicity of structure, mask can be created manually without difficulty.....	42
3.16 Sample dome structure (a) and associated grayscale mask file (b). Due to simplicity of structure, mask can be created manually without difficulty.....	42
3.17 Sample complex structures, (a) and (b), would be difficult if not impossible to manually render grayscale mask files.....	42
3.18 3D microstructure design. Part design in commercially available solid modeling program (SolidWorks) showing modeling of desired structure (hemisphere array) on a simulated silicon wafer substrate (note: units/scale used in part modeling are arbitrary).....	44
3.19 Grayscale conversion software showing mask generation process. Part is saved from solid modeling program as a stereolithography (STL) file, then imported and mask file is rendered.....	45
3.20 (a) Grayscale mask file resulting from the conversion process in and (b) detail of grayscale mask showing 250 nm XY resolution.....	45
3.21 Heidelberg 66FS Laser Pattern Generator.....	46

3.22 (a) Dektak profilometer of the ramp structure (b) Experimental profile vs. the theoretical profile.....	49
3.23 (a) Dektak profilometer of the ramp structure after calibration. (b) Experimental profile vs. the theoretical profile.....	50
3.24 (a) Uncalibrated Dekak profile for the inverted dome structure [9]. (b) Calibrated Dektak profile for the inverted dome structure.....	51
3.25 Dektak profilometer of the dome structure after thermal reflow.....	52
4.1 Formation of buckled diaphragms.....	54
4.2 Thin diaphragm vs. thick diaphragm.....	56
4.3 Cross section of a thin diaphragm loaded with a differential pressure and equilibrium of forces.....	58
4.4 Growth of silicon dioxide by thermal oxidation.....	66
4.5 Contraction of the silicon and the thermal oxide.....	68
4.6 Internal compressive stress of the thermal oxide thin film.....	68
4.7 Non-uniform dome with a wrinkled pattern.....	69
4.8 Mask design contains arrays of circular pattern starting from 100 μm to 700 μm in diameter with 50 μm increment.....	71
4.9 Left side: cross sectional view of the device. Right side: fabrication process flow chart.....	72

4.10 (a) Front view of the three-zone tube furnace (b) Quartz bubbler system for the wet oxidation.....	74
4.11 Summarized temperature profile for the oxidation process.....	75
4.12 Illustration of the sputtering process.....	76
4.13 PVD 75 RF/DC sputtering system from Kurt J. Lesker. Both 3” and 4” targets can be used in the system and it is capable of co-sputtering.....	77
4.14 Spin speed curve.....	78
4.15 Yes Polyimide Oven.....	79
4.16 Temperature profile of the thermal curing process for the PI2610 polyimide....	79
4.17 Suss Mask Aligner MA6/ BA6.....	81
4.18 STS DRIE Etcher.....	83
4.19 Recipe of DRIE for Si etch process.....	84
4.20 Buckling map: shows the buckling direction of released diaphragms.....	85
4.21 Comparison of experimental and theoretical buckling height vs. diaphragm diameter for 0.45 μ m oxide/1.7 μ m polyimide diaphragms. The bistability region labeled in the figure was determined experimentally by applying vacuum to the diaphragms.....	88
4.22 Residual stress and critical stress vs diaphragm diameter.....	89

4.23 Optical image of a buckled diaphragm with a non-uniform wrinkled profile (DIC and brightfield illumination).....	90
4.24 Dome factor vs. diameter of the diaphragm.....	90
4.25 Buckling map: shows the buckling direction of released diaphragms.....	91
4.26 Comparison of experimental and theoretical buckling height vs. diaphragm diameter for .45 μm oxide/.9 μm aluminum diaphragms. Also shown is the experimentally-determined bistability transition point vs. diaphragm diameter.....	92
4.27 Optical images of the buckled diaphragm using DIC and brightfield illumination.....	93
4.28 Optical images of 500 μm and 400 μm in diameter buckled diaphragms using DIC and brightfield illumination.....	94
4.29 Measured stress in the 0.90 μm aluminum film (deposited on top of the oxide) in blue, and the measured stress in the bilayer film (0.45 μm oxide/0.90 μm alum) in red as a function of temperature.....	94
4.30 3 dimensional and cross sectional view of 650 μm oxide/alum diaphragm.....	95
4.31 3 dimensional and cross sectional view of 600 μm oxide/alum diaphragm.....	96
4.32 3 dimensional and cross sectional view of 550 μm oxide/alum diaphragm.....	96
4.33 3 dimensional and cross sectional view of 200 μm oxide/alum diaphragm.....	97
4.34 3 dimensional and cross sectional view of 150 μm oxide/alum diaphragm.....	97

4.35 Stress as a function of temperature for sputtered aluminum.....	98
4.36 Height of the Oxide-Al-PI diaphragm as a function of temperature.....	99
4.37 Profile of the diaphragm (550 μm) at 125°C.....	100
4.38 Comparison of experimental and theoretical buckling height vs. diaphragm diameter for 0.45 μm oxide/0.5 μm alum/1 μm PI diaphragms. Also shown is the experimentally-determined bistability transition point vs. diaphragm diameter.....	101
5.1 Pattern aluminum on the diaphragm.....	107

CHAPTER I

INTRODUCTION

Micro-Electro-Mechanical Systems (MEMS) is the integration of mechanical elements and electronics on a common substrate through microfabrication technology. MEMS devices are typically classified into two categories which are sensors and actuators. A MEMS sensor is a device that when it is exposed to a physical phenomenon (non-electrical input such as temperature, displacement, force, etc.), it produces a proportional output electrical signal. A MEMS actuator is a device that converts electrical power into mechanical motion. These MEMS sensors/actuators can range in size from twenty microns to one millimeter. MEMS application areas include smartphones, tablets, computers, wearables, automobiles, medical devices and industrial control systems.

As shown in Figure 1.1, MEMS sensor absorption in the market exploded from 10 million units in 2007 to 3.5 billion in 2012, and this corresponds to an exponential growth rate of 222% per year between 2007 and 2012 [1]. Few of the research markets and companies expected such growth in 2007. They further estimate 3.5 billion MEMS sensor units exist in 2012, and that will grow to a trillion within the next decade. Figure 1.1 further shows how the different MEMS companies predict the “trillion sensor vision” within the next 10 years. All these MEMS sensors require electrical power for the operation and usually use batteries to provide the required power. If there are a trillion MEMS devices within the next decade, it will require trillions of batteries to provide that

power. Moreover, once the MEMS sensor gives the desired output as an electrical signal, it requires more electronic devices to interpret the signal and produce the final logic output as shown in Figure 1.2. This process may include amplification, signal conditioning, temperature compensation, and filtering.

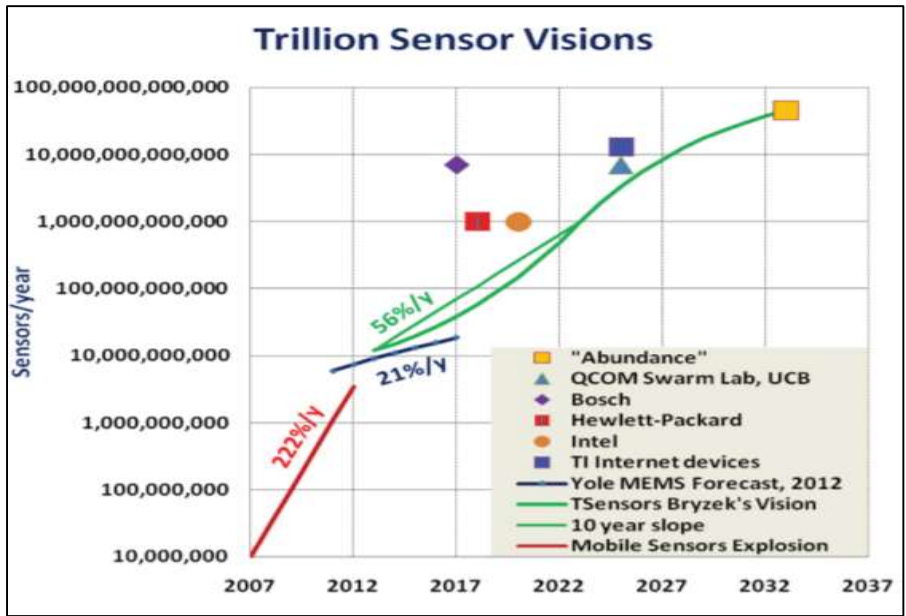


Figure 1.1. Trillion sensor vision [1].



Figure 1.2. Final output representation.

What if the trillions of sensors could be replaced with a new type of inherently smart sensors which consumed zero electrical power and required no electronics to interpret their output and store their data??? That would be a real game changer. These no electrical power (NEP) sensors would result in reduced system complexity and substantial energy savings. The research in this dissertation explores strategies and

techniques for fabricating NEP MEMS sensors. Specifically, we target a no electrical power MEMS temperature switch using bistable thermal actuation.

1.1 Inspiration: The “Bimetallic Disc”

These bimetallic dome-shaped discs are sold as jumping toys on the internet and high quality variations of them are found inside commercial water heater thermostats. In these applications, however, the bimetal discs are very large and formed using traditional alloy-stamping techniques. When the bimetal disc is exposed to a pre-defined temperature, it will change its state from snap up/down to down/up. This phenomenon can be used to create a purely mechanical thermal switch. Note that this device does not require any battery power for operation.

Bimetallic discs with small curvatures have been used as temperature-sensing devices which control elements of thermostatic switches since the middle of the 20th century [2]. Several researchers have been involved in the field of bimetallic shell structures and Timoshenko did an extensive study of the stability of such bimetallic lines and plates[2, 3]. However, the initial explanation of the thermos-elastic stability of a bimetallic disc was presented in a paper by Wittrick in 1953 [2, 4]. Wittrick derived a general theory of the thermos-elastic deformation of a disc and examined the condition for its snap through instability [2, 4]. Furthermore, his mathematical analysis provided the foundation for understanding the operation of a bimetallic disc. He summarized that when the initial central height of the disc is greater than a critical value which is approximately twice the disc thickness, the disc will respond to temperature by changing its state from its 1st stable state to its 2nd stable state at a given temperature [2, 4].

The bimetal thermal disc is truly snap acting and it is commonly known as a “Jumping Disc” because it releases enough mechanical energy when the disc changes its state from one to another to physically jump from a horizontal surface. The bimetallic disc shown in Figure 1.3 is an example of a commercially available non-MEMS snap disk. When the temperature changes slowly from room temperature to some critical temperature value, the disk suddenly changes from its snap down to snap up position.

The commercial non-MEMS bimetallic discs have a diameter of typically 25-30 millimeters and consist of two metal layers bonded together. One layer is made out of invar and referred to as the “passive layer” because of its very low coefficient of thermal expansion (CTE). The second layer is typically made from steel and is called the “active layer” because of its much higher CTE. The two layers are cold-welded together [5]. Invar was developed by the French physicist Charles Guillaume back in 1897 [5] and it is an alloy which has the composition of 36% Ni and 64% Fe. This ferromagnetic face-centered cubic alloy has a very small coefficient of thermal expansion in the wide temperature range between -100°C and +160°C. Since its CTE is almost invariant, the material became known as invar [5].

At low temperatures, these bimetallic discs have a concave shape which then snaps to a convex shape at higher temperatures. As is common in discontinuous phase change materials, the bimetallic disc demonstrates significant hysteresis behavior as shown in Figure 1.4 [5]. These T_{us} and T_{os} are defined the lower and upper snap temperature for the bimetallic disc and those two temperature values provide the sensitivity of the bimetallic disc [5].

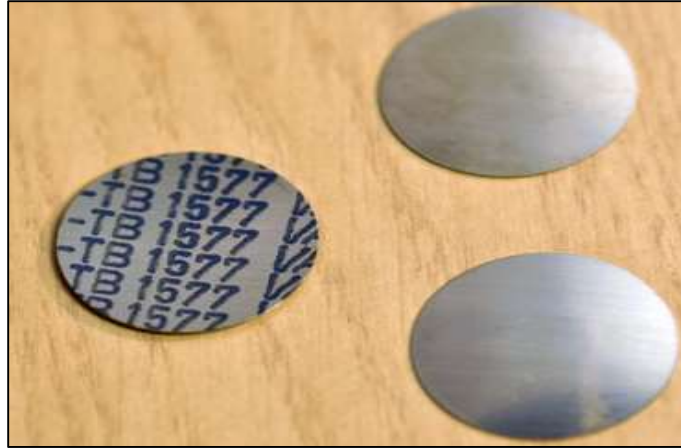


Figure 1.3. Commercial bimetallic discs.

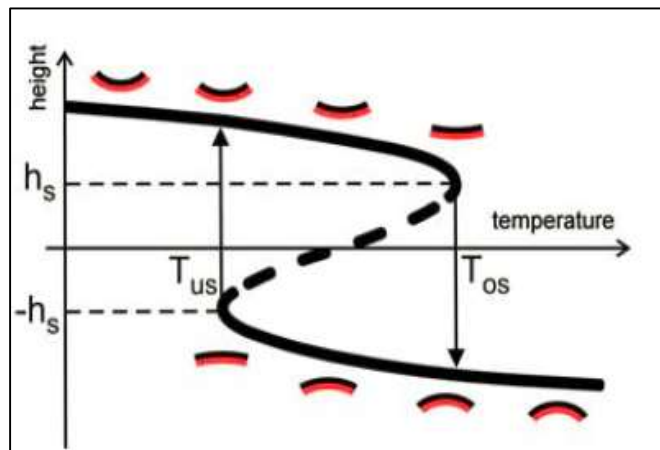


Figure 1.4. Qualitative characteristic of a thermal bimetal snap disc [5].

In this research, we strive to develop a novel microfabrication process for making miniature versions of these thermally-actuated snap discs using MEMS technology. These MEMS bistable disc elements can then be used to design ultra-miniature, low-cost no electrical power thermal switches. The next section provides some background material on bistable devices and their possible embodiment using MEMS.

1.2 Background Material on MEMS Bistable Devices

Bistable devices are all around us from the unique conical auditory hair bundles found in the human ear [6, 7] to the common mechanical wall switches found in homes for turning lights on and off. However, until very recently, bistable structures have not been implemented for miniature mechanical devices and systems. Over the last few years, bistable elements have started to be adopted by the MEMS (micro-electro-mechanical systems) community as they have the potential to serve as building blocks for a new generation of sensors and actuators. A bistable device is similar to a switch in that it can only exist in one of two possible stable states. It remains in that state until it receives enough energy to switch to its other state. In terms of potential energy, a bistable system has two local minima of potential energy which are called its stable equilibrium states. These 2 distinct energy states are separated by a local maximum which is called the unstable equilibrium state, as shown in Figure 1.5. The y-axis represents potential energy and the x-axis represents position. Application of an external stimulus of interest such as heat, vibration, electrostatic, magnetic, force, pressure, etc., can cause the device to switch its states from the 1st stable state to the 2nd stable state. Energy required to switch states can be supplied by the stimulus if the system is designed properly.

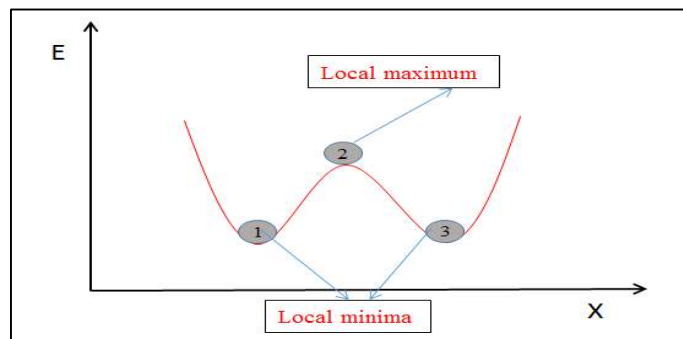
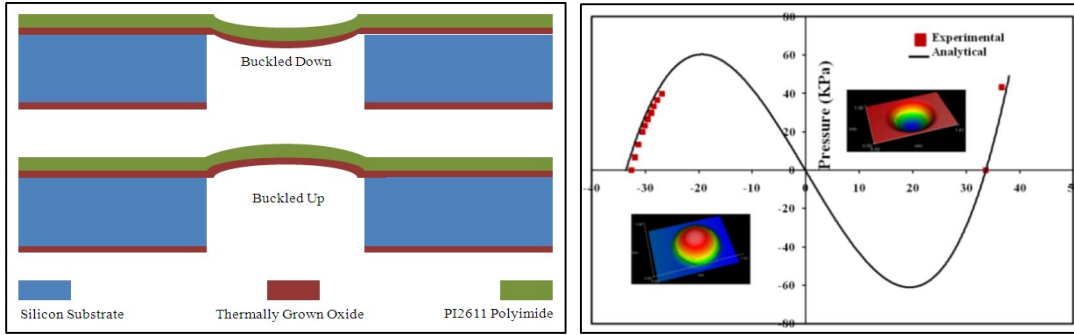


Figure 1.5. Potential energy vs position showing the concept of bistability.

Bistable devices have some unique advantages over their linear non-bistable counterparts. They can be configured as "threshold detection" devices for capturing critical events due to their inherent mechanical hysteresis and store it until the devices can be interrogated later when electrical power is available or convenient. This also allows them to exhibit built-in "non-electronic memory" for mechanically recording and storing important events. If designed properly, they can even be configured as true no-electrical power (NEP) sensors and devices (i.e. battery free). The potential application areas for these novel bistable elements include mechanical switches [8], bistable vibration energy harvesters [9], micro-valves [10], micro-pumps [11], no-electrical-power sensors [12], and mechanical memory elements [13] . Several methods for fabricating bistable structures, such as buckled beams and diaphragms, have been reported in the literature along with proposed actuation methods including electrostatic [14], pneumatic [15], magnetic[16] and thermal means [17].

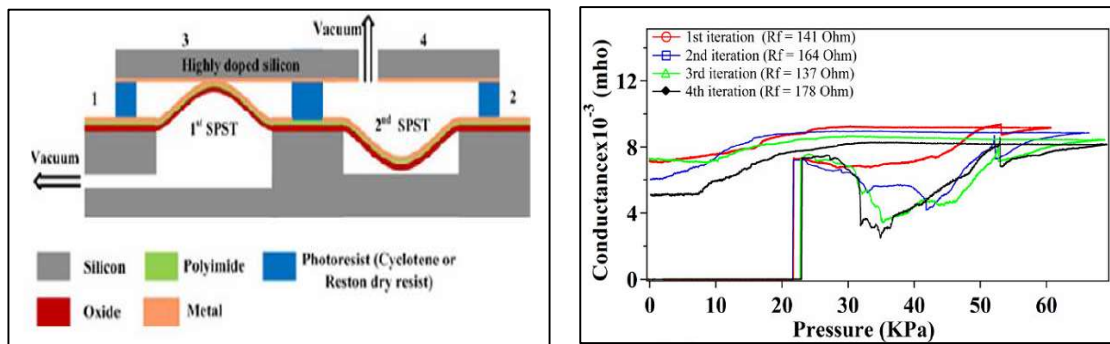
Our research group has been very active in this emerging field. In 2010 we developed a reliable fabrication process for producing buckled circular diaphragms using stress-engineered thermal oxide coupled with low-stress polyimide (PI) for structural enhancement and stability [18]. The cross-section of that device is illustrated in Figure 1.6 (a), along with its bistable deflection to applied pressure (Figure 1.6 (b)). In 2010, we used a similar process to fabricate a no-electrical power, bistable, pressure-actuated SPST (single pole single throw) MEMS switch as shown in Figure 1.7 (a) and demonstrated its performance under variations of applied vacuum and pressure (Figure 1.7 (b)) [19]. In 2012, we published a paper demonstrating how our PI/oxide buckled diaphragms could serve as the heart of an energy harvesting device [20].



(a)

(b)

Figure 1.6. (a) Bi-stable MEMS diaphragms fabricated using thermal oxidation, polyimide spinning, and deep reactive ion etching (DRIE). (b) Theory vs. experimental diaphragm deflection to pressure demonstrating a snapping displacement of +/- 35 μm at the center of the 900 μm diameter buckled diaphragm [19].



(a)

(b)

Figure 1.7. (a) Cross-section of the UoFL bi-stable, normally-open, vacuum-actuated, SPST MEMS switch. (b) Switch conductance versus pressure for 4 iterations of vacuum followed by applied pressure. Contact resistance of the switch was less than 200 ohms when closed [19].

1.3 Purpose of Dissertation Research

The purpose of this dissertation research is to design, fabricate and test strategies and techniques for fabricating MEMS bistable dome-shaped thermal actuators. Such elements can be used as the building blocks for ultra-miniature, low-cost no electrical temperature switches. These elements have various applications NEP sensors, actuators, switches, and thermal energy harvesting devices. The dissertation research can be divided into three areas as follows.

- I. Investigate interesting candidate materials for engineering stress in thin films for potential use as bistable elements.
- II. Explore different strategies and approaches for fabricating MEMS 3D non-planar structures using minimal processing steps.
- III. Design, fabricate, and test a bistable MEMS buckled diaphragm which will change its state (buckled up/down) upon the application of a set temperature and compare experimental results to the theoretical predictions.

Section 1 and 2 involve intensive research developing processes for fabricating bimetallic discs using MEMS technology. Various fabrication strategies are explored for making three-dimensional dome-shaped structures, including resist reflow, grayscale lithography and engineered compressive stress in thin films. Material properties of candidate thin films are determined and assessed for application to our research goals.

Figure 1.8 presents a schematic of a possible design of a MEMS-based NEP thermal switch implementing a center anchored disc. Figure 1.9 presents an alternate design approach using a thermal disc anchored along its perimeter.

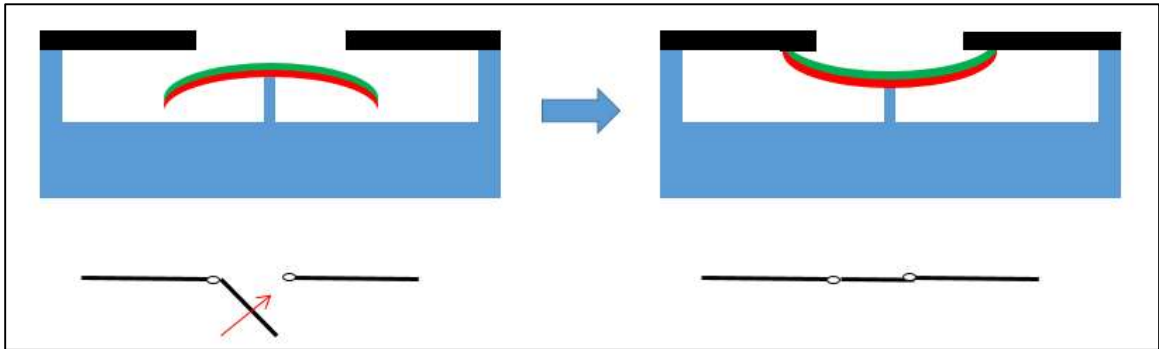


Figure 1.8. Possible design for a MEMS-based thermal switch using a center anchored disc.

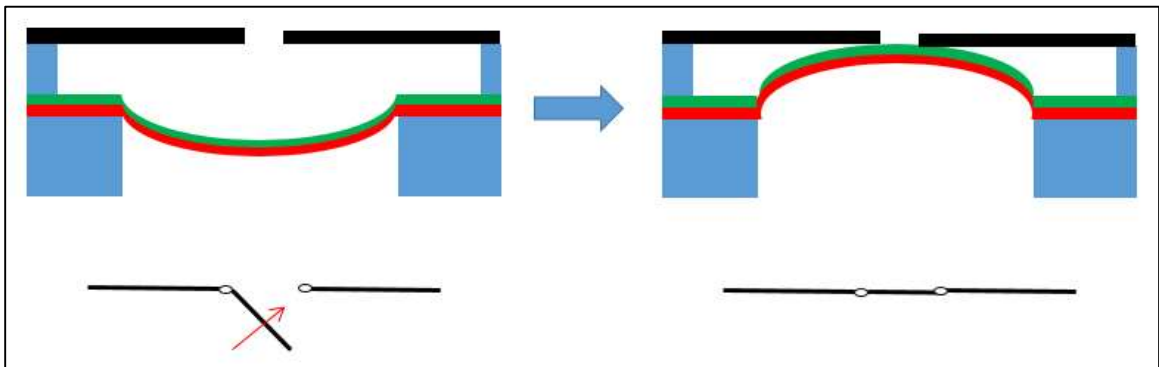


Figure 1.9. Alternative design of a MEMS-based thermal switch using a disc anchored along its perimeter.

CHAPTER II

MATERIAL STUDY

In this chapter, I investigate more interesting candidate materials for engineering stress in thin films for potential use as bistable elements. Specifically, I report on using sputtering and PECVD (plasma enhanced chemical vapor deposition) techniques for controlling stress in deposited thin films.

Since most MEMS devices are fabricated from layers of silicon combined with electrically conductive and insulating films, we selected the following materials to study: titanium tungsten, invar, silicon nitride and amorphous silicon. Titanium tungsten (TiW) was chosen because it is a good conductive layer and can also be used as an adhesion layer for other metals. Invar was selected because it can be utilized as an effective passive layer (i.e. low CTE) in thermally actuated MEMS devices. Silicon nitride was selected because it is a common MEMS insulating layer and it also serves as an excellent adhesion layer for amorphous silicon. Finally, amorphous silicon was selected because it is a common form of silicon deposited using PECVD and sputtering equipment. In all of our experimental investigations, 100 cm diameter (100) n type Si wafers (4-10 Ω cm) were used as the starting substrates. They were cleaned using the traditional industry-standard RCA1 and RCA2 cleaning procedures [21]. The initial wafer bow was measured using a laser-based Toho Thin Film Stress Measurement System (KLA Tencor FLX-2320, USA). Each wafer was measured at four different angles (0°, 45°, 90° and 135°) before any thin film deposition. Then the candidate films were

deposited onto the top surface of the wafers and the bow measurements were repeated. From those data, the internal stresses of the deposited thin films were calculated using the supplied Toho software which is based upon the Stoney equation[22]. Additional material characterization was performed for the invar, which includes examining the composition of the sputtered invar thin films and the coefficient of thermal expansion. The thickness of the candidate films was measured using either a Dektak Profilometer or a Filmetrics Thin Film Measurement System.

2.1 Titanium Tungsten Films

It is well known that the thin film stress of sputtered metal layers can be tuned by adjusting the kinetic energy of arriving neutral metal atoms so that at lower sputter pressures (and higher kinetic energy) the film becomes more compressive [23, 24]. Essentially, the film becomes denser and contains fewer voids at lower sputter pressures. A similar effect can be achieved by providing a small substrate bias (either RF or DC) during the deposition so that Ar ions bombard the substrate (not the target) with sufficient energy to allow metal atoms and clusters to “walk” on the surface until surface defects are found to fill. In particular the intrinsic film stress of TiW is known to be readily adjustable from roughly +1000MPa tensile to -2000 MPa compressive by changing the Ar pressure during sputter deposition from 2 mTorr to 20 mTorr [24].

In this work, sputtering was used to deposit the thin-films of TiW from a 4” diameter target composed of 10% Ti and 90% W. Sputtering was performed with a PVD 75 RF/DC Sputtering System from Kurt J. Lesker. For all experiments the power was 300W DC and the deposition time was 20 minutes while the pressures were varied. In some experiments a capacitively coupled RF substrate bias was used at 20W which produced a

DC bias of 277V at 3mTorr, 270V at 5mTorr and 107V at 2 mTorr due to poor coupling. Figure 2.1 shows our results with and without substrate bias. With no bias, we were able to vary the film's stress from approximately -300 MPa to +1500 MPa consistent with findings in the literature. However, with bias we could further control stress from -1300 MPa to -2300 MPa. The addition of the substrate bias allowed compressive stresses to be tuned into the films, which is the basic requirement for thin film buckling when released. To our knowledge, this is the first time a stress characterization curve for TiW has been published with a substrate bias. In general, this method allows one to adjust film stress at relatively higher pressures thus enabling deposition of compressive TiW films at higher deposition rates. Additionally, many capacitively coupled sputtering systems are not capable of sustaining plasmas at such low pressures (<5 mTorr) therefore substrate biasing allows the manipulation of TiW film stress at less challenging pressures.

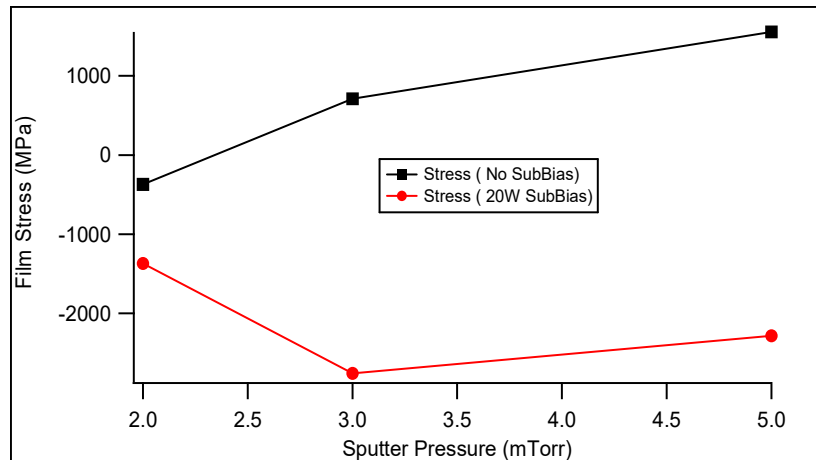


Figure 2.1. Stress in sputtered TiW thin films with and without substrate bias [25].

2.2 Invar Films

Invar was developed by the French physicist Charles Guillaume in 1897 [5] and consists of an alloy which has the composition of 36% Ni and 64% Fe. The advantage of this

ferromagnetic face-centered cubic alloy is that it has a very small and invariant coefficient of thermal expansion (CTE) in the temperature range between -100°C and $+160^{\circ}\text{C}$, thus the reason for its name [5]. Invar thin film deposition studies have been previously reported using electroplating [26, 27], but very little research was found in the literature on invar thin films using sputtering[28]. The goal of this section is to perform a comprehensive study on sputtered invar thin films, focusing on the chemical composition, analyzing the stress and the coefficient of thermal expansion of sputter-deposited invar thin films.

2.2.1 Elemental analysis

In this research a 4" invar sputtering target was purchased and the invar thin film was deposited on a 100 mm diameter (100) Si wafer using the same Kurt Lesker PVD 75 RF/DC sputtering system as discussed above. Table 2.1 shows the process parameters used and the corresponding deposition rates. Elementary analysis was performed using EDX (Energy Dispersive X-ray analysis) to verify the invar thin film composition that was sputtered on the silicon wafers. The results are shown in Figure 2.2. The Si peak is due to the substrate. Table 2.2 presents the material composition of the deposited film without considering the Si composition due to silicon substrate. However, the composition of Ni and Fe are slightly different compare with common grades of bulk invar which has 36% Ni and 64% Fe. Additionally, elementary analysis shows a small amount of oxygen (3.55%) content, and since it is a thin film, we assume this oxygen is due to contamination with the air.

Table 2.1. Process parameters.

DC/RF	Power (W)	Pressure (mTorr)	Thickness (μm)	Time (min)	Deposition Rate(nm/min)
DC	300	5	0.750	60	12.5

Table 2.2. EDAX Quantification.

Element	Weight %
Fe	54.95
Ni	41.50
O	3.55
Total	100

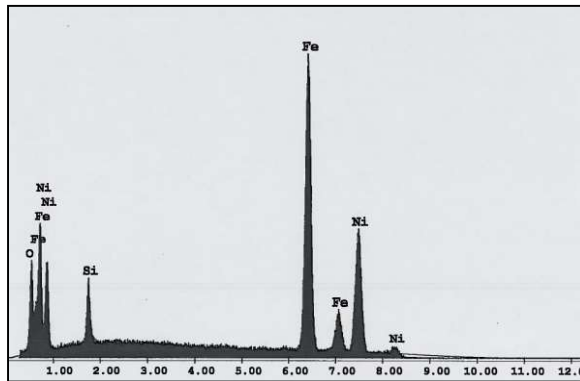


Figure 2.2. The Y-axis shows the counts (number of X-rays received and processed by the detector) and the X-axis shows the energy level of those counts.

2.2.2 Stress analysis

The same procedure that was used to deposit TiW thin film was used to deposit sputtered Invar thin films. For all experiments the power was 300W DC and the deposition time

was 20 minutes while the pressures were varied from 2 mTorr to 5 mTorr. In some experiments a capacitively coupled RF substrate bias was used at 20W which produced an average DC bias of 280V to produce a denser film. As shown in Figure 2.3, the application of a 20W substrate bias resulted in more film stress variation with chamber pressure. Without substrate bias, it was not possible to tune compressive stress into the films. This combination of deposition with and without bias allows one to create invar films ranging from -1600 MPa to +300 MPa, providing much latitude with the MEMS design of bistable and non-bistable structures.

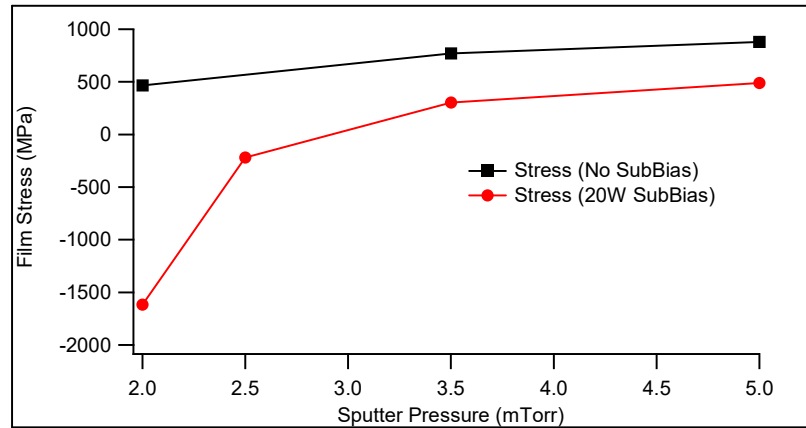


Figure 2.3. Stress in sputtered Invar thin films with and without substrate bias [25].

2.2.3 Linear thermal expansion coefficient of invar thin films

Stress in the film can be measured by a laser-scanning method which measures substrate curvature. The stress in the thin film can then be calculated from the experimentally-determined radius of the curvature of the substrate using the Stoney formula as shown in equation 2.1 [29] as follows,

$$\sigma = \frac{Eh^2}{(1-\nu)6RT} \quad 2.1$$

where $E/(1 - \nu)$ is the biaxial elastic modulus of the substrate, h is the substrate thickness, T is the film thickness, R is the substrate radius of the curvature, and σ is the average film internal stress. The stress change with temperature in the elastic range is governed by the following equation [28].

$$\frac{d\sigma}{dT} = \left(\frac{E}{1-\nu}\right)_f (\alpha_s - \alpha_f) \quad 2.2$$

where, $\frac{d\sigma}{dT}$ is the derivative of the stress vs. temperature, $\left(\frac{E}{1-\nu}\right)_f$ is the biaxial modulus of the films, α_s is the substrate thermal expansion coefficient, α_f is the film thermal expansion coefficient. This equation has two unknowns, α_f and $\left(\frac{E}{1-\nu}\right)_f$. These two unknowns can be determined if the film is deposited on two different types of substrates and then stress is measured by varying the temperature (i.e. heating the substrate). Silicon and quartz were selected for the substrates. An invar thin film was then sputtered on top of the 100 mm (100) Si wafer and the 100 mm quartz wafer using the same processing conditions. A KLA-Tencor FLX-2320 Stress Analysis System was used to measure the stress on the films through curvature measurements. To solve for these unknown quantities, two temperature cycles were performed with two different substrates and the KLA software solved the two equations to find the CTE of the thin film. Figure 2.4 and Figure 2.5 show the stress variation on the invar film with temperature. Temperature was increased from 32°C to 120°C and 2.6°C/min and -2.6°C/min ramp rates were used for the heating and cooling cycles.

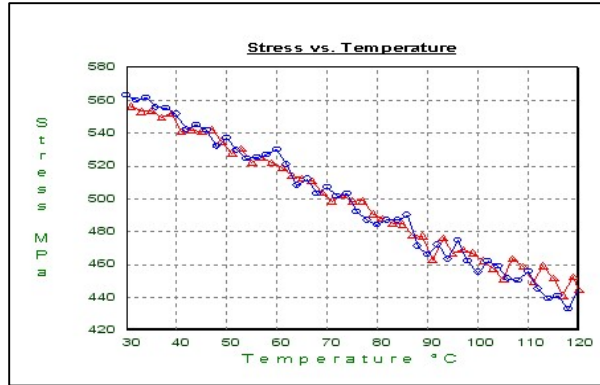


Figure 2.4. Invar film deposited on 4'' (100) Si [30].

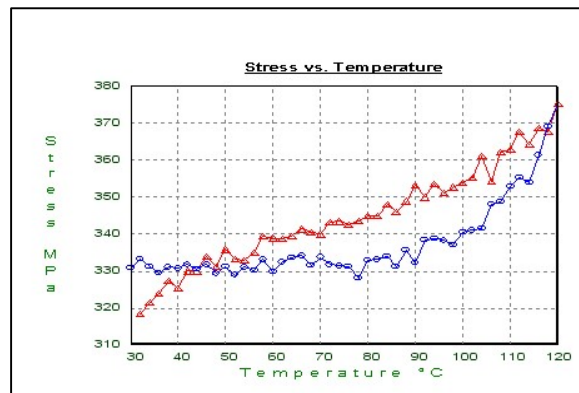


Figure 2.5. Invar film deposited on 4'' Quartz [30].

Then these two graphs were used by the KLA software program to determine the CTE variation with temperature as shown in Figure 2.6. This produces an experimental CTE average for sputter-deposited invar to be 1.376ppm/°C. This was an encouraging result as it is competitive with published values for bulk invar. Common grades of bulk invar have a coefficient of thermal expansion of about $1.2 \times 10^{-6} \text{ K}^{-1}$ (1.2 ppm/°C) measured between 20°C and 100°C, while ordinary steels have values of around 11–15 ppm/°C [31]. We expected our experimental value for sputter-deposited invar to be different as the properties of thin films are commonly different from their bulk values.

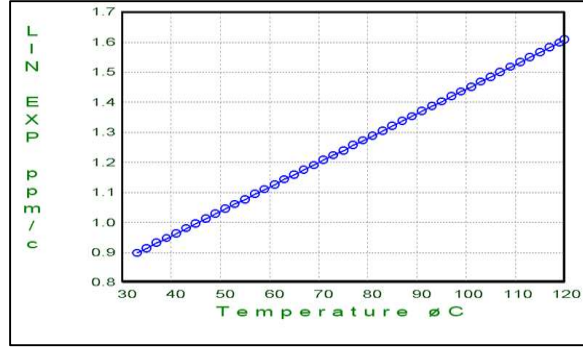


Figure 2.6. Linear expansion coefficient variation with temperature [30].

2.3 Silicon Nitride Films

An Oxford PECVD System 100 using silane and ammonia was used to deposit silicon nitride films. The films were deposited onto a 100 cm silicon (100) wafers as before.

The details of the process settings are presented in Table 2.3.

Table 2.3. Process Settings for PECVD SiN_x Deposition

Material	Parameters								
	SiH ₄ 5% in Ar (sccm)	NH ₃ (sccm)	N ₂ (sccm)	LF Power(W)	HF Power(W)	Pressure (mTorr)	Time (minutes)	Temperature (°C)	Thickness (nm)
SiN _x	20	20	600	20	20	650	15	400	~130

The stress on the nitride films were controlled by changing the high frequency (HF) pulse time in dual frequency mode as described in equation 2.3.

$$HF \text{ Pulse } \% = \frac{HF \text{ Pulse Time}}{(LF \text{ Pulse Time} + HF \text{ Pulse Time})} 100\% \quad 2.3$$

where HF refers to high frequency (13.56MHz) and LF refers to low frequency (100-350 kHz). Figure 2.7 shows the stress on the SiN_x film verses HF pulse percentage. As seen in the figure, it is possible to produce a near stress-free film (i.e. less than -20MPa) using

an 85% HF pulse recipe. Note that this recipe will be used in the next section for producing a thin stress-free adhesion layer of silicon nitride which is needed for PECVD-deposited amorphous silicon.

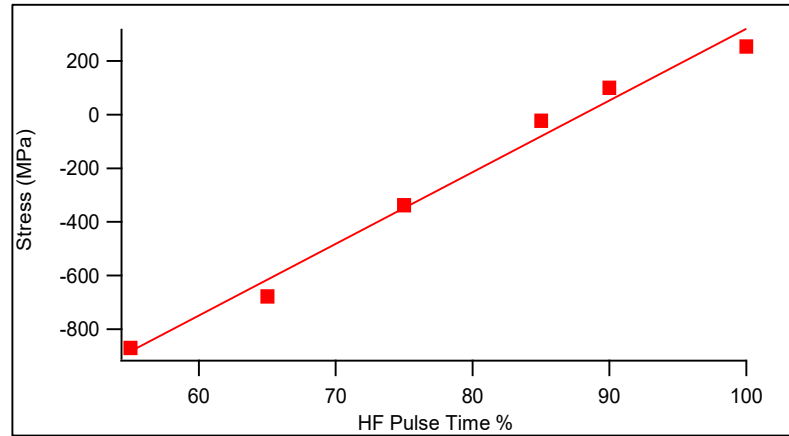


Figure 2.7. SiNx Film Stress vs HF Pulse Percentage (at 400°C) [25].

A second experiment was performed to observe how deposition pressure effects the stress on the nitride film. In this series of experiments, the high frequency was operated continuously (i.e. HF Pulse % = 100%). Figure 2.8 presents the results illustrating a very linear dependence of silicon nitride film stress on chamber pressure, with the interesting ability to tune the internal stress of the deposited films from tensile to stress-free to compressive. The results in this section illustrate how the internal stress of PECVD-deposited silicon nitride films can be readily adjusted using either HF % or chamber pressure. While these results have never been published for our deposition tool, similar results exist for other PECVD equipment. However, we needed to perform these experiments in order to determine how to deposit stress-free PECVD silicon nitride which is needed in the next section.

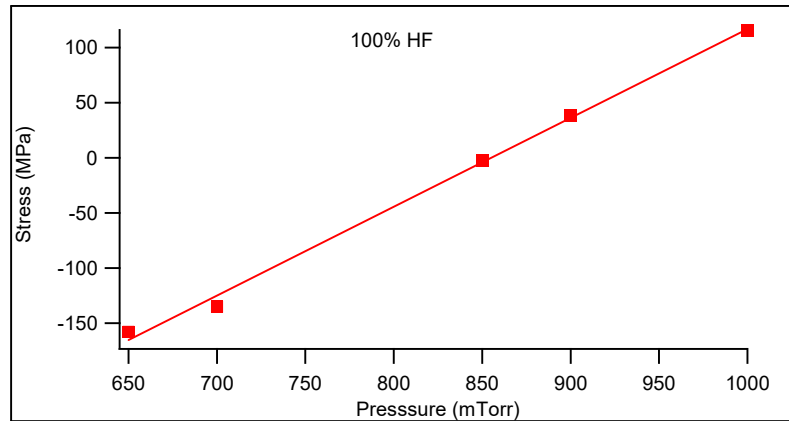


Figure 2.8. Stress on SiNx film vs Pressure with 100% HF [25].

2.4 Amorphous Silicon Films

Amorphous silicon (α -Si) is a popular deposition material for MEMS and very little has been published regarding methods to effectively tune its internal stress properties for various non-traditional MEMS applications. For our experiment, undoped amorphous silicon was selected deposited using PECVD. Specifically, the film's stress variation versus deposition temperature was investigated. Since amorphous silicon is known to show poor adhesion to bare silicon, it is traditionally deposited onto a SiO_x or $SiNx$ underlayer to improve adhesion [32, 33]. We did, however, explore the possibility of depositing amorphous silicon directly onto bare silicon, but that resulted in very weak adhesion and the formation of "micro bubbles" in the deposited films (see next section for images and further discussion). To overcome that problem, a stress-free film of silicon nitride was first deposited on the silicon substrates using the parameters extracted from the previous section. Then amorphous silicon films were deposited using the same PECVD system. The deposition temperature was varied from 150°C to 300°C. A summary of the deposition parameters are shown in Table 2.4. The stress on the film was measured and the results for the undoped amorphous PECVD silicon are graphed in

Figure 2.9. Interestingly, we were able to obtain a nice linear range for internal stress versus deposition temperature, ranging again from tensile films to compressive films. Near zero-stress α -Si films were obtained at a deposition temperature of 225°C (average tensile stress was ~ 3.33 MPa). The compressive films are excellent candidates for buckled bistable MEMS structures.

Table 2.4. Process Settings for PECVD α -Si Deposition

Material	Parameters					
	SiH4 5% in Ar (sccm)	HF Power(W)	Pressure (mTorr)	Time(mi nts)	Temperature (°C)	Thickness (nm)
α -Si	25	7	1000	30	150-300	~ 700

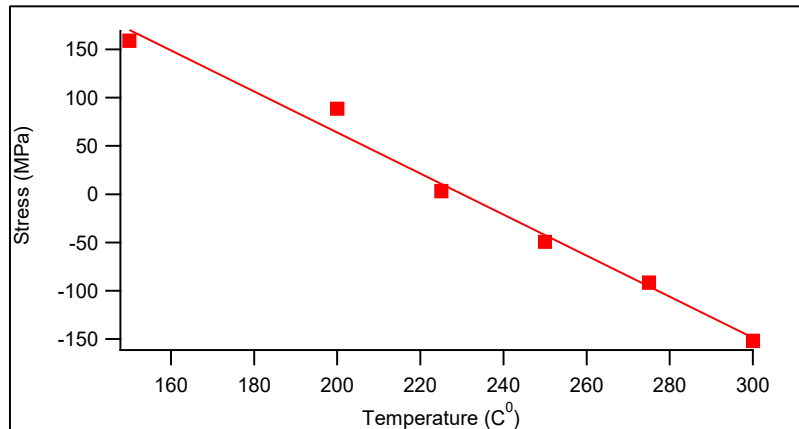


Figure 2.9. Stress on α -Si film vs Temperature [25].

2.5 Discussion and Conclusion

As stated in the previous section, during the amorphous silicon study, some issues surfaced with the quality of the films when PECVD α -Si was deposited directly onto bare silicon. Specifically, two problems were encountered. The deposited films demonstrated poor adhesion to the substrates and failed the traditional "tape test"[34-37]. When a strip

of adhesive tape was pulled from the film, it delaminated from the substrate. The second problem was with its morphology as the film contained a large density of raised hollow "micro-bubbles" ranging in size from 60 μm microns to 140 μm microns. The formation of such bubbles has been previously reported in the literature and has been attributed to trapped hydrogen gas unable to escape [38-40]. It is logical to think that both problems are somewhat related, as poor adhesion can provide regions on the surface for hydrogen to accumulate. To eliminate this problem, a thin layer of stress-free silicon nitride was deposited prior to the amorphous silicon. This eliminated the formation of the hollow micro-bubbles as long as the nitride and $\alpha\text{-Si}$ deposition were done in-situ (without breaking vacuum). When the $\alpha\text{-Si}$ was deposited after breaking vacuum (which we initially had to do to verify that the nitride film was indeed stress-free using the Toho Measurement System), the micro-bubbles reappeared when the compressive stress of the $\alpha\text{-Si}$ exceeded -90 MPa ($\geq 275^\circ\text{C}$ deposition temperature). This was attributed once again to poor adhesion between the compressive $\alpha\text{-Si}$ film and the cleaned nitride film which had been exposed to atmosphere. To test this hypothesis, the same experiment was repeated without breaking vacuum between the nitride and $\alpha\text{-Si}$ depositions (i.e. in-situ). The adhesion between the two films improved tremendously and the hollow micro-bubbles disappeared. Also supporting our hypothesis was the fact that the in-situ deposition passed the traditional "tape test", while the film deposited while breaking vacuum failed. A comparison of the two films is shown in Figure 2.10 using DIC optical microscopy (500x). The left side of the figure shows representative micro-bubbles obtained when breaking vacuum between depositions. The right side presents results when performed in-situ. The micro-bubbles ranged in diameter from 60 μm to 140 μm

with typical heights of 3 μm to 7.5 μm . The density of the micro-bubbles was approximately 5 bubbles/ mm^2 . The average roughness of the two surfaces, as measured by an AFM, was 16 nm RMS for the in-situ film and 667 nm RMS when breaking vacuum. Figure 2.11 presents a Dektak image of a typical hollow micro-bubble with a diameter of 134 microns and a height of 7.3 microns. If a controllable process could be developed for the formation of these interesting three-dimensional structures, they could be used to fabricate bistable elements. To prove that the micro-bubbles were in fact hollow and not an accumulation of excess amorphous silicon as claimed in [32], some of them were intentionally fractured with a probe tip and imaged optically and using an SEM. These results are shown in Figure 2.12 and illustrate that there are hollow.

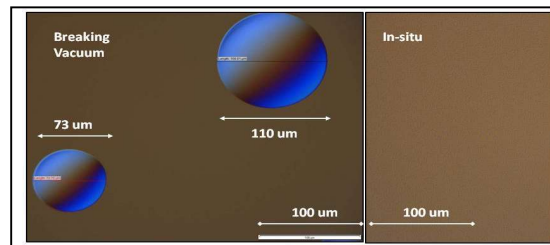


Figure 2.10. Optical image of PECVD amorphous silicon film deposited by breaking vacuum after the SiN_x deposition step (left) and without breaking vacuum (in-situ, right) [25].

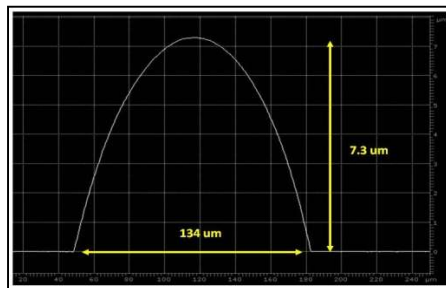


Figure 2.11. DEKTAK profile of one of the larger PECVD amorphous silicon micro-bubbles deposited on low-stress nitride. Diameter = 134 μm , height = 7.3 μm [25].

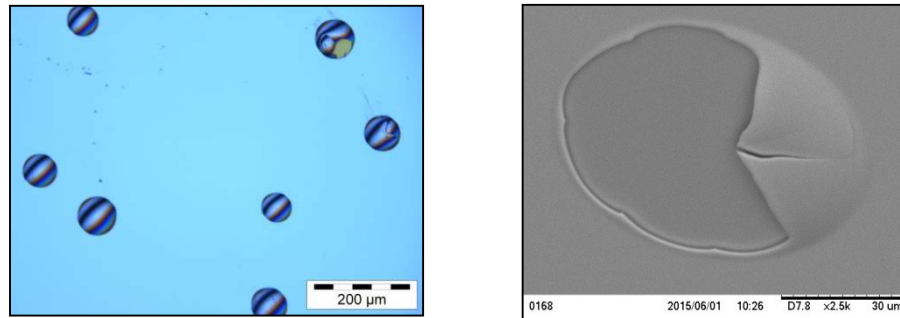


Figure 2.12. Optical image of amorphous silicon micro-bubbles which were PECVD deposited on low stress silicon nitride after breaking vacuum. Notice the two fractured bubbles in upper left corner of the image exposing underlying nitride layer (left), and SEM of a fractured micro-bubble (right) [25].

In summary, this chapter reports on various deposition techniques for engineering the internal stress in candidate thin film materials for producing buckled bistable MEMS structures. Sputtering with and without substrate bias provided an excellent deposition technique for titanium tungsten and Invar. In both cases, the addition of a substrate bias provided a convenient means to greatly increase the compressive stress in the films, which is a desirable characteristic when fabricating mechanically bistable elements. Elementary analysis of the experimental Invar thin film provided a similar but not an exact match to the bulk target which was 64% Fe and 36% Ni. However, the coefficient of thermal expansion of the invar thin film compared favorably with that of bulk invar. This demonstrated that sputtered invar thin films can be used as candidate materials for the “passive” layer in bistable MEMS thermal sensors and actuators. For controlling the internal stress of amorphous silicon and silicon nitride, PECVD deposition was explored. With amorphous silicon, it was demonstrated that the stress could be controlled by

varying the substrate temperature. Raman spectroscopy was used to verify that the films were indeed amorphous as shown in Figure 2.13. The sharp peak at 520 cm^{-1} is due to the silicon wafer substrate and the broad peak around 480 cm^{-1} is an indication of the amorphous PECVD silicon films [41]. With silicon nitride, the stress was controlled by either varying the HF/LF duty cycle or by varying the chamber pressure. Both strategies allowed for a full range of stress values to be obtained in the thin films - ranging from tensile to stress-free to compressive.

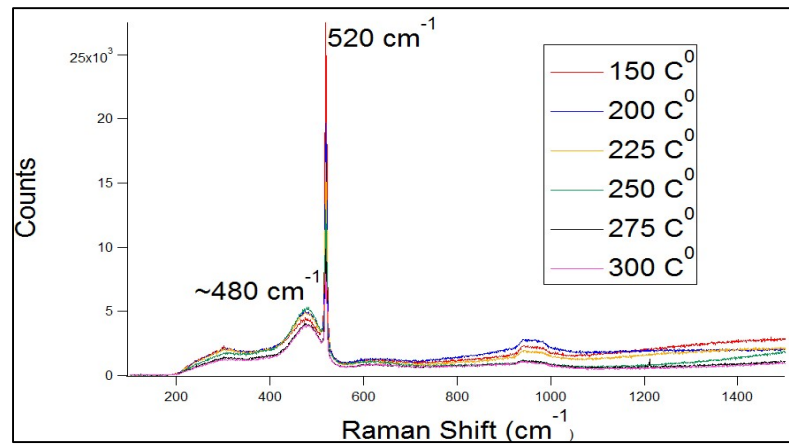


Figure 2.13. Raman spectra of PECVD amorphous silicon films versus deposited temperature[25].

CHAPTER III
TOPOLOGY STUDY-FABRICATING THREE DIMENSIONAL STRUCTURES
WITH MINIMAL PROCESSING

Integrated circuits (ICs) are considered 2.5 dimensional devices because they are fabricated using the top surface of a silicon wafer. As such, ICs typically utilize only the top 5-10% of the silicon wafer volume. The remainder of the silicon material is required to mechanically handle the wafer. If the silicon wafers were cut to only the thickness of the transistors, they would be physically too thin and fragile to handle. Therefore, most of an ICs volume is in the X and Y directions with only a small amount in the Z direction, thus the rationale for naming them 2.5 dimensional devices. In contrast, MEMS (microelectromechanical systems) devices, such as sensors and actuators, are truly three-dimensional (3D) structures requiring the fabrication of non-planar elements. To create three-dimensional structures in silicon, researchers have traditionally relied on combinations of wet etching, dry etching, thin film deposition, wafer-level bonding and electroplating to create interesting non-planar structures. However, designing and fabricating 3D structures in this fashion can be limiting, time-consuming, and/or very expensive. A new approach to producing non-planar structures using either a single fabrication step or the minimal number of fabrication steps is needed. One interesting non-planar element which has proven very difficult to fabricate on the micro-scale has been the hemispherical dome. This element is especially useful for the fields of optics and bistable MEMS.

While it is possible to produce a hemispherical dome using a series of thin film depositions followed by their patterning, this is an extremely time-consuming and costly strategy. It is considered impractical and therefore rarely used. Using the classical hemispherical dome as a case study, this chapter explores different strategies and approaches to fabricating this 3D non-planar structure using the minimal steps possible. The first approach uses thermal/chemical reflow and traditional binary lithography with a single photomask. The second approach introduces a novel maskless procedure for fabricating the dome and essentially any MEMS 3D structures using grayscale lithography. Both methods are presented below.

3.1 Reflow of Photoresist

In this part of the study, we investigate our first method for producing micro-scale dome structures quickly and economically. We began by examining the literature on micro-fabricated lenses, as that is the general shape of our desired micro-scale dome structures. Many experiments have previously been conducted to produce micro-lenses using different processing techniques such as ion exchange [42], pneumatically diaphragm-driven drop-on-demand inkjet technology [43], and thermal reflow of photoresist [44-46]. The reflow of photoresist strategy is the most widely known and successful process according to the literature. Researchers have used this process to prototype micro-lenses for many applications such as optical interconnections, optical communication, and imaging systems [47]. Most of these fabricated micro-lenses using reflowed resist are in the range of less than 200 μm in diameter. This study explored the possibility of applying the thermal reflow strategy to fabricate much larger rounded dome features using a combination of both thermal and chemical reflow. Both involve a single photomask

using standard binary lithography. We anticipate that the combination of thermal and chemical reflow will allow one to fabricate any size (based on diameter and height) of rounded dome features by controlling the parameters such as spin/spread RPM, thermal reflow temperature and time, and chemical reflow time. Details are provided in the next sections.

3.1.1 Thermal Reflow

The viscosity of photoresist decreases rapidly at temperatures above the glass transition temperature [48]. The material flows because of surface tension, while remaining coherent. The flow of such a low-viscosity material across a substrate is described by the Navier–Stokes equation [46]:

$$\rho \left(\frac{\partial \vec{v}}{\partial t} + \vec{v} \cdot (\nabla \vec{v}) \right) = -\nabla p + \mu \nabla^2 \vec{v} + \vec{f} \quad 3.1$$

where;

\vec{v} = flow velocity, $\nabla \vec{v}$ = tensor derivative of \vec{v} , ρ = fluid density, p = pressure

μ = fluid viscosity, and f = external force

Reflow of the photoresist takes place at temperatures beyond the glass transition temperature, at which the resist becomes soft and starts flowing on the substrate due to surface tension. This approach for reflow is known as “thermal reflow”. Figure 3.1 shows how the geometry of the initial cylindrical shape of the resist changes with the raising temperature. When the temperature reaches the melting point of the resist, the resist becomes soft which helps to create a rounded shape. Figure 3.2 shows the cross sectional

view of an actual resist structure that undergoes the changes with increasing bake temperature.

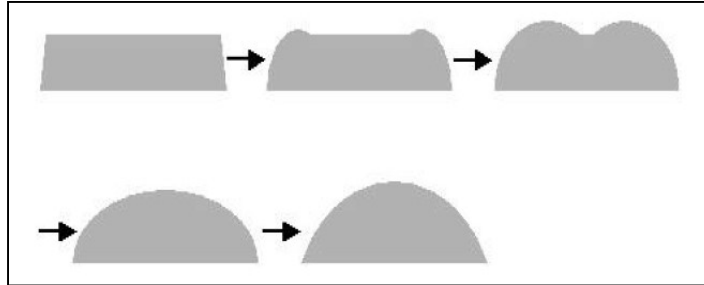


Figure 3.1. Thermal reflow mechanism between the edges.

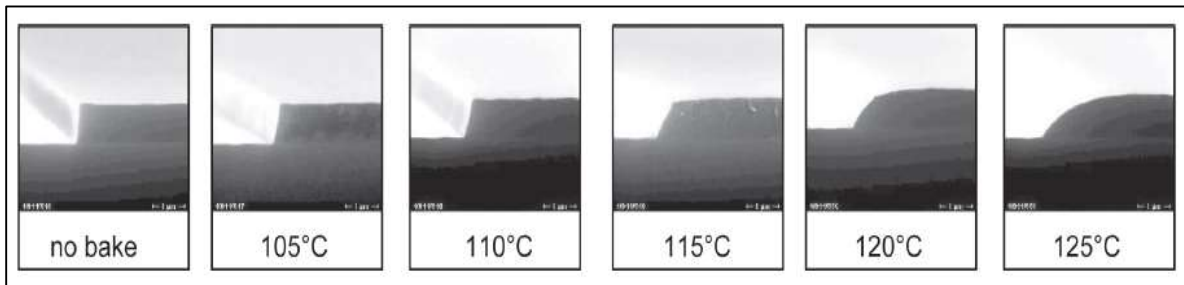


Figure 3.2. Cross-section of resist structures at increasing bake temperatures (AZ® ECI 3000). Source: AZ-EM® AZ® ECI 3000 Product Data Sheet.

3.1.2 Chemical Reflow

When the sample is exposed to the vapor of a solvent, photoresist absorbs the solvent resulting in a very soft substance, which flows easily over the substrate. This methodology for resist reflow is known as “chemical reflow”. It is possible to use a combination of thermal and chemical reflow to produce a variety of interesting non-planar three-dimensional features.

3.1.3 Fabrication Process

AZ4620 photoresist was used for all the following experiments. First, the photoresist was spun onto a 4" silicon wafer using a Headway spinner, and its spread and spin parameters were modified to produce a 10 μ m thick resist layer. Then a soft bake was performed for 10 minutes at 100°C on a hotplate, which is below the glass transition temperature of the AZ 4620 resist. Standard binary lithography was performed using a MA6/BA6 Suss Mask Aligner, which provides the UV light for exposure. The photomask contains arrays of circular features from 200 μ m to 1100 μ m in diameter, as shown in Figure 4.3 (200 μ m, 300 μ m, 400 μ m, 500 μ m, 600 μ m, 700 μ m, 800 μ m, 900 μ m, 1000 μ m, 1100 μ m). Once the sample was exposed to UV light, AZ 400k developer was used to develop the exposed structures into cylindrically-shaped structures on the bare silicon wafer. The optimized lithography parameters are given in Table 3.1. AZ 400k developer is supplied as a concentrate. The standard high contrast make-up provides optimum resolution and contrast as well as maximum processing latitude [49]. The standard high-speed dilution results in very high production throughput [49]. Therefore, AZ 400k was diluted with DI water in a 1:4 ratio to develop the structures. Then, the wafer was rinsed in a QDR (Quick Dump Rinse) unit followed by SRD (Spin Rinse Dryer). Next, these patterned structures were exposed to thermal and chemical reflow. Figure 3.4 provides an overview of the fabrication flow. The thermal reflow was performed by placing the sample on top of a hot plate at 150°C, which is above the glass transition temperature of AZ4620 resist. The chemical reflow process was performed by placing the sample (a sample holder was created using Teflon as shown in Figure 3.5) inside a beaker of NMP (N-Methyl-2-

pyrrolidone) at 60°C so that it absorbed the NMP vapor. Finally, a Veeco Dektak 8M Profilometer was used to characterize the profile of the structures.



Figure 3.3. Features on the photomask (containing circular features from 200 μm to 1100 μm in diameter).

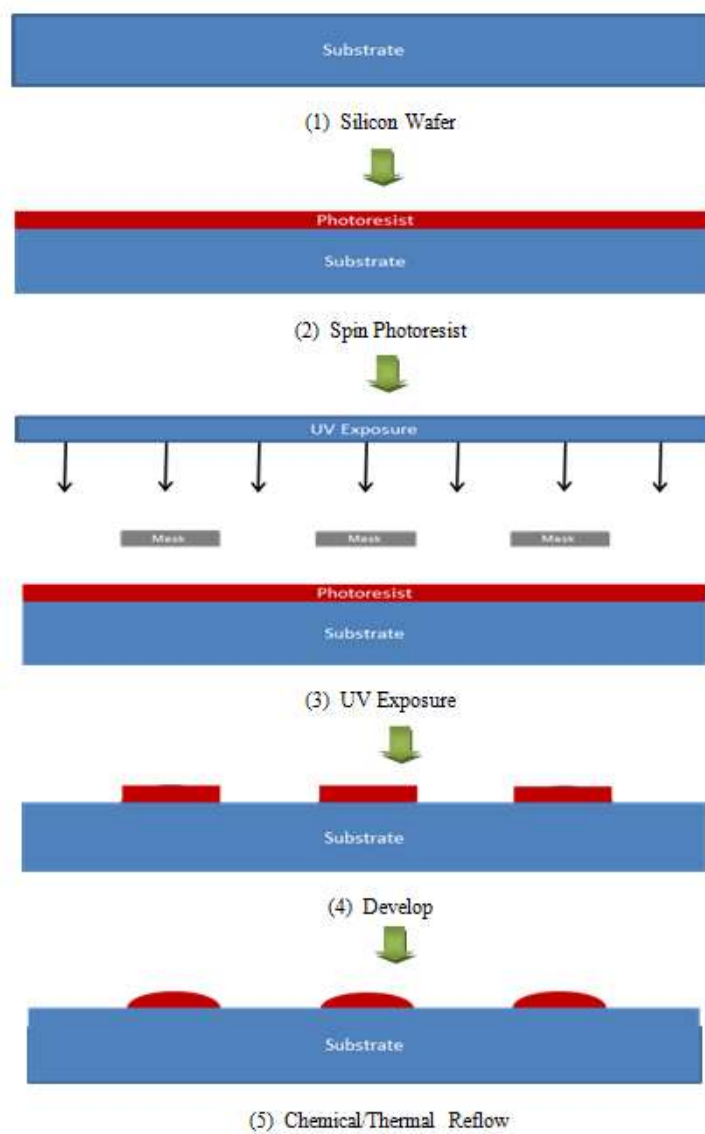


Figure 3.4. Fabrication flow.

Table 3.1. Optimized Lithography Parameters.

Description	Equipment	Condition
Dehydrate Wafers	Hot Plate	115°C for 10 mints
Spin on AZ P4620	Headway Spinner	Spread: 500RPM for 5s Spin: 2000RPM for 30s
Soft bake	Hot Plate	100°C for 10 minutes
Exposure	SUSS MASK ALIGNER MA6/ BA6	70s
Develop	Pan	AZ400K 4:1 until clear
Rinse in DI H2O	Quick Dump Rinse	3 cycles
Dry with N2	Spin Rinse Dryer	

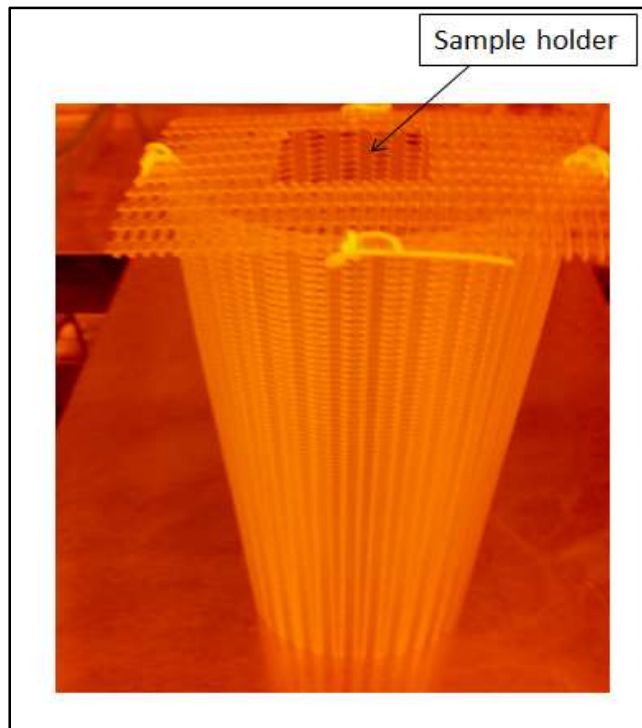


Figure 3.5. Teflon sample holder

3.1.3 Results and Discussion

3.1.3.1 Thermal Reflow Only

Once the fabrication process was completed as described above, the profile of the structures were inspected using the Dektak profilometer. In the first part of the experiment, only thermal reflow of the resist was used for all the samples. Figure 3.6 shows the profile of the array of structures after annealing them on a hotplate at 150 °C for two minutes. Figure 3.7 shows the same except for an anneal time of one hour. Note that 150 °C is above the glass transition temperature of the AZ 4620 photoresist. As shown in the 2 figures, only the 1st two structures were converted to domes. This corresponded to structures with diameters of 400 μm and less. Figure 3.7 also demonstrated that extending the anneal time from 2 minutes to 60 minutes produced little effect, except for smoothing out the profile a bit. However, the extended bake time did not result in dome conversion for the larger diameter profiles. We even extended the anneal time to 15 hours, but no improvement was noted.

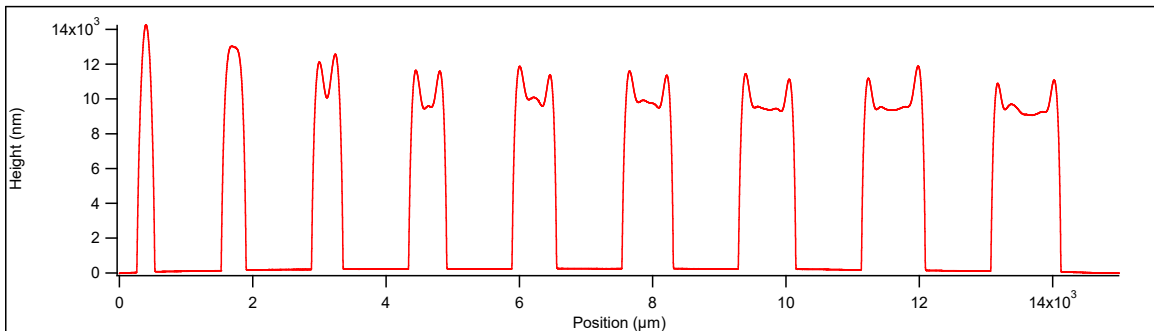


Figure 3.6. Dektak profile of the structure Hot plate: two minutes at 150°C.

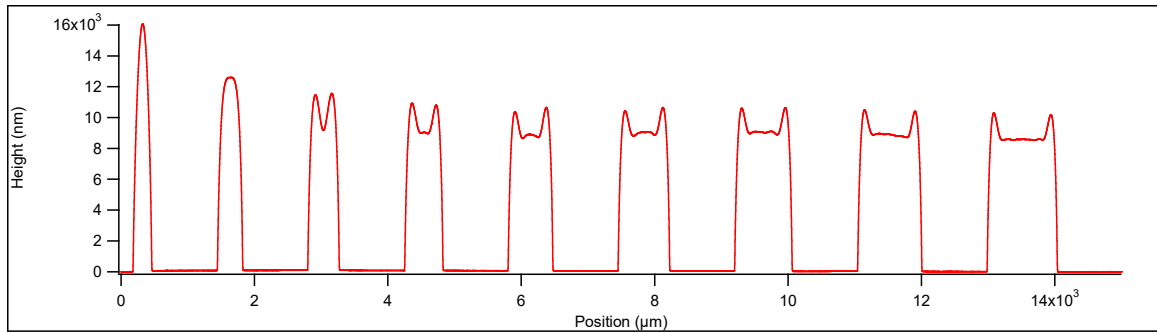


Figure 3.7. Dektak profile of the structure: Hot plate: 1 hour at 150°C.

Figure 3.8 presents the results of a more detailed study of the temperature effects on a 400 μm diameter structure. Here the structure was exposed to anneal times of 2 min, 30 min, 1 hr, 2.5 hrs, and 5 hrs. As seen from the data, the 400 μm structure was converted into a dome in approximately 30 min. Further anneal time provided little improvement in the shape of the dome, but did decrease the dome's height slightly.

Figure 3.9 presents the results of the same reflow study performed on a 500 μm diameter structure of resist. As shown in the profile data, even the extended anneal times were unsuccessful in converting the disc of resist into a dome. Only a smooth double humpback profile was achievable with the reflow process. This was due to the structure's larger diameter. This result is consistent with other results presented in the literature [46]. The basic problem is the relatively large diameter of our structures, as this process works for structures in the range of 400 μm or less [45], but was ineffective for the larger discs.

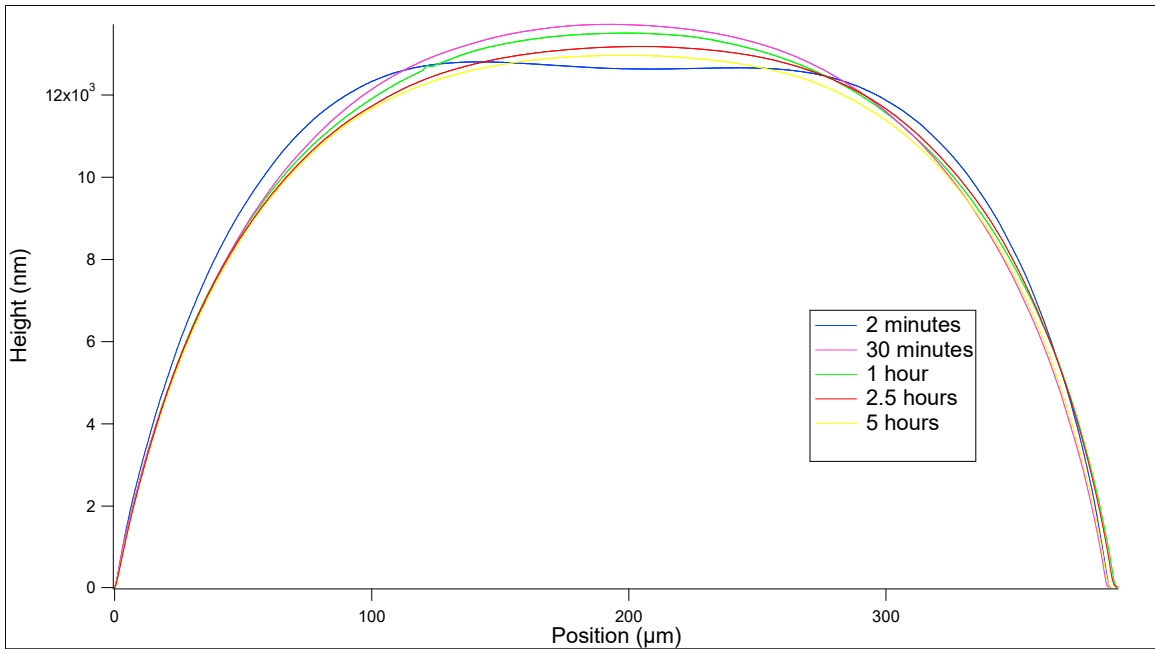


Figure 3.8. Study of profile vs time on a 400 μm diameter disc at a constant temperature of 150 $^{\circ}\text{C}$.

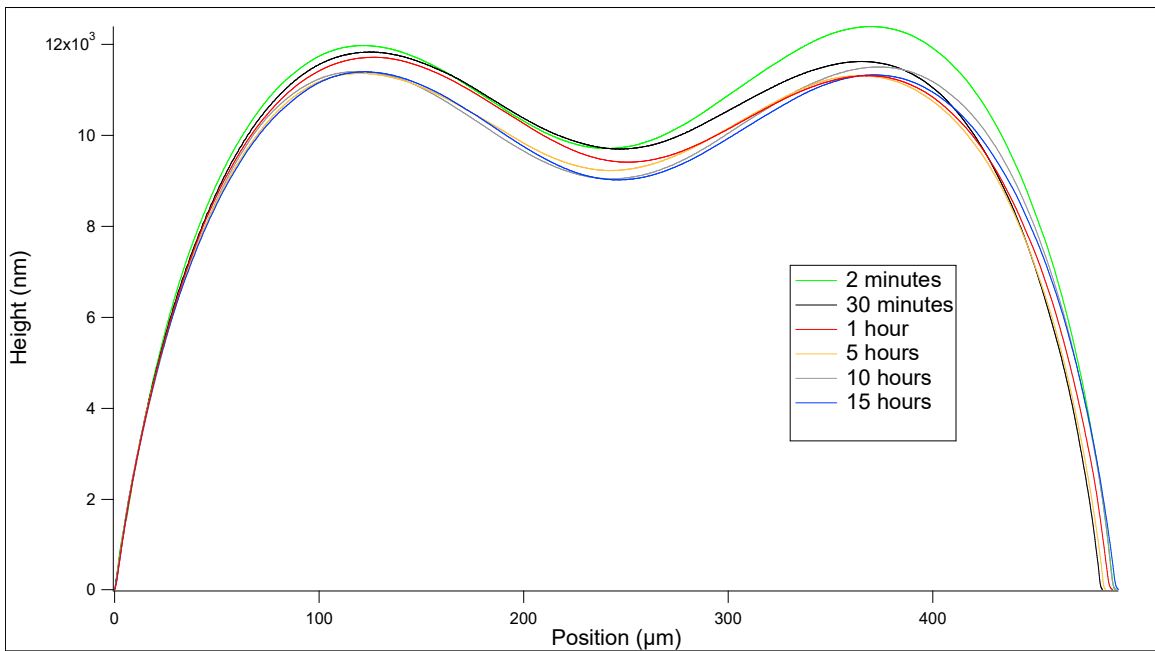


Figure 3.9. Study of profile vs time on 500 μm diameter disc at a constant temperature of 150 $^{\circ}\text{C}$.

3.1.3.2 Combining Chemical and Thermal Reflow

As a solution, we decided to combine chemical reflow with thermal reflow to see if it was possible to create the large diameter dome features which were needed for our bistable MEMS applications.

Our overall processing strategy was as follows: Chemical reflow was initially introduced to soften the photoresist using NMP as discussed in sections 3.1.2 and 3.1.3 followed by heat exposure for thermal reflow using a hot plate. After several experiments, we were able to identify combinations of the two processes which would successfully convert large diameter discs of resist into nice dome structures, as illustrated in Figure 3.10. This figure shows our results for a large 700 μm diameter of resist after it was exposed to NMP vapor for three minutes at 60°C and then placed on a hot plate for one hour at 150°C. Figure 3.11 compares the profile of the 700 μm structure after each critical processing step – a) after developing, b) after thermal reflow only, and c) after chemical reflow. What began as a 700 μm diameter disc of resist with an initial height of 10.1 μm was converted through our thermal-chemical reflow process into a dome of resist with a diameter of 792 μm and height of 9.2 μm .

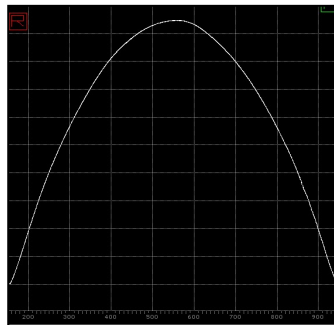


Figure 3.10. Combination of chemical and thermal reflow: 700 μm dome exposed to NMP vapor for three minutes at 60°C and then placed on a hot plate for 1 hour at 150°C.

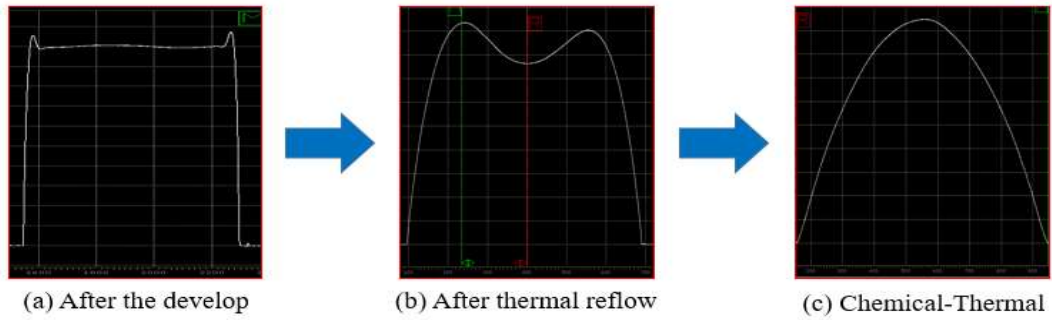


Figure 3.11. Comparison of the 700 μm dome profile after each critical processing step.

Next we exposed the entire array of varying diameter structures to the NMP vapor followed by thermal reflow. Figure 3.12 presents the profiles of selected array elements after exposure to NMP vapor for four minutes followed by thermal reflow at 150 $^{\circ}\text{C}$ for one hour. As seen in the figure, domed structures were obtained with the large diameter devices, but when the starting diameter was less than 800 μm , nice domes were not produced. Instead those profiles have flat tops instead of being curved.

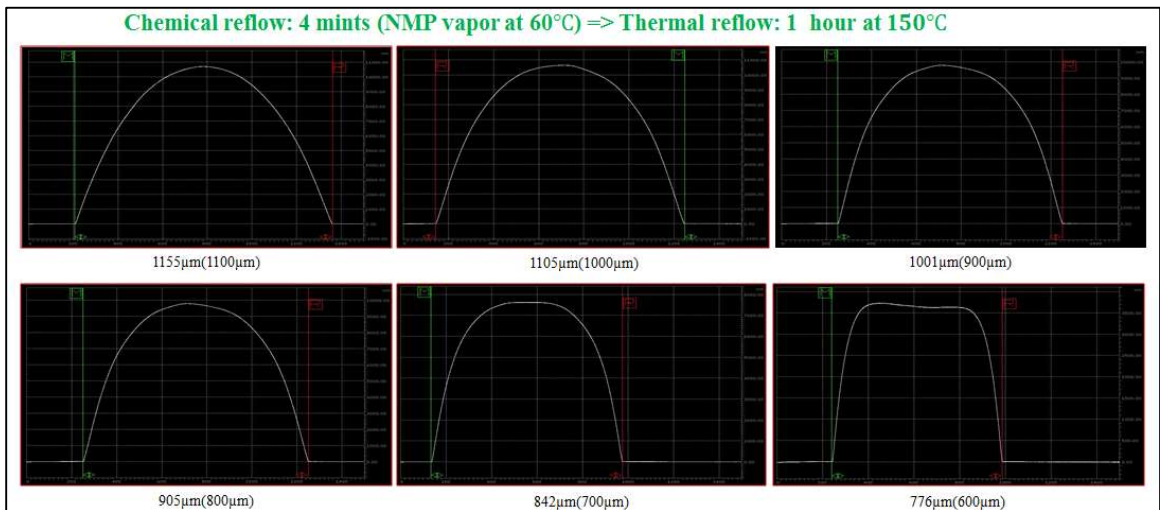


Figure 3.12. Chemical-thermal reflow.

Finally, in Figure 3.13 we varied the NMP exposure time from 4 min to 3 min to 2 min, keeping everything else constant. As one can observe, four minute exposure produced nice dome profiles for the large diameter structures (1100 μm , 1000 μm , 900 μm and 800 μm), three minute exposure produced nice results for the medium diameter structures (700 μm , 600 μm , and 500 μm), two minutes produced nice results for the smaller structures (500 μm and 400 μm), and structures with 200 μm and 300 μm in diameter do not require the chemical reflow process.

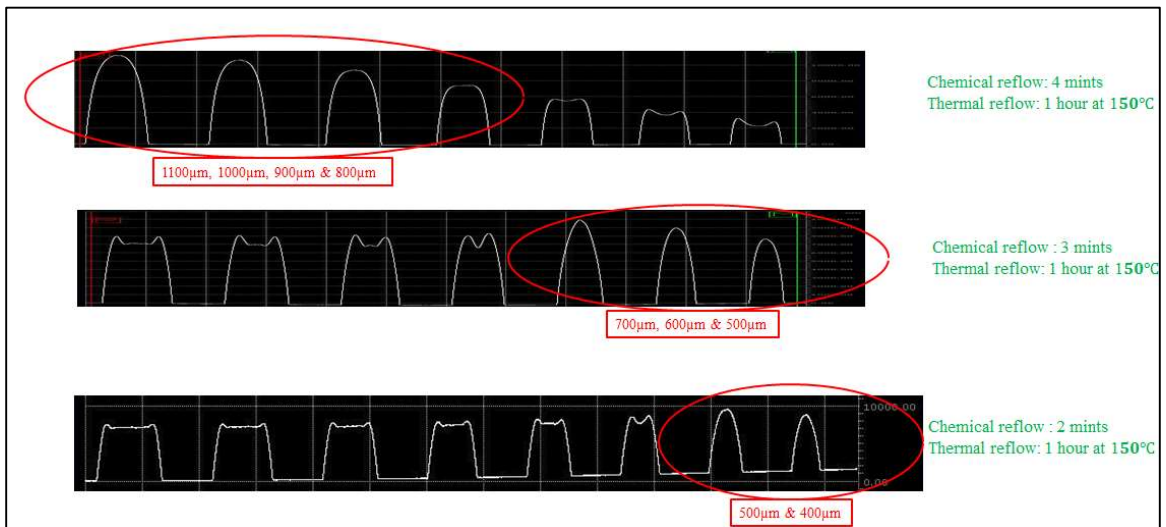


Figure 3.13. Variation of the structure with changing chemical reflow times.

3.2 Grayscale Lithography

The second strategy we explored for fabricating 3D dome structures used grayscale lithography. The concept of grayscale lithography has been around for a while, but it is a relatively underutilized process. The unique advantage of grayscale lithography is that it allows one to theoretically produce an infinite number of three-dimensional structures in photoresist using a single step [50]. As opposed to standard binary lithography (where the photoresist film is either completely exposed or completely shielded from the ultraviolet (UV) illumination), grayscale lithography allows one to modulate the UV intensity spatially, resulting in partial photoresist exposure and development. This allows one to generate complex surface geometries, as shown in Figure 3.14. Grayscale lithography presents an interesting method of generating complex surface geometry from a single lithographic exposure using microfabrication equipment presently available rather than stacking hundreds of planar films on top of one another to approximate the complex geometric shape. The latter approach is prohibitively expensive and time-consuming.

The main disadvantage of grayscale lithography involves the time-intensive creation of mask files required to generate complex 3D microstructures. According to our literature review, grayscale masks used in LPGs (Laser Pattern Generators) must be created manually, resulting in severe limitations on design complexity and limiting overall usefulness. For example, minimum exposure region size is equipment specific, but typically $250 \text{ nm} \times 250 \text{ nm}$ pixels are possible with 128 levels of UV intensity in z direction (that is the development depth). Therefore, to fabricate a $100 \text{ }\mu\text{m} \times 100 \text{ }\mu\text{m}$ structure on a LPG with 250 nm resolution and 128 intensity steps, an operator would have to create a mask file with up to 1.6×10^6 elements and calculate desired height (thus

exposure intensity or layer number) for each element. For simple shapes such as a single ramp as shown in Figure 3.15 or a dome as shown in Figure 3.16, mask files are relatively straightforward and mask generation software (for example L-Edit) can be used. In more complex structures, however, such as those shown in Figure 3.17, manual creation of mask files is not feasible. Furthermore, if many iterations of a design are desired, an automatic mask generation technique is important [50]. This requires the development of a fast automated process for producing mask files with complex 3D surface geometry.

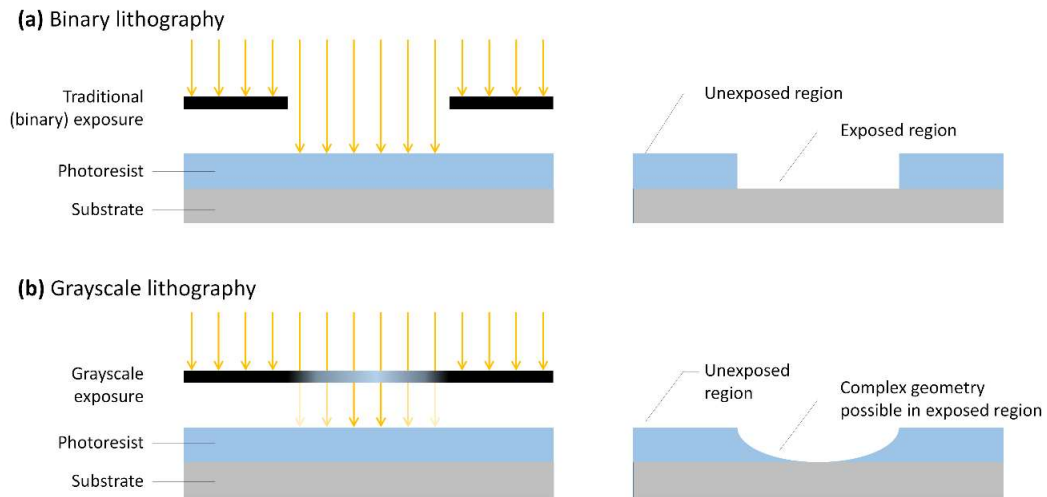


Figure 3.14. Comparison between lithographic exposure methods. (a) Traditional (binary) exposure results in completely unaffected photoresist regions, and completely exposed regions; and (b) conversely, grayscale lithography allows for varying UV intensity in each region, resulting in partial photoresist development and allowing for generated of complex surface geometry.

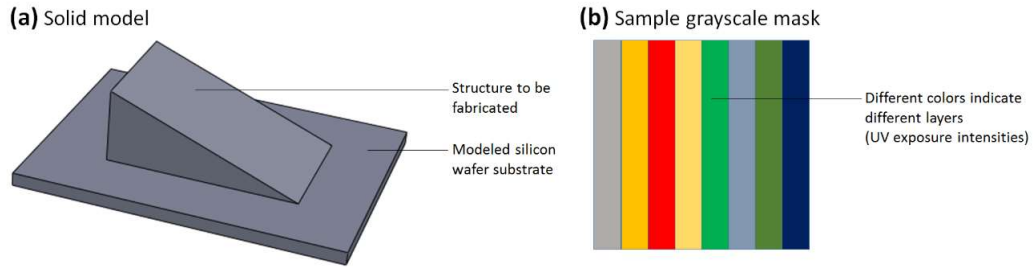


Figure 3.15. Sample ramp structure (a) and associated grayscale mask file (b).
 Due to simplicity of structure, mask can be created manually without difficulty.

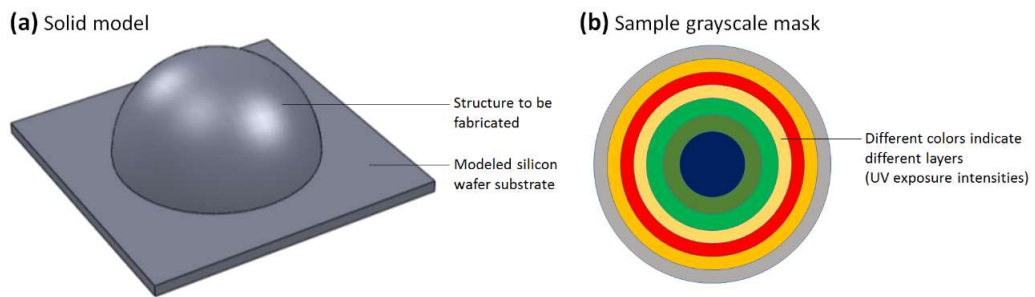


Figure 3.16. Sample dome structure (a) and associated grayscale mask file (b).
 Due to simplicity of structure, mask can be created manually without difficulty.

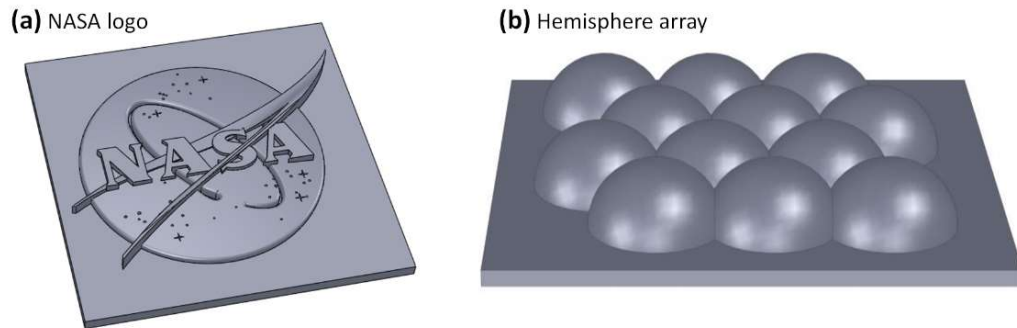


Figure 3.17. Sample complex structures, (a) and (b), would be difficult if not impossible to manually render grayscale mask files.[50]

3.2.1 Microstructure Design and Conversion

This section discusses a custom process for fabricating MEMS 3D structures using grayscale lithography. A conversion software [3], which was developed by our research group member (Dr. James Loomis), was used for converting parts created within a variety of commercially available solid modeling programs into appropriate grayscale mask files accepted by common Laser Pattern Generators (LPGs), such as a Heidelberg 66FS. This customized software and associated process should lower the barrier-to-entry for grayscale lithography and could fuel breakthroughs in fields such as MEMS bistable devices, miniaturized biomedical sensors with greater sensitivity due to enhanced mixing, and potentially help spawn micro-3D printing.

By enabling 3D parts designed within common programs such as SolidWorks to be directly fabricated in MEMS devices, a large pre-existing pool of engineering professionals can design MEMS projects with little additional training. However, a non-linear relationship exists between ultra-violet (UV) exposure intensity and photoresist development depth. Therefore, a calibration step is needed to calibrate these effects into the software in order to obtain the correct microstructure surface geometry.

SolidWorks is a well-established CAD software with a worldwide pre-existing user base. With SolidWorks an engineer designs a desired structure and saves the 3D file as shown in Figure 3.18. Once the desired 3D structure is completed, it is exported to a stereolithography (STL) format so that our customized grayscale conversion software can read it. Next, an engineer would load this file in the grayscale conversion software as shown Figure 3.19 and select various process parameters such as the maximum height of the features, *xyz* resolution, etc. (A detail instruction of the grayscale conversion software

operating procedure is provided in the Appendix). The conversion software automatically slices up the model into a total of 128 layers in the vertical direction, while the first layer is set coincident with the substrate surface, and the 128th layer is set coincident with the highest point of the model. Individual layer thicknesses are calculated based on the parameters of the model. This process creates 3D pixels and generates a grayscale mask file in Drawing Exchange Format (DXF). Figure 3.20 shows the resulting mask file and detail of the level of complexity for the sample hemisphere array.

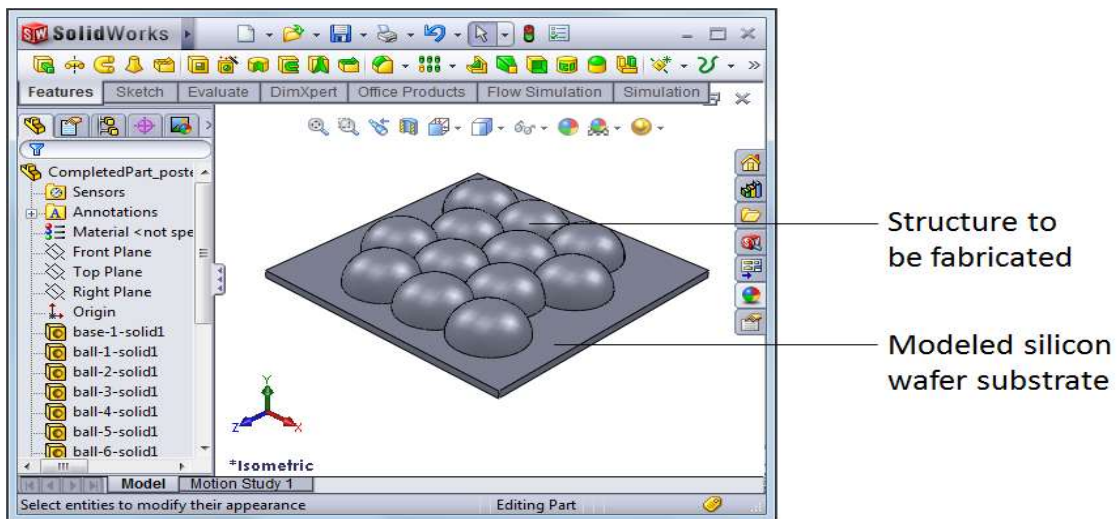


Figure 3.18. 3D microstructure design. Part design in commercially available solid modeling program (SolidWorks) showing modeling of desired structure (hemisphere array) on a simulated silicon wafer substrate (note: units/scale used in part modeling are arbitrary).

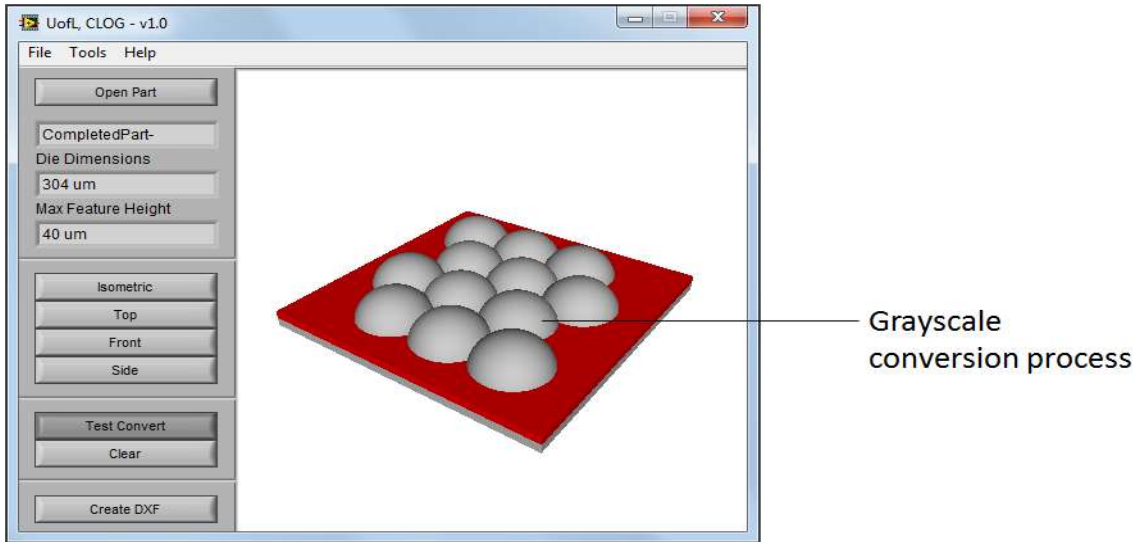


Figure 3.19. Grayscale conversion software showing mask generation process. Part is saved from solid modeling program as a stereolithography (STL) file, then imported and mask file is rendered.

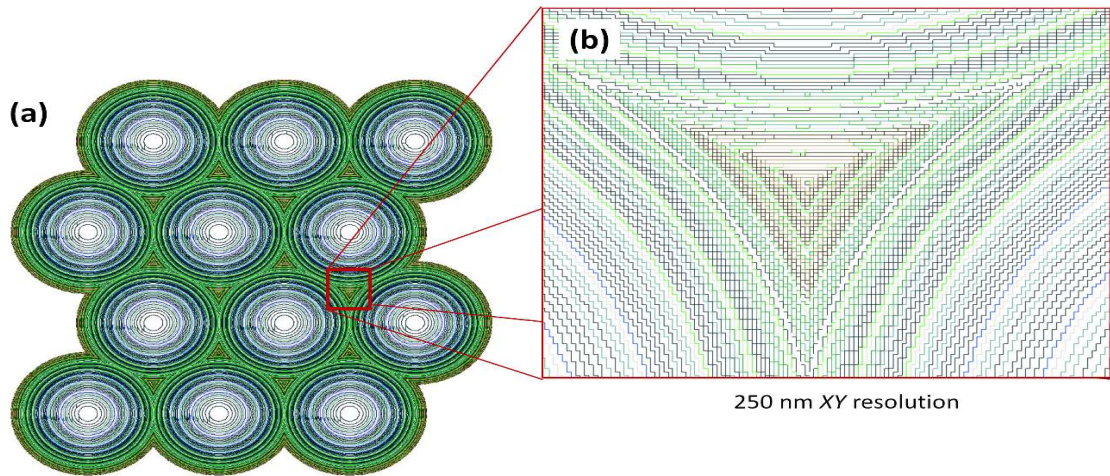


Figure 3.20. (a) Grayscale mask file resulting from the conversion process in and (b) detail of grayscale mask showing 250 nm XY resolution.

3.2.2 Grayscale Lithographic Equipment

A Heidelberg 66FS Laser Pattern Generator (LPG) system (Figure 3.21) was with our software to fabricate 3D prototypes in resist. The Heidelberg DWL 66FS is a high resolution pattern generator for mask making and direct writing (a maskless processes). Traditionally, Heidelberg LPGs were used only for binary exposures to write/make 2D structures, but the Heidelberg 66FS added functionality to modulate the laser intensities to 128 different levels during the writing process. This feature permits one to use the DWL 66FS for grayscale lithography to create more complex 3D structures. The DWL 66FS employs a diode laser (~405 nm), and the laser output power is between 20 mW and 180 mW, depending on the specific design. This LPG system comes with a conversion workstation and a conversion software package to convert source files from gerber, dxf, cif, gdsii, hpgl or structure format into the LIC format as input for the machine [51].



Figure 3.21. Heidelberg 66FS Laser Pattern Generator

During an exposure, this LIC format data is converted in real time into the final pixel data set [51]. Theoretically the original design data could be converted directly to the final pixel set, but the advantage of the LIC format is that its file size is much smaller due to a

highly optimized compression, leading to a much faster data transfer from the workstation to the system [51]. The resolution of the patterned design depends on the writing head. The University of Louisville Micro/Nano Technology Center (MNTC) has four different writing heads which are named based on their focal lengths. Minimum feature size and feature size limit of the various heads are presented in Table 3.2. The 20 mm head writes faster than the other heads while the 2 mm head writes slower than other heads, but write time is inversely proportional to minimum feature time.

Table 3.2. LPG specifications.

Focal length of the head (mm)	2	4	10	20
Minimum feature size (μm)	0.6	1	2.5	5
Feature size limit (μm)	1	2	5	10
Address grid (nm)	50	100	125	250

3.2.3 Grayscale Fabrication Process

First AZ 4620 photoresist was spun onto a 4" silicon wafer using a Headway spinner. A spread speed of 500 RPM for 5 secs and a spin speed of 4000 RPM for 30 secs were selected. A soft bake was then performed for 10 min at 90°C on a hotplate, which is below the glass transition temperature of the AZ 4620 resist. This procedure formed around a 6 μm thick resist layer on top of the silicon wafer. A relatively thick photoresist layer is critical for nice 3D geometries because various intensities of light will expose various depths of the resist. If the resist is not thick enough, it can result in different

exposure levels effectively registering the same exposure. A converted ramp structure was used to characterize the parameters of the Heidelberg 66FS with the targeted resist so that it gives the desired depth. Energy of the laser beam and its focus setting were adjusted until the depth became 4-5 μm . After exposure, AZ 400k solution was used to develop the exposed structure. AZ 400k developer is supplied as a concentrate so it was diluted with DI water to a ratio of 1:4 as described in Section 3.1.3. Finally, the wafer was rinsed in a QDR (Quick Dump Rinse) followed by a SRD (Spin Rinse Dryer). A Veeco Dektak 8M profilometer was used to scan the profile of the structures and a Zygo Optical Interferometer was used to generate the 3D images of the fabricated resist structures.

3.2.4 Results and Discussion

Each particular type and brand of photoresist needs to be previously characterized when being used for grayscale applications because it plays the major role in how the exposure is transformed into the 3D image. AZ 4620 is a thicker positive photoresist which can be used in many 3D MEMS applications. The range of available film thicknesses of this resist is approximately from 6 μm to 20 μm , and this can be achieved by varying the spin and spread RMP values.

Using our grayscale conversion software on a SolidWorks-designed ramp with AZ 4620 resist and the Heidelberg 66FS LPG, the structure was fabricated. Figure 3.22 (a) shows the Dektak profilometer scan of the final ramp structure in resist. As you can see, the experimental result is not completely linear indicating that the resist exposure needs to be calibrated. Figure 3.22 (b) shows the experimental profile vs. the theoretical profile, which emphasizes the nonlinear correlation between exposure intensity and development

depth of the photoresist. This suggests that a calibration step is required to adjust the layer segmentation in the mask file. This nonlinear relationship is assumed to be uniquely dependent on the given set of process variables, such as photoresist type, spin speed/time, soft bake time and LPG settings. Therefore, running a new calibration structure is required if the above variables are changed. It is crucial for correctly adjusting layer segmentation in the grayscale conversion process, a necessary step as most photoresists are not chemically engineered for grayscale lithography.

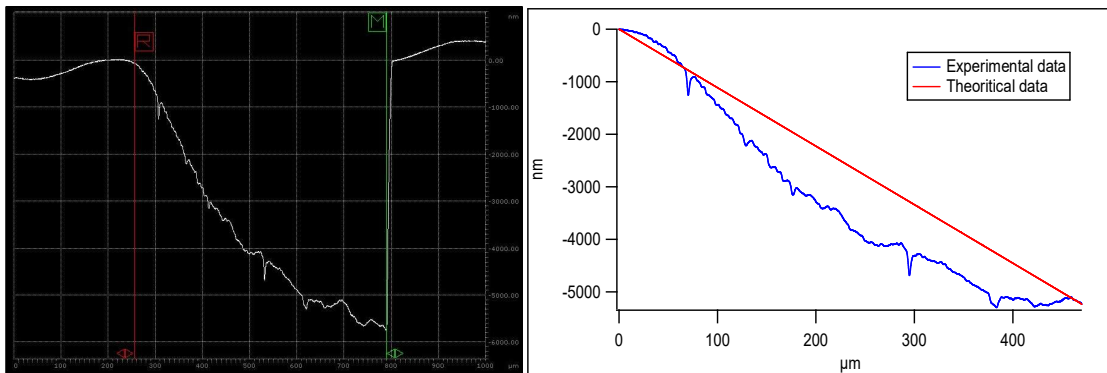


Figure 3.22. (a) Dektak profilometer of the ramp structure (b) Experimental profile vs. the theoretical profile.

An n^{th} order polynomial was determined by fitting in to the data in the Figure 3.22 (a) profilometer scan, and coefficients of the polynomial equation were inserted into the grayscale conversion software to obtain the corrected mask file. Figure 3.23(a) and (b) present the surface profile of the ramp structure after the calibration process, showing substantial improvement.

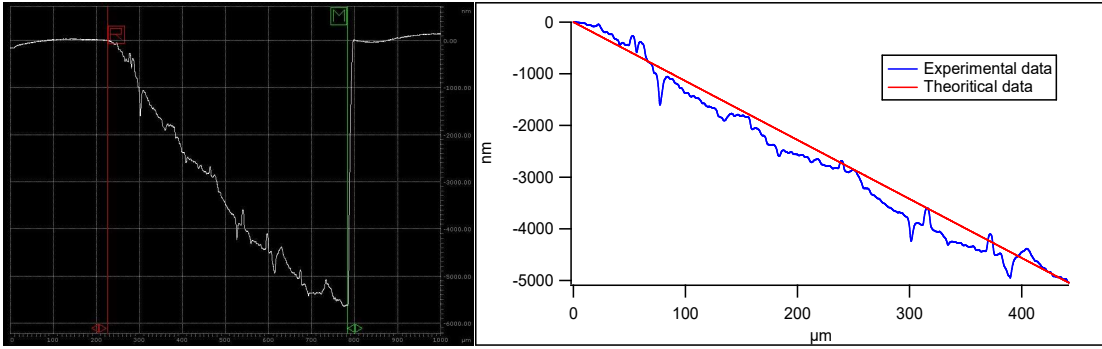


Figure 3.23. (a) Dektak profilometer of the ramp structure after calibration. (b) Experimental profile vs. the theoretical profile

Once the nonlinear correlation is determined, this relationship can be applied to any other grayscale mask using the conversion software as long as the same photoresist, spin speed/time, soft bake time and the LPG settings are used. After the calibration process, another grayscale mask was created to make dome structures with 300 μm diameter and the same fabrication process was used without changing the above discussed parameters. Figure 3.24 (a) and (b) show the Dektak profile without the calibration step and with the calibration step. We believe the discontinuities in the surface profile as shown in Figure 3.24 (b) may be a result of stitching errors from neighboring passes of the laser interfering with each other and either overexposing or underexposing portions of the photoresist during the writing process (and not due to non-linearity of the photoresist) [50].

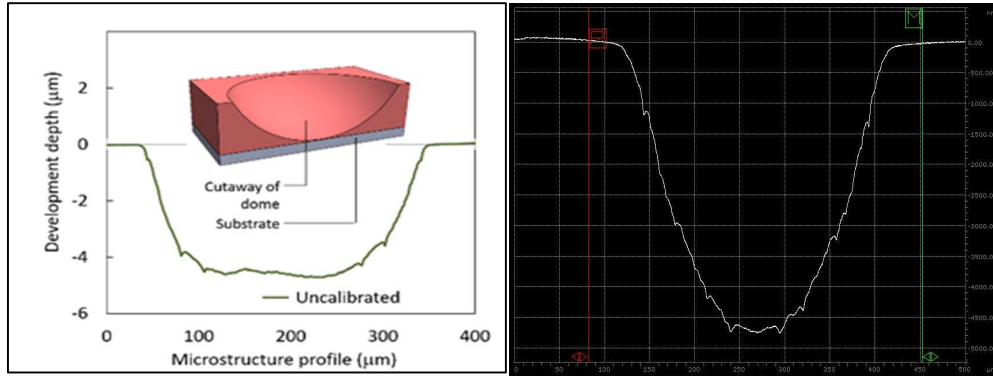


Figure 3.24. (a) Uncalibrated Dektak profile for the inverted dome structure [50]. (b) Calibrated Dektak profile for the inverted dome structure.

Since the ultimate goal for our research group is the fabrication of bistable MEMS devices that buckle or change mechanical state with temperature, the domelike structures fabricated in resist using grayscale lithography can be used as building platforms onto which other materials can be deposited. For example, after the dome structure is produced in resist, it can then be covered with a variety of thin films, all with different CTEs. Using appropriate materials and specific layout designs, it should be possible to create hemispherical discs which change states with temperature, thus allowing the creation of no-electrical-power (NEP) temperature sensors and switches. However, such interesting applications require an extremely smooth surface to deposit the materials onto after the grayscale process. Therefore, we added an additional processing technique after grayscale exposure and development, namely the thermal reflow process presented in Section 4.1. Once grayscale lithography was finished, the wafer was then placed on a hot plate at 150°C for one hour, which is above the glass transition temperature of the AZ 4620 photoresist. Figure 3.25 shows the improvement of the surface of the dome structure after the thermal reflow process. The only downside of this technique is that the

reflow process slightly changes the dimension of the dome structure as shown in Figure 3.25. However, that change could be incorporated into the engineer's design space.

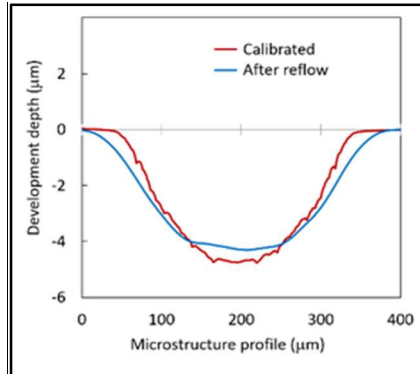


Figure 3.25. Dektak profilometer of the dome structure after thermal reflow [50].

CHAPTER IV

DEVELOPING MEMS BISTABLE ACTUATORS

4.1 Introduction

The overall objective of this research is to design, fabricate, and test a bistable MEMS buckled diaphragm which will change its state (buckled up/down) upon the application of a set temperature. These novel buckled structures have the potential to introduce a new era in MEMS no power devices. They could serve as the building blocks for no power MEMS-based temperature sensors, pressure sensors, radiation sensors, actuators, switches, and even thermal energy harvesting devices. Chapters 3 and 4 provided a description of various fabrication strategies for processing domed structures which serve as the heart of the buckle devices using resist reflow and grayscale lithography. This chapter focuses on creating the dome buckled structures by leveraging the internal stress which is found in the deposition of various thin films instead.

A simplified explanation of using stress in thin films to form dome structures is provided in Figure 4.1. The figure shows the deposition of a stress-free thin film on a silicon wafer followed by a deep silicon etch from the backside. If an external force is then applied at the boundaries of the film, it will create internal compressive stress in the film, causing it to buckle and form a nice bistable dome structure if patterned in a circular shape [52].

While the strategy presented in Figure 4.1 is theoretically possible, a more practical strategy to implement is the deposition of a highly compressive thin film to begin with. Upon its release during the silicon etching process, the thin film will then buckle on its own.

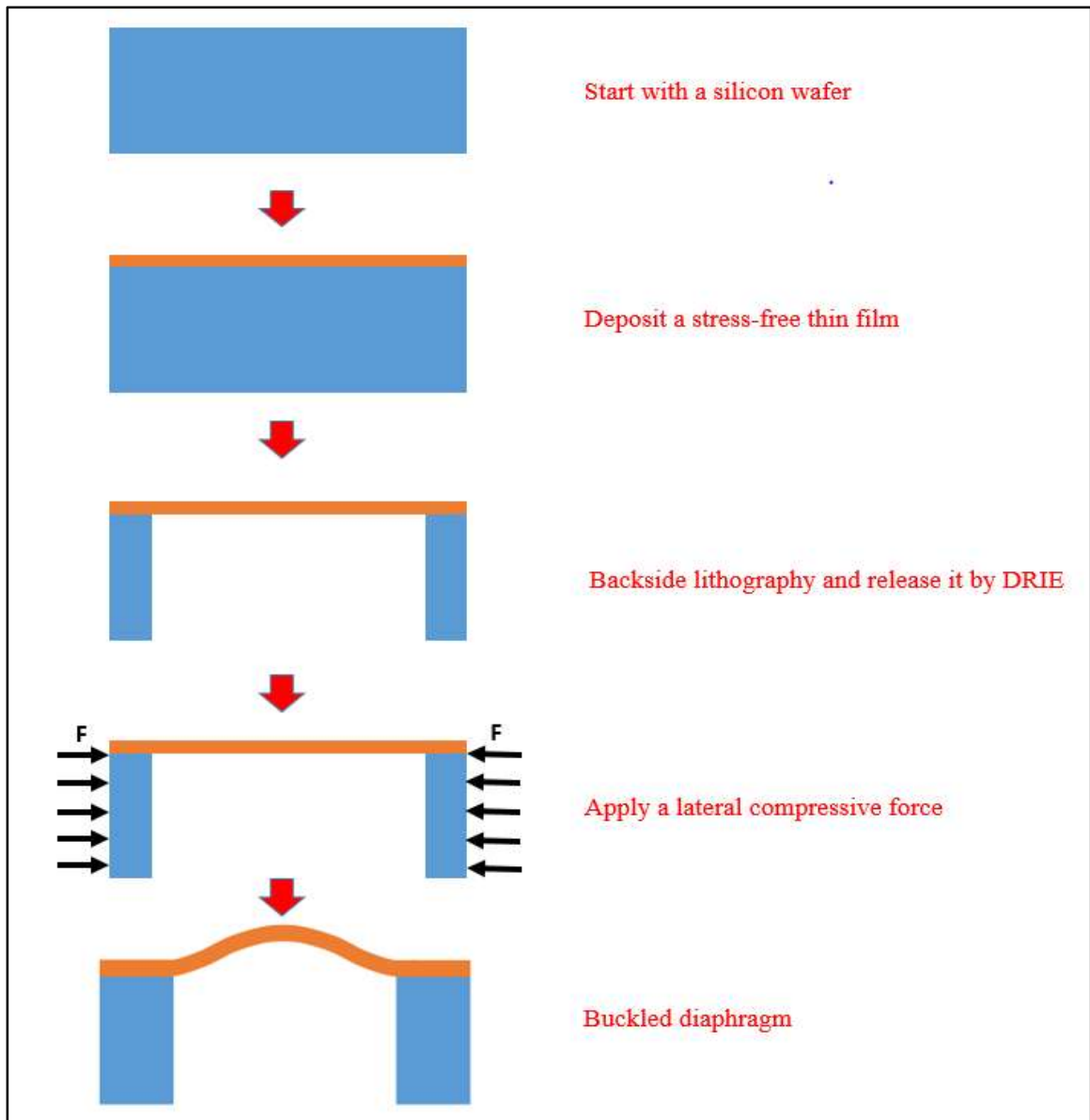


Figure 4.1. Formation of buckled diaphragms.

To accomplish that strategy, we selected a unique combination of low stress polyimide along with highly-compressive thermally-grown silicon oxide (SiO_2) [53]. The highly compressive oxide film provided the required internal forces required to make the circular bilayer pattern to buckle and form a dome structure when released. These structures proved to be bistable as well. Polyimide is used as a mechanical structural layer to protect the thermal oxide so that it can produce uniform smooth buckled diaphragms upon release.

Once these buckled structures are formed, the diaphragm can switch its state from the 1st state to the 2nd state upon application of stimulus (ex: pressure, temperature, force, etc.). Upon removal of the stimulus, the diaphragm remains in its 2nd stable state. This behavior is called true bistability. To make the bistable element sensitive to temperature, an additional material needs to be added which supplied the required temperature sensitive force to switch its state to the 2nd state. A second material, such as aluminum which has a higher coefficient of thermal expansion (TCE) (10 times CTE of silicon) compared to oxide and polyimide was selected and deposited on top of the diaphragm. This layer will hopefully supply the required force to change the element's state due to thermal mismatch of the materials. Such bistable buckled diaphragms offer 3 distinct advantages over traditional MEMS actuators; 1) larger displacements, 2) truly bi-stable operation, and 3) requirement of zero electrical power to hold the diaphragms in each of its stable states (i.e. mechanical memory). The details of this process are described in Section 4.3. The theory behind these circular buckled diaphragms is explained in Section 4.2. Candidate materials for the diaphragms are presented in Section 4.3, followed by the fabrication process, and test results which are presented in Sections 4.4 and 4.5.

4.2 Buckling Theory for Circular Diaphragms

Diaphragms can be divided into two categories - thick diaphragms and thin diaphragms. When the maximum displacement (h_0) is greater than the thickness (t) of the diaphragm, it is known as a “thin diaphragm” and when the maximum displacement (h_0) is smaller than the thickness (t) of the diaphragm, it is called a “thick diaphragm” as shown in Figure 4.2. The deflection (h) of a circular thick diaphragm with radius R is described by the following equation [3, 54, 55].

$$h(r) = h_0 \left(1 - \frac{r^2}{R^2}\right)^2 \quad 4.1$$

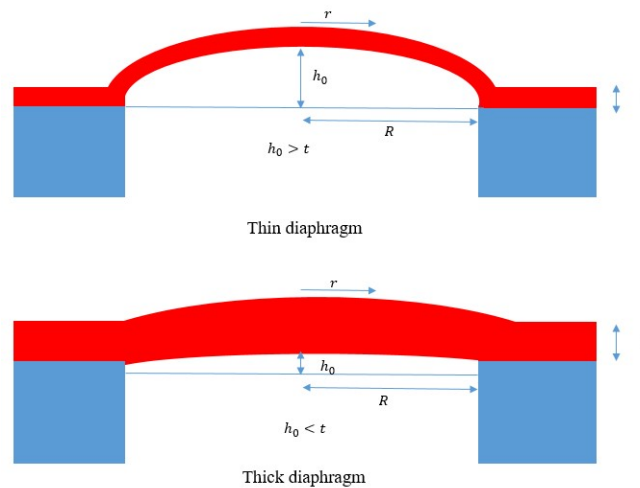


Figure 4.2. Thin diaphragm vs. thick diaphragm.

When the deflection becomes much larger than the thickness of the diaphragm (which is a thin diaphragm), the shape of the diaphragm mainly depends on the stress due to straining compared with the bending moments which may be neglected in calculations [55]. Therefore, the deflection of a thin diaphragm can be assumed to act in the shape of a parabola, and equation 4.2 describes its parabolic shape.

$$h(r) = h_0 \left(1 - \frac{r^2}{R^2}\right) \quad 4.2$$

This study only discusses thin diaphragms and provides some important equations to find the deflection of a thin diaphragm [54, 55]. The deflection of a thin circular diaphragm, as shown in Figure 4.3, can be calculated using differential pressure with the equilibrium of forces acting on the surface. The force acting on the diaphragm (F_{PZ}) is equal to the surface area (πR^2) times the differential pressure (P). This force is balanced by the force (F_{FZ}) which is ($F_F * \sin \alpha$), on the frame fixing the diaphragm at the circumference. The force F_F pulls as a result of the diaphragm stress (σ) and this force is equal to the diaphragm cross section at the border ($2\pi R t$) times the stress (σ). This can be summarized as follows,

$$F_{PZ} = P * \pi R^2 = -F_{FZ} = -F_F * \sin \alpha = -2\pi R t \sigma \sin \alpha \quad 4.3$$

When the angle (α) is small, it can be equated to the tangent which is the slope of the diaphragm at the edge and can be determined by taking the derivative of the equation 4.2 (function of the parabola curve).

$$P * \pi R^2 \approx -2\pi R t \sigma \tan \alpha = -2\pi R t \sigma \left[\frac{\partial h(r)}{\partial r} \right]_{r=R} = -2\pi R t \sigma * \left(-\frac{2h_0}{R} \right) = 4\pi t h_0 \sigma \quad 4.4$$

The differential pressure can be simplified as follows,

$$P = \frac{4t h_0 \sigma}{R^2} \quad 4.5$$

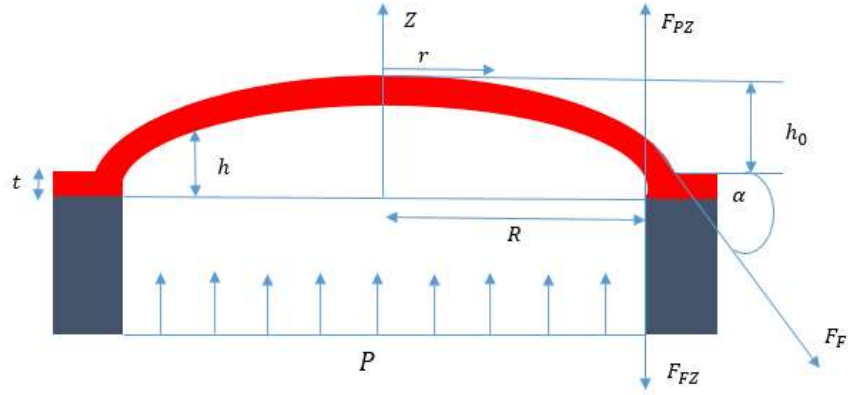


Figure 4.3 Cross section of a thin diaphragm loaded with a differential pressure and equilibrium of forces.

The stress of the diaphragm (σ) has two components: they are the residual stress (σ_0) (when there isn't any deflection of the diaphragm) and the stress (σ_D) due to Hooke's law generated by the deflection of the diaphragm. Then the strain in radial (ε_r) and tangential (ε_t) directions can be calculated using the Hooke's law as follows [55].

$$\varepsilon_r = \frac{\sigma_r}{Y} + \nu \frac{\sigma_t}{Y} = \frac{(\sigma_r + \nu \sigma_t)}{Y} \quad 4.6$$

$$\varepsilon_t = \frac{\sigma_t}{Y} + \nu \frac{\sigma_r}{Y} = \frac{(\sigma_t + \nu \sigma_r)}{Y} \quad 4.7$$

In the above, σ_r is the radial stress, σ_t is the tangential stress, ν is the Poisson's ratio of the diaphragm and Y is the Young's modulus of the diaphragm. Then an expression for the length of a parabola can be obtained by considering a small height (h_0) at its peak as follows [55].

$$L \approx 2R \left(1 + \frac{2h_0^2}{3R^2} \right) \quad 4.8$$

The radial strain can be determined by subtracting equation 5.8 from the base length which is $2R$ as given in equation 4.9.

$$\varepsilon_r = 2R \left(1 + \frac{2 h_0^2}{3 R^2} \right) - 2R = \frac{2 h_0^2}{3 R^2} \quad 4.9$$

The tangential strain can be determined using following two boundary conditions.

1) In the center of the diaphragm, radial and tangential strains are equal because the strain is not a function of direction at this position due to symmetry [54, 55].

$$\sigma_r = \varepsilon_r \frac{Y}{1-\nu} \quad 4.10$$

2) At the circumference, tangential strain is zero because the diaphragm is clamped there and the frame does not allow any movements of the membrane [54, 55].

$$\sigma_r = \varepsilon_r \frac{Y}{1-\nu^2} \quad 4.11$$

By considering the first boundary condition, equation 4.9 is substituted in equation 4.10 to find the radial stress. Then the total stress can be found by adding the radial stress and the residual stress as given in equation 4.12.

$$\sigma = \sigma_0 + \frac{2 h_0^2}{3 R^2} \frac{Y}{(1-\nu)} \quad 4.12$$

Next, equation 4.12 is substituted to equation 4.5 further simplifying the differential pressure as given below.

$$P = \frac{4th_0}{R^2} \left[\sigma_0 + \frac{2 h_0^2}{3 R^2} \frac{Y}{(1-\nu)} \right] \quad 4.13$$

Equation 4.13 is called *Cabrera's equation* which is used to calculate deflection of diaphragms [54, 55].

By considering the second boundary condition, equation 5.13 can be modified as follows.

$$P = \frac{4th_0}{R^2} \left[\sigma_0 + \frac{2h_0^2}{3R^2} \frac{Y}{(1-\nu^2)} \right] \quad 4.14$$

Both equation 4.13 and equation 4.14 are not entirely precise, because two boundary conditions discussed above on the strain distribution are not quite correct and the equations are different by the Poisson's ratio only [54].

In general, both stress and bending moments are taken into account to get a more accurate expression for the differential pressure. First, the total energy of the buckled diaphragm is determined and the force exerted by the diaphragm is calculated by taking the first derivative of the total energy with respect to its deflection. The extremes of the potential energy correspond to the positions where the total exerted forces are zero.

The total energy of the buckled diaphragm can be expressed as follows [3, 54, 55],

$$V = \int_0^{2\pi} d\varphi \int_0^R r dr \left[\frac{t^3}{24(1-\nu^2)} \left(\frac{\partial^2 h}{\partial r^2} + \frac{1}{r} \frac{\partial h}{\partial r} + \frac{1}{r^2} \frac{\partial^2 h}{\partial \varphi^2} \right)^2 + \frac{t}{2} \left(\sigma_{r0} \left\{ \frac{\partial h}{\partial r} \right\}^2 + \frac{\sigma_{\varphi 0}}{r^2} \left\{ \frac{\partial h}{\partial \varphi} \right\}^2 \right) + \frac{t}{2} \frac{Y}{(1-\nu^2)} \frac{1}{4} \left(\frac{\partial h}{\partial r} \right)^4 - hP \right] \quad 4.15$$

The first term in the brackets of the equation corresponds to the effect of the bending moments, the second term corresponds to the residual diaphragm stress in radial and tangential directions, the third term corresponds to the contribution of the stress due to straining of the neutral fiber, and the last term corresponds to the energy generated by moving the diaphragm at the pressure difference [54, 55]. Equation 4.15 can be solved

introducing a fourth order polynomial deflection curve (h_r) for the circular diaphragm to find the minimum potential energy [55]. By skipping the math, the total force exerted by the diaphragm can be calculated as follows [54, 55].

$$F_F = \frac{\partial V}{\partial h_0} = \frac{2\pi}{3} \left(\frac{8}{3} \frac{Y t^3 h_0}{R^2 (1-\nu^2)} + 2t\sigma_0 h_0 + \frac{128}{105} \frac{Y t h_0^3}{R^2 (1-\nu^2)} - \frac{1}{2} P R^2 \right) \quad 4.16$$

When the system is in the equilibrium, the total force ($F_F = \frac{\partial V}{\partial h_0} = 0$) becomes zero and differential pressure can be determined using equation 4.16.

$$P = \frac{4th_0}{R^2} \left(\frac{4}{3} \frac{t^2}{R^2} \frac{Y}{(1-\nu^2)} + \sigma_0 + \frac{64}{105} \frac{h_0^2}{R^2} \frac{Y}{(1-\nu^2)} \right) \quad 4.17$$

This generalized equation can be used to examine the behavior of diaphragms under different conditions. Similar to equation 4.15, equation 4.17 contains three major components as described below [55].

$$\text{Bending moments: } \frac{4th_0}{R^2} \left(\frac{4}{3} \frac{t^2}{R^2} \frac{Y}{(1-\nu^2)} \right)$$

$$\text{Residual stress: } \frac{4th_0}{R^2} (\sigma_0)$$

$$\text{Stress due to straining of the neutral fiber: } \frac{4th_0}{R^2} \left(\frac{64}{105} \frac{h_0^2}{R^2} \frac{Y}{(1-\nu^2)} \right)$$

Bending moments and residual stress show a linear relationship between differential pressure and diaphragm deflection, while the stress due to straining contributes with its third power. Moreover, there is a transition from a monostable to a bistable diaphragm and this stress, *known as the critical stress σ_c of the diaphragm*, occurs where the slope of the differential pressure at the origin is zero [55]. This critical stress can be calculated

by taking the first derivative of the equation 4.17 with respect to the deflection and equating it to zero as described below.

$$0 = \left. \frac{\partial P}{\partial h_0} \right|_{h_0=0} = \frac{4t}{R^2} \left(\frac{4 t^2}{3 R^2} \frac{Y}{(1-\nu^2)} + \sigma_0 \right)$$

$$\sigma_C = - \frac{4 t^2}{3 R^2} \frac{Y}{(1-\nu^2)} \quad 4.18$$

As seen in equation 4.18, the critical stress depends upon the dimension of the circular diaphragm rather than the material properties, and these dimensions can be changed to design buckled diaphragms.

When there is not any differential pressure ($P=0$), the deflection of a diaphragm (h_0) and the compressive stress can be calculated using equation 4.17.

There are two possible solutions for the deflection of a diaphragm (h_0).

$$h_0 = 0 \quad 4.19$$

or

$$\left(\frac{4 t^2}{3 R^2} \frac{Y}{(1-\nu^2)} + \sigma_0 + \frac{64 h_0^2}{105 R^2} \frac{Y}{(1-\nu^2)} \right) = 0$$

$$h_0 = \pm \frac{\sqrt{35}}{4} t \sqrt{\frac{\sigma_0}{-\sigma_C} - 1} \quad 4.20$$

$$\text{where; } \sigma_C = - \frac{4 t^2}{3 R^2} \frac{Y}{(1-\nu^2)}$$

The first solution (equation 4.19) corresponds to a flat diaphragm and the second solution (equation 4.20) determines the deflection of a bistable diaphragm with compressive stress.

As previously discussed, when the stress is more compressive than the critical stress, the diaphragm buckles. Equations 4.17 to 4.20 were developed by considering the equilibrium of the system which implies the total force acting on the diaphragm is zero. For example, if the diaphragm is initially buckling downward without any differential pressure, it will require a certain force to change its state from buckled down to buckled up. This critical force can be determined by taking the first derivative of equation 5.16 with respect to the deflection and equating it to zero. Then the deflection of the buckled diaphragm at the point of snapping or actuation (h_{snap}) is determined as described in equation 4.2 [55].

$$\frac{\partial F_F}{\partial h_0} = \frac{2\pi}{3} \left(\frac{8}{3} \frac{Yt^3}{(1-\nu^2)} \frac{1}{R^2} + 2t\sigma_0 + \frac{128}{35} \frac{Yth_0^2}{(1-\nu^2)} \frac{1}{R^2} \right) = 0 \quad 4.21$$

$$h_{snap} = \pm \frac{\sqrt{35}}{\sqrt{34}} t \sqrt{\frac{\sigma_0}{-\sigma_C} - 1} = \frac{1}{\sqrt{3}} h_0 \quad (P=0) \quad 4.22$$

$$\text{where; } \sigma_C = -\frac{4}{3} \frac{t^2}{R^2} \frac{Y}{(1-\nu^2)}$$

Now equation 4.22 is substituted in equation 4.26 to find the critical force required to snap the diaphragm to the next state [55].

$$F_C = \pm \frac{\pi}{3} \left(\frac{7}{3} \sqrt{\frac{35}{3}} t^2 \sigma_C \left(\frac{\sigma_0}{\sigma_C} - 1 \right)^{3/2} - PR^2 \right) \quad 4.23$$

The above discussed equations provide a basic explanation for buckled bistable circular diaphragms. These equations are used to design and develop a MEMS bistable temperature sensor.

4.3 Candidate Materials for the Diaphragm

Buckling is a mechanical phenomenon that can occur in structures (beams or diaphragms) based on a combination of applied compressive stresses, material stiffness, and the slenderness ratio of the structure (radius of gyration/length or thickness/diameter) [19]. As lateral compressive force is applied to the diaphragm, the diaphragm is simply compressed by building up compressive stress on the diaphragm. When compressive stress on the diaphragm is further increased, this will result in an unstable state for the structure. When the critical buckling stress is reached, the transverse deflection increases rapidly and the beams/diaphragms buckle to their 1st stable state which has a lower total strain energy than the simple compressed state [56, 57].

This section provides a quick overview of the candidate materials which were used in this research. *Thermally grown oxide was used to provide the compressive stress needed for buckling and polyimide was selected as the stress-free material to provide mechanical stability and integrity for the diaphragm. Aluminum was then investigated as the candidate material that provided the temperature-sensitive force needed to change the diaphragm from its 1st stable state to its 2nd stable state.*

4.3.1 Thermal Oxide

Thermal oxidation using oxygen or water vapor in combination with a silicon substrate is a common way to produce SiO_2 . Silicon dioxide layers can also be produced by using

chemical vapor deposition (CVD) which involves a much smaller thermal budget than thermal oxidation. The CVD technique is usually used when the underlying film is not silicon (i.e. a metal layer). CVD deposited oxide does not have the same high density and large breakdown voltage as thermally grown oxide. Another drawback to CVD oxide is the interface between the deposited oxide and the underlying silicon is not as electrically stable as thermal oxide.

Thermal oxidation is a chemical process where silicon dioxide (SiO_2) is grown on a silicon wafer in the presence of oxygen at a high elevated temperature, typically ranging from 900 to 1200°C. Thermal oxidation even takes place at room temperature if the silicon is exposed to oxygen, but at a much reduced rate. However, it does slowly create a thin native oxide layer of around 1 nm [58] within a few hours at room temperature and the growth slows down with the time because the oxygen atoms have too small of energy at room temperature to diffuse through the already formed oxide layer [59].

A diffusion of oxidants and a volume increase occur simultaneously to transform the silicon substrate into a thin SiO_2 layer. This thermal oxidation process is strongly influenced by the oxidant species, temperature, pressure, and the crystal orientation of the silicon substrate ($\langle 100 \rangle$ or $\langle 111 \rangle$). Silicon is consumed as the oxide grows, and the resulting oxide gets thicker during growth as shown in Figure 4.4. The final oxide layer is approximately 54% above the original surface of the silicon and 46% below it. That is, for every 1 μm of silicon oxide grown, about 0.46 μm of silicon is consumed [60].

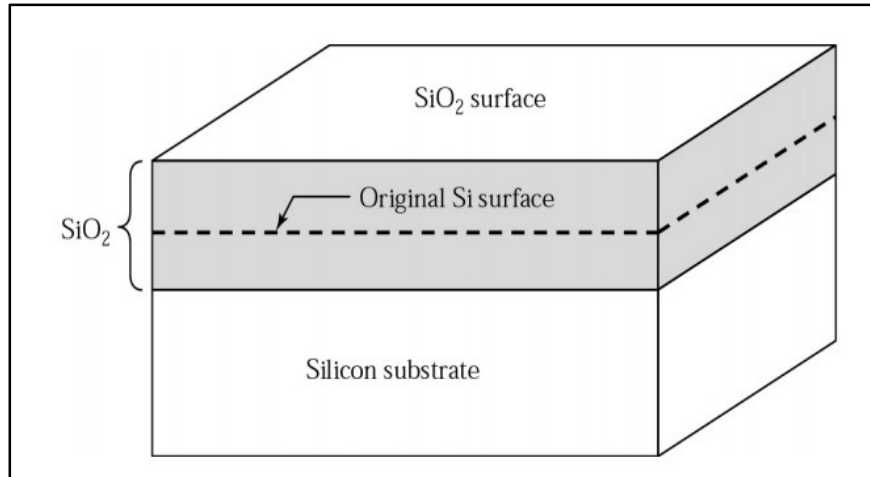


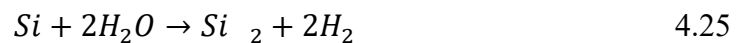
Figure 4.4. Growth of silicon dioxide by thermal oxidation [60].

Thermal oxidation is usually performed at atmospheric pressure in an oxidizing environment comprised of either an oxygen gas or a mix of oxygen gas and water vapor. Oxidation in oxygen gas is known as “dry oxidation”, whereas oxidation in water vapor and oxygen gas is known as “wet oxidation”. The chemical reactions that take place for these cases can be represented as follows.

For dry oxidation;



For wet oxidation;



Dry oxidation has a slower deposition rate than wet oxidation although the oxide film quality is better than the wet oxide film. Therefore, thin oxides (<1000Å) such as the gate oxide of MOS devices are almost always formed using dry oxidation. In addition, dry oxidation results in a higher density oxide than wet oxide, resulting in a higher

breakdown voltage (5 to 10 MV/cm) [61]. During the wet oxidation process, the water molecules dissociate at high temperatures to form hydroxide “OH” that can diffuse in silicon faster than oxygen molecules giving a significantly higher deposition rate. Wet oxidation is typically used to grow thick oxides, and this oxide layer can also provide selective masking against the diffusion of dopants at elevated temperatures, a very useful property in MEMS and microelectronic fabrication. Table 4.1 shows some important properties of thermal oxide [62, 63]. For this research, the mechanical properties such as thermal expansion coefficient, Poisson’s ratio, and Young’s modulus are especially important.

Table 4.1. Properties of thermal oxide [62, 63].

Crystal structure	Amorphous
Atomic weight	60.08g/mole
Density (thermal, dry/wet)	2.27/2.18g/cm ³
Molecules	$2.3 \cdot 10^{22} / \text{cm}^3$
Specific heat	1.0J/g-K
Melting point	1700 °C
Thermal expansion coefficient	$5.6 \cdot 10^{-7} / \text{K}$
Young's modulus	$6.6 \cdot 10^{10} \text{ N/m}^2$
Poisson's ratio	0.17
Thermal conductivity	1.1W/m-K - 1.4W/m-K
Relative dielectric constant	3.7 - 3.9
Dielectric strength	10^7 V/cm
Energy bandgap	8.9eV
DC resistivity	$\simeq 10^{17} \Omega \text{ cm}$

Thermal cycling of the substrate and thermal mismatch between deposited layers can lead to the development of stress within a device, ultimately manifesting itself in device failure[64]. Even though this thermal oxide creates problems due to the high mechanical stress induced in the structures [65], this interesting internal compressive stress of the thermal oxide can be leveraged to produce buckled MEMS diaphragms [19].

As previously discussed, thermal oxidation takes place at a high temperature and then cooled down to room temperature at the end of the process. Silicon ($2.3 \times 10^{-6} K^{-1}$) has a higher coefficient of thermal expansion (CTE) compared with silicon oxide ($5.6 \times 10^{-7} K^{-1}$). Due to the mismatch of the CTEs, silicon contracts more than the thermal oxide during the cooling process, as shown in Figure 4.5. This produces compressive stress on the thermal oxide film as shown in Figure 4.6. It is this thermally-produced compressive stress that we leverage to produce buckled structures.

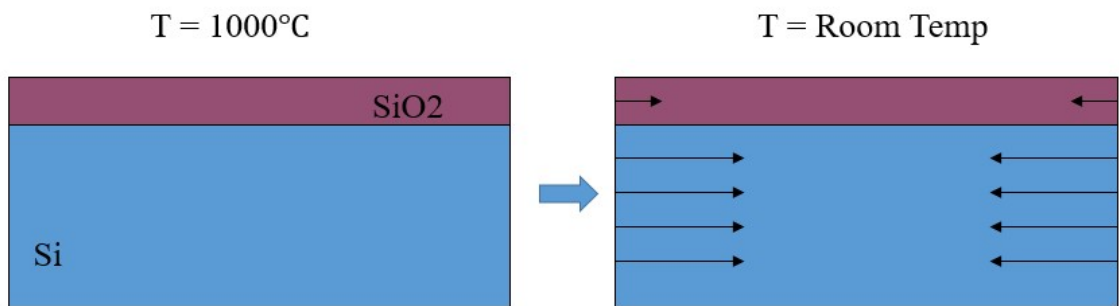


Figure 4.5. Contraction of the silicon and the thermal oxide.



Figure 4.6. Internal compressive stress of the thermal oxide thin film.

4.3.2 Polyimide

As previously mentioned, the silicon dioxide layer can serve as the source of highly compressive stress which is needed to produce the buckled structures. However, because the silicon dioxide film is so thin, when the structure is released from the bottom using deep reactive ion etch (DRIE), it typically results in a fragile and non-uniform dome with a wrinkled pattern on its surface as shown in Figure 4.7. Polyimide films are commonly used on wafers as passivation layers, stress buffer layers, dry etch masks, structural layers, and re-distribution layers for chip scale packaging and wafer level packaging [66]. Our research group has pioneered the use of polyimide as a mechanical stress-free structural layer to enhance the thin oxide films so that smooth dome-like buckled structures are possible.

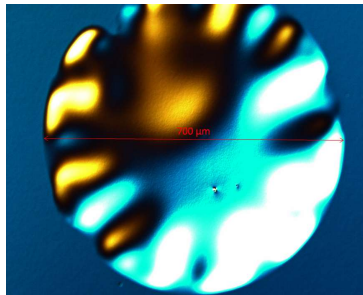


Figure 4.7. Non-uniform dome with a wrinkled pattern.

PI 2600 series products provide high molecular weight and the rigid rod polyimide structure of cured PI-2600 products exhibits desirable combination film properties such as low stress, low coefficient of thermal expansion (CTE), low moisture and high modulus [67]. This PI 2600 series polyimide from HD Microsystems is designed for MEMS applications such as semiconductor and packaging dielectric as well as substrate material. PI 2600 series polyimide is a good candidate material to choose as a structural

layer for thermal oxide considering its properties above discussed, specially having low stress and low CTE.

4.3.3 Aluminum

Aluminum thin films are used in variety of applications, especially in microelectronics, because of their low resistivity, high reflectance and low cost [68]. These applications include connections in semiconductor and integrated circuit devices, electrodes, and back contacts in solar cells. However, its property of having a higher coefficient of thermal expansion (CTE) than silicon and silicon dioxide is leveraged in this research. Once the bistable buckled diaphragm is fabricated, these oxide-polyimide diaphragms are bistable at room temperature, as demonstrated later in this chapter. In other words, if the diaphragms are initially in the buckled up state upon their release during fabrication, and an external force is applied downward, the diaphragm will snap to its buckled down state, which is its 2nd stable state and remain there. Instead of providing the actuation using an external force, we wish to use thermal actuation by depositing a layer of aluminum on top of the diaphragm. Upon deposition, the aluminum layer is comparatively free of stress [56, 69] and it doesn't effect buckling. The coefficient of thermal expansion (CTE) of aluminum is $23 \times 10^{-6}K^{-1}$, and it is higher than the CTE of polyimide and oxide. When increasing temperature is introduced to the diaphragm, the aluminum layer attempts to expand at a much higher rate than the polyimide and oxide layers. Upon heating, a biaxial state of compression is thereby induced in the aluminum film, which should counteract the effect of the compression in the oxide layer [56]. Once the temperature is reached to a certain value, the diaphragm should switch to its 2nd stable state.

4.4 Fabrication Process

This fabrication process involved a single mask process which is used to open arrays of circular patterns on the backside of the wafer to etch silicon using deep reactive ion etching (DRIE). The designed photomask contains arrays of circular pattern starting from 100 μm to 700 μm in diameter with 50 μm increment as shown in Figure 4.8. The process flow can be summarized as follows (see Figure 4.9): thermal oxidation to grow oxide on top of the silicon wafer, polyimide spin-deposition and thermal curing, metal deposition, and finally DRIE etching of the silicon. The left side of the Figure 4.9 shows the cross sectional view of the device fabrication flow and right side of the figure provides an overview of the process flow.

Three different types of composite diaphragms were experimentally researched and studied. They are 1) oxide-polyimide diaphragm (skipping step c), 2) oxide-aluminum diaphragm (skipping step d), and 3) oxide-aluminum-polyimide diaphragm (same as the given process flow).

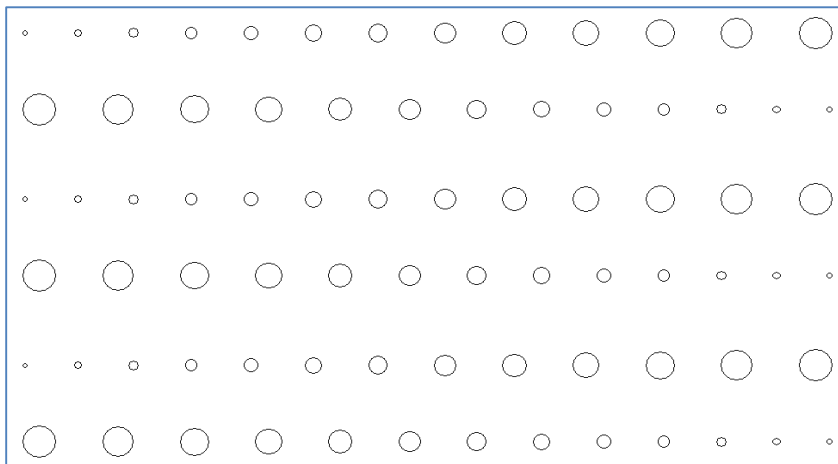


Figure 4.8. Mask design contains arrays of circular pattern starting from 100 μm to 700 μm in diameter with 50 μm increment.

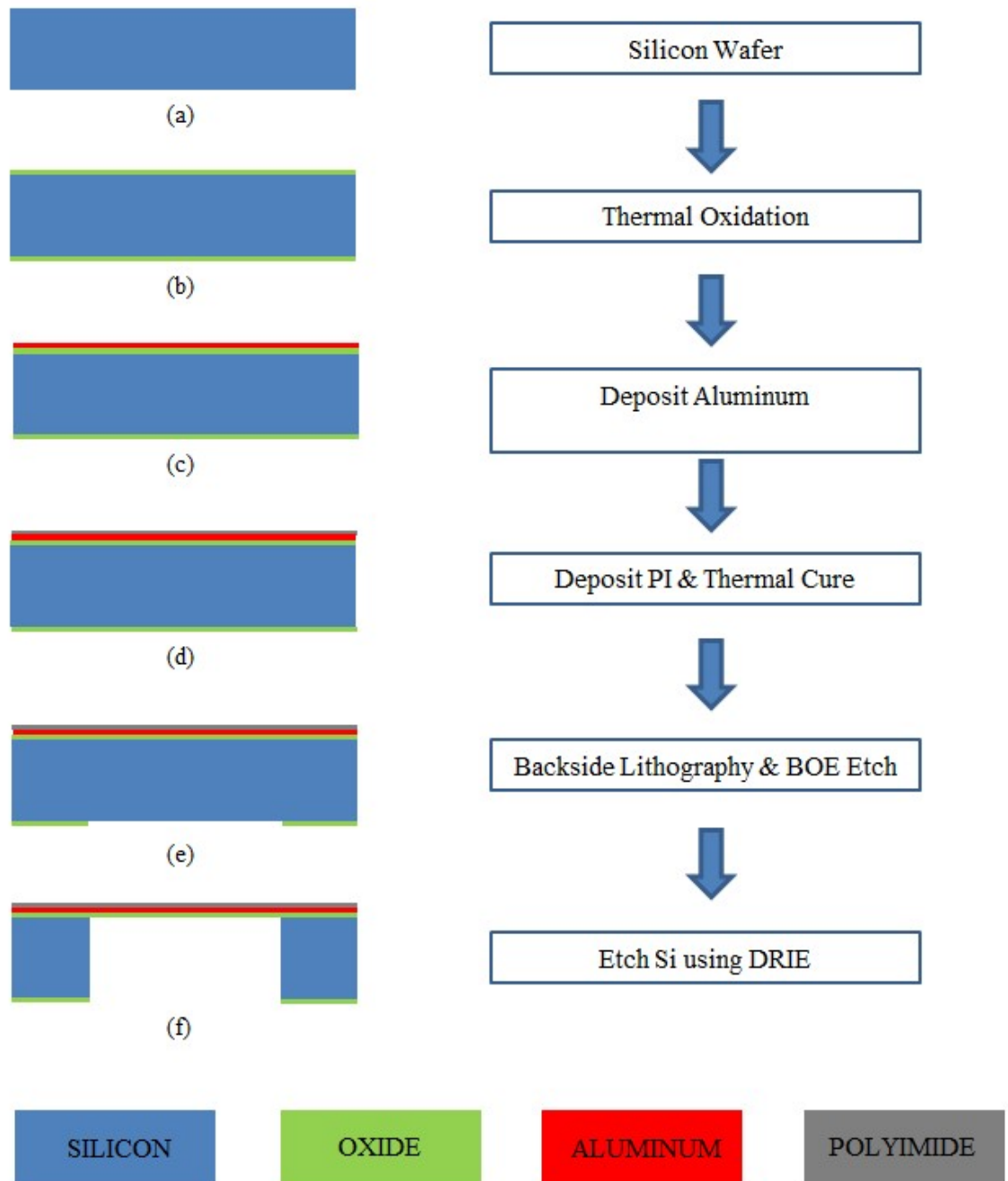


Figure 4.9. Left side: cross sectional view of the device. Right side: fabrication process flow chart.

All the fabrication processing was performed in the class 100/1000 Micro/Nano Technology Cleanroom (MNTC) at the University of Louisville. Details of each of the fabrication steps are described below. An n-type double side polish 4" silicon wafer was used and a micrometer gauge was used to determine the wafer thickness (160 μm).

4.4.1 Wafer Cleaning Process

The first step was to clean the silicon wafer using the RCA Clean method developed by RCA in 1965 [21]. The RCA has four steps designed to remove all foreign contaminants (dirt, scum, silicon dust, etc.) that have built up or been deposited on the wafer during production. This RCA Clean process removes certain contaminants using different chemicals.

The silicon wafer was first immersed in a bath of 6:1:1 $H_2O-NH_4OH-H_2O_2$ at 70°C for 10 minutes followed by washing in DI (deionized) water. This removes organic/ionic contaminations but also results a thin oxide layer which had to be removed by a BOE (Buffered Oxide Etch). BOE is a 1:40 solution of HF and DI water. After BOE etching, the wafer was immersed in a 6:1:1 solution of $H_2O-HCl-H_2O_2$ for at 70°C for 10 minutes to remove metal contamination. It is also followed by washing in running DI water. Finally, it was rinsed and dried using a "Spin Rinse Dryer" (SRD) and transferred into the oxidation furnace.

4.4.2 Thermal Oxidation

The RCA cleaned silicon wafer was loaded into a three-zone tube furnace at 600°C as shown in Figure 4.10(a). Nitrogen gas was introduced to the furnace so that it flows through the furnace until oxidation starts; thus creating an inert clean environment for the

oxidation process. In order to create a high quality oxidation layer, a dry/wet/dry thermal cycle was used and a ramp rate ($20^{\circ}\text{C}/\text{min}$), dwell temperature (1000°C) and dwell time (2 hours) were programmed using the controller. The two dry processes (O_2 gas for 6 minutes) are used to create a higher density (and thus higher quality) SiO_2 layer and the wet oxidation (O_2 gas bubbled through H_2O using a bubbler as shown Figure 4.10 (b)) is used to grow the majority of the SiO_2 layer in a shorter time. A summary of the temperature profile for the whole oxidation process is given in the Figure 4.11. The silicon wafer was removed at 600°C after the oxidation process was completed, and a Filmetrics system was used to determine the thickness of the oxide, which was measured to be $0.45\text{ }\mu\text{m}$.



Figure 4.10. (a) Front view of the three-zone tube furnace (b) Quartz bubbler system for the wet oxidation.

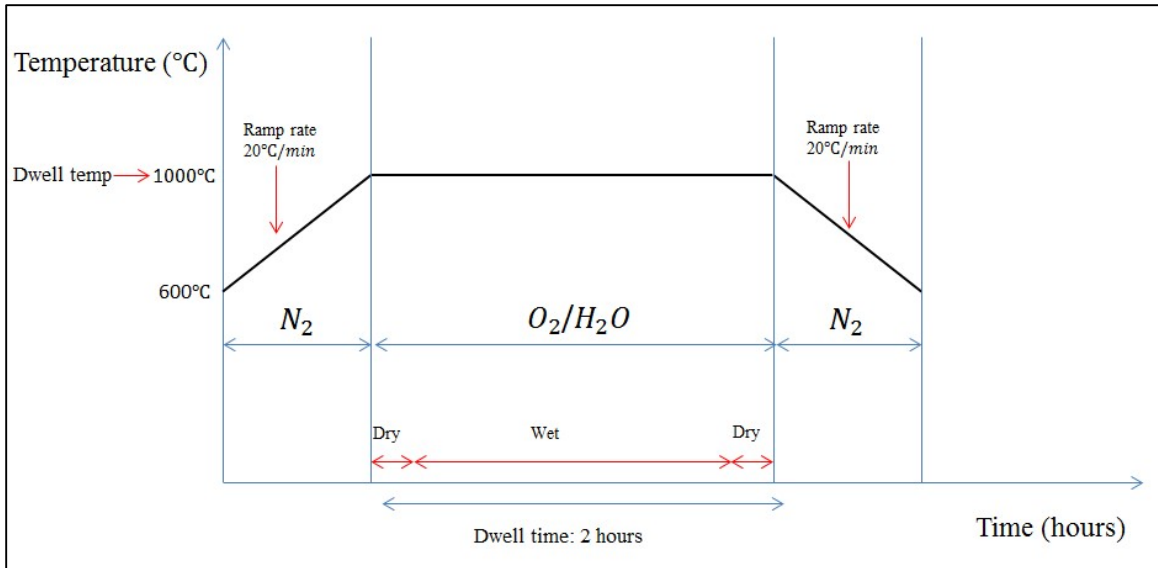


Figure 4.11. Summarized temperature profile for the oxidation process.

4.4.3 Sputtered Thin Film Deposition

Sputtering is a physical vapor deposition (CVD) process whereby atoms are injected from a solid target material due to bombardment of the target by energetic particles. The sputtering process deposits a thin film of a desired material onto the substrate. This is performed by directing ions from a gaseous plasma into the intended target. As the target is bombarded by these ions, they eject target particles onto the substrate. During the sputtering process, the target material and the substrate is placed in a vacuum chamber and a voltage is applied between them so that the target is the cathode and the substrate is attached to anode (see Figure 4.12). The plasma is created by ionizing a sputtering gas which is typically a chemically inert, heavy gas like Argon.

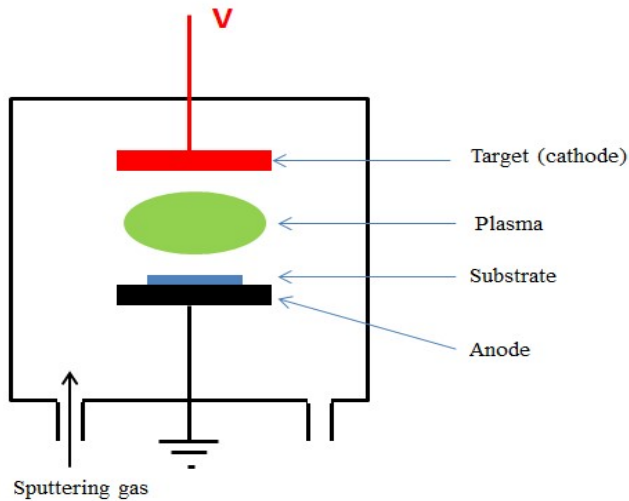


Figure 4.12. Illustration of the sputtering process.

There are a number of ways to improve the deposition rate of the basic sputtering process and a magnetron sputtering system is commonly used for that purpose. This technique applies a strong magnetic field to the dc sputtering system. This magnetic field affects traveling ions to spiral along the magnetic flux lines (thus increasing their effective path length and momentum) and confine the plasma near the target. This will increase the ionization and thin film deposition rate. A magnetron sputtering system was used in this research.

After completing the oxidation process, aluminum was deposited using a 4" diameter pure aluminum (99.995%) target. Sputtering was performed with a PVD 75 RF/DC sputtering system from Kurt J. Lesker as shown in Figure 4.13. For all experiments the power was 300W DC and the pressure was 5 mT while the deposition time varied for each sample to change the thickness of the film. Before each deposition, a pre-sputtering

process was performed to clean the target's surface in case there is an oxide layer or contamination present.



Figure 4.13. PVD 75 RF/DC sputtering system from Kurt J. Lesker. Both 3” and 4” targets can be used in the system and it is capable of co-sputtering.

4.4.4 Polyimide Deposition and Curing

PI 2610 polyimide, which is highly viscous due to its high molecular weight, was selected as the mechanical structural layer. To ensure the wafer was completely dry (thus ensuring the polyimide would correctly adhere) the wafer was placed on a hotplate for a dehydration bake for three minutes at 115 °C. This was done to get rid of the moisture on the wafer and make it ready for the application of the polyimide. Then PI 2610 was spun on the wafer using a Headway Spinner. PI 2610 has the ability to provide a 1.0 to 2.5 μm thick layer by adjusting the spread and spin parameters as shown in Figure 4.14. Spread and spin parameters were adjusted until 1 μm thick polyimide layer was obtained. Table 4.2 shows the optimized parameters.

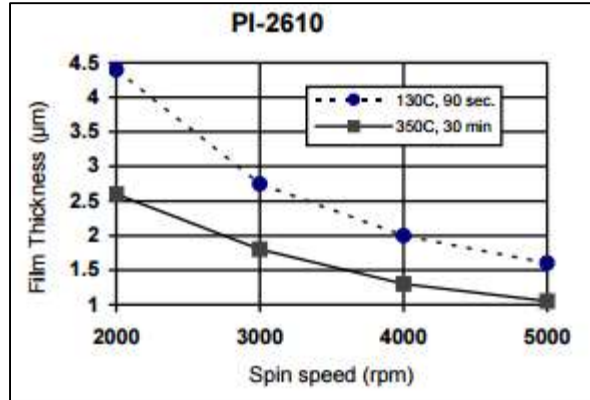


Figure 4.14. Spin speed curve [67]

Table 4.2. Optimized spread and spin speeds to produce 1 µm of Polyimide.

Step	Speed (RPM)	Duration (Seconds)
1 (Spread)	500	10
2 (Spin)	4000	30

After the spin, a soft bake was performed using a hot plate at 130°C for another 3 minutes to remove any solvent from the film. Following the soft bake, the wafer was transferred to a Yes Polyimide Oven, which is a high temperature vacuum oven (can go up to 550°C), for thermal curing. The Yes Polyimide Oven is shown in Figure 4.15. A recipe was created for the curing process and its corresponding temperature profile is given in Figure 4.16. The wafer was loaded at 50°C and cured at 350°C for an hour. The vacuum environment brings about several dehydration cycles to remove oxygen and moisture, and nitrogen gas is supplied throughout the curing process which helps to provide a dry inert atmosphere.



Figure 4.15. Yes Polyimide Oven.

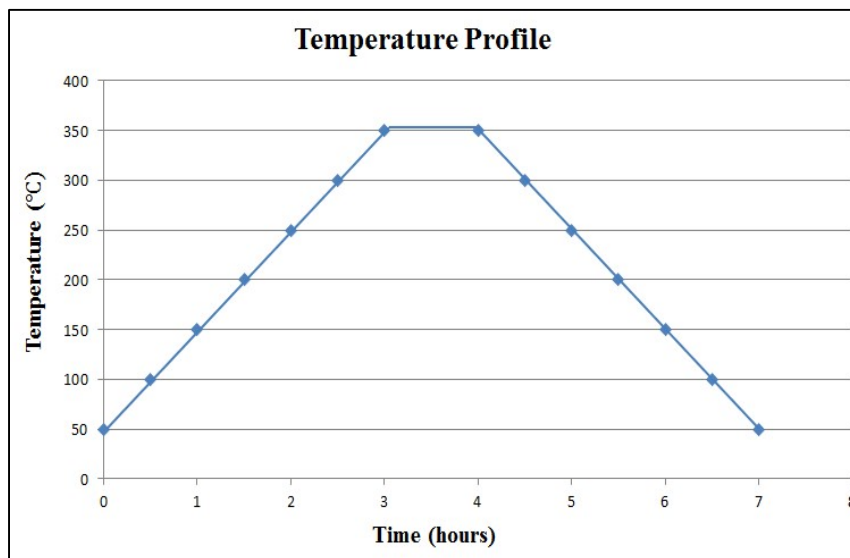


Figure 4.16. Temperature profile of the thermal curing process for the PI2610 polyimide.

4.4.5 Photolithography

Photolithography is one of the most critical processes in the successful fabrication of any microelectronic or MEMS device. Photolithography is the process of transferring a pattern from a photomask onto the surface of a silicon wafer or substrate. The pattern is

transferred via an intermediate photosensitive polymer film called photoresist. Photolithography permits intricate details to be transferred to a substrate and allows multiple devices to be patterned at once. A pattern is laid out by a designer. This pattern is copied and repeated several times onto a photomask. The substrate that will receive the pattern is coated with either positive or negative photoresist (or sometimes simply called resist), depending on the polarity of the design. The photomask is aligned to the wafer, brought into contact with the wafer, and the photoresist is exposed to UV (ultra-violet) light. The wafer is then placed in a developing solution which causes the pattern to appear in the photoresist film. Finally, the pattern is transferred to the underlying material (typically a silicon dioxide layer or a metal layer) by means of a wet or dry etching process.

After completing the curing process, the wafer was transferred to the lithography bay. This lithographic process will open arrays of circular pattern on the backside of the wafer so that silicon can be etched through those opened windows using DRIE to form the diaphragms. First, the wafer was placed on a hotplate at 115°C for three minutes for a dehydration bake. Then AZ4620 photoresist (which was used in Chapter 2) was spun onto the backside of the sputtered wafer using a Headway spinner. Its spread and spin parameters were modified to produce a 5 μm thick resist layer and optimized spread and spin parameters are given in Table 4.3. Then a soft bake was performed for 10 minutes at 100°C on a hotplate which is below the glass transition temperature of the AZ4620. Standard binary lithography was performed using an MA6/ BA6 Suss Mask Aligner (as shown Figure 4.17), which provides the UV light for exposure, and the photomask (containing circular features from 100 μm to 700 μm diameter). Once the sample was

exposed to UV light, AZ400k developer was used to develop the exposed structures, and a QDR (Quick Dump Rinse) and SRD (Spin Rinse Dryer) were used to clean the wafer using DI water. To carry out the hard bake, the patterned wafer was placed on the hotplate at 115°C for one minute. This removes any remaining solvents and hardens the resist, thus improving its ability to function as an etch mask. Finally, the wafer was immersed in BOE (Buffer Oxide Etch) bath for four minutes to etch the oxide, and a QDR and SRD were used to once again clean the wafer.

Table 4.3 Optimized spread and spin speed

Step	Speed (RPM)	Duration (Seconds)
1 (Spread)	500	10
2 (Spin)	4000	30

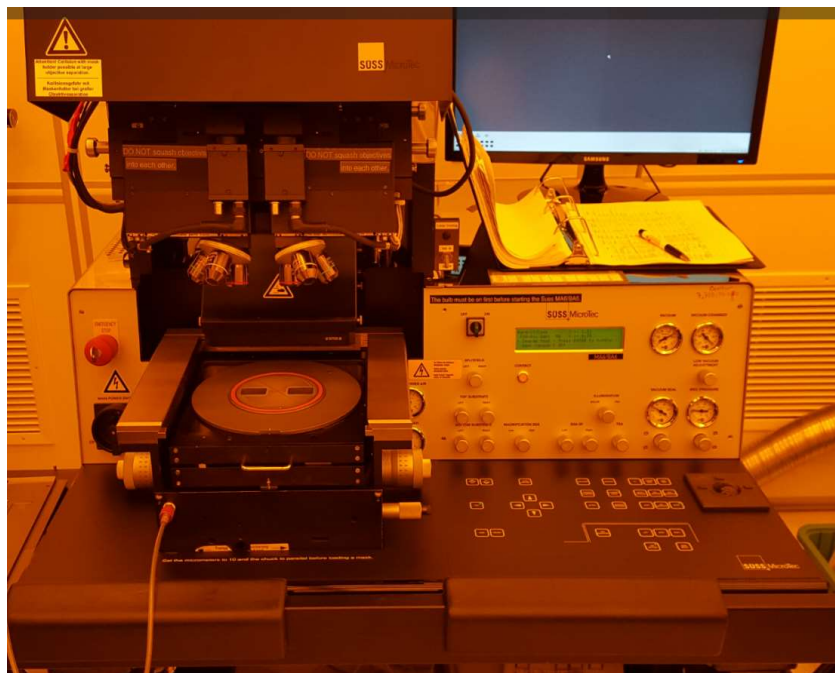


Figure 4.17. SUSS MASK ALIGNER MA6/ BA6.

4.4.6 Deep Reactive Ion Etch (DRIE)

High aspect-ratio deep reactive ion etching (DRIE) is an essential processing step that enables the fabrication of many MEMS devices [70-72]. Especially in the field of silicon bulk-micromachining, anisotropic etching of silicon wafers using DRIE has become an almost industry-standard process.

A DRIE system is a combination of RIE (reactive ion etch) and an ICP (inductively coupled plasma). RIE is mainly used for near surface processing; whereas the ICP allows deeper etching. DRIE anisotropically (vertically) etches the silicon using combinations of etch and passivation dry gasses known as the Bosch process. This technique was patented and licensed by Robert Bosch GmbH in 1994. This is performed using an isotropic plasma etch that bombards the substrate with ions traveling in a vertical direction. After the silicon is initially etched, a passivation layer is conformally coated over the substrate. The etching cycle begins again, but etches only horizontal features causing the vertical sidewalls to remain intact. The etch and passivation cycles repeat until the determined depth is achieved. Sulfur hexafluoride (SF_6) gas is used for the etch cycle, while octafluorocyclobutane (C_4F_8) gas is used for the passivation cycle.

Prior to DRIE etching, the processed wafer was first diced into several samples so more experiments could be conducted. Samples were transferred to the DRIE to etch silicon from the backside. A sample was attached to a handle wafer using polyimide tape and loaded to the DRIE system (see Figure 4.18). A summarized recipe is given in Figure 4.19 which includes gas flow setup, power setup, switching cycle time, chamber pressure, and temperature set points for both the etch and passivation cycles. This DRIE process

was continued until it reached the top etch stop layer, which was the thermal oxide layer. A Dektak profilometer was used to measure the depth.



Figure 4.18. STS DRIE Etcher.

Once the diaphragm was released using DRIE, the internal compressive stress of the released diaphragms caused them to buckle, producing smooth uniform domed structures. A Zygo 3D optical interferometer, optical microscope, and a Dektak profilometer were all used to observe the buckled profiles. A custom microscope heat stage was used to examine the temperature dependence of the devices.

Gas flow setup

Gas	Etch cycle		Passivation cycle	
	Flow(sccm)	Tol(%)	Flow (sccm)	Tol (%)
C ₄ F ₈	0	5	85	5
SF ₆	130	15	0	5
O ₂	13.0	15	0	5
Ar	0	5	0	5

Power setup

Sources	Etch cycle	Passivation cycle
13.56MHz generator	800 W	800 W
Platen generator	12 W	0 W

Switching cycle time

	On time	Overrun
Etch	9s	1
Passivation	5s	1

Chamber Pressure

Etch	Passivation
42 mT	32 mT

Temperature set points

Platen Temperature set point	15°C
Chamber Lid temperature set point	45°C

Figure 4.19. Recipe of DRIE for Si etch process.

4.5 Results and Discussion

4.5.1 Oxide -PI Diaphragms

These Oxide-PI diaphragms were fabricated using 0.45 μm thick oxide and 1.7 μm thick polyimide and structures were released from the back using DRIE as explained in Section 4.4. Around 10-15% of diaphragms were buckled down and rest of them were buckled up at room temperature as shown in Figure 4.20. The equations discussed in Section 4.2 were used to predict the diaphragm buckling height at room temperature and the critical stress required for buckling. The analytical predictions are then compared with experimental results in the following section.

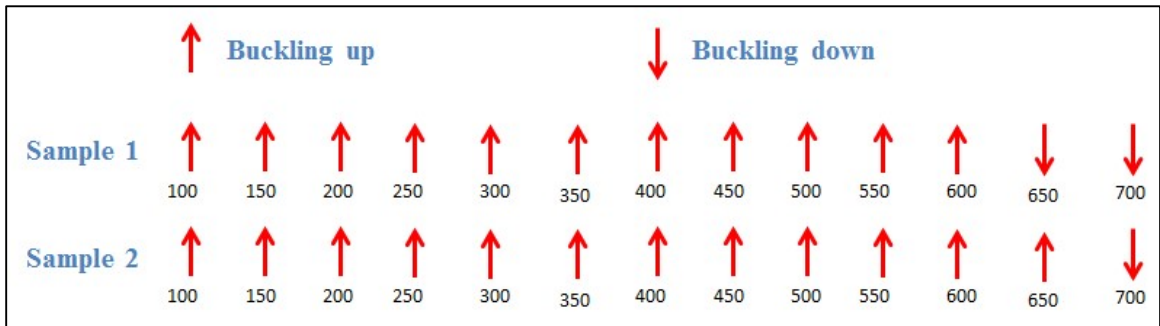


Figure 4.20. Buckling map: shows the buckling direction of released diaphragms.

Derived equations in Section 4.2 were developed for a single layer diaphragm of uniform material properties, therefore for a bilayer system; “effective” value needs to be determined for such mechanical properties as residual stress, Young’s modulus and Poisson’s ratio. These effective values can then be substituted into the previously-derived equations. Since this diaphragm was composed of polyimide and oxide, the following equation was used to find the effective in-plane Young’s Modulus [19].

$$Y_{eff} = \left(\frac{t_{SiO_2} \times Y_{SiO_2} + t_{PI} \times Y_{PI}}{t_{SiO_2} + t_{PI}} \right) \quad 4.26$$

where;

t_{SiO_2} = Oxide thickness (μm)

Y_{SiO_2} = Young's modulus of silicon dioxide (73×10^9 Pa) [62, 63]

t_{PI} = Polyimide thickness (μm)

Y_{PI} = Young's modulus of polyimide (8×10^9 Pa)[73]

Using the above mentioned parameters, the effective Young's modulus was calculated to be **20.53×10^9 Pa** for our sample.

Similarly the effective residual stress of the oxide-polyimide diaphragm was calculated using equation 4.27 [74].

$$\sigma_{eff} = \left(\frac{t_{SiO_2} \times \sigma_{SiO_2} + t_{PI} \times \sigma_{PI}}{t_{SiO_2} + t_{PI}} \right) \quad 4.27$$

where;

σ_{SiO_2} = Stress in the oxide film (MPa)

σ_{PI} = stress in the polyimide film (MPa)

The polyimide (PI-2610) is a stress free material according to the manufacture specifications [67]. Therefore, the value of stress was considered to be zero for this calculation. A Toho FLX-2320-S stress analyzer was used to determine the internal stress of the thermal oxide, and it was measured to be **-275 MPa**. These values were then

substituted into the equation 4.27 to determine the effective residual stress on the bilayer, which was calculated to be **-57.56 MPa**. Both Poisson's ratios of oxide and polyimide were found to be nearly identical, so the **effective Poisson ratio was 0.2**. These effective values of the material properties of the bilayer film were used in the calculations to determine the buckling height and the critical stress required for buckling.

The initial buckle height was measured using a Zygo profilometer and then vacuum was applied underneath individual diaphragms to test their bistability. Equation 4.20 was used to calculate the initial buckling height for each diaphragm. Figure 4.21 shows a comparison of the experimental and theoretical buckling height of each diaphragm, as well as their regions of bistability determined by the vacuum test. While all diaphragms tested would buckle and change states when vacuum was applied, not all the samples exhibited bistability, meaning that not all samples would remain in their 2nd bistable state when vacuum was removed. Some of the samples would immediately return to their original buckled condition. Those samples were labeled as being **not bistable**. The diaphragms with diameter from 300 μm to 700 μm were found to be bistable with applied vacuum, whereas the diaphragms with diameters from 100 μm to 250 μm were not.

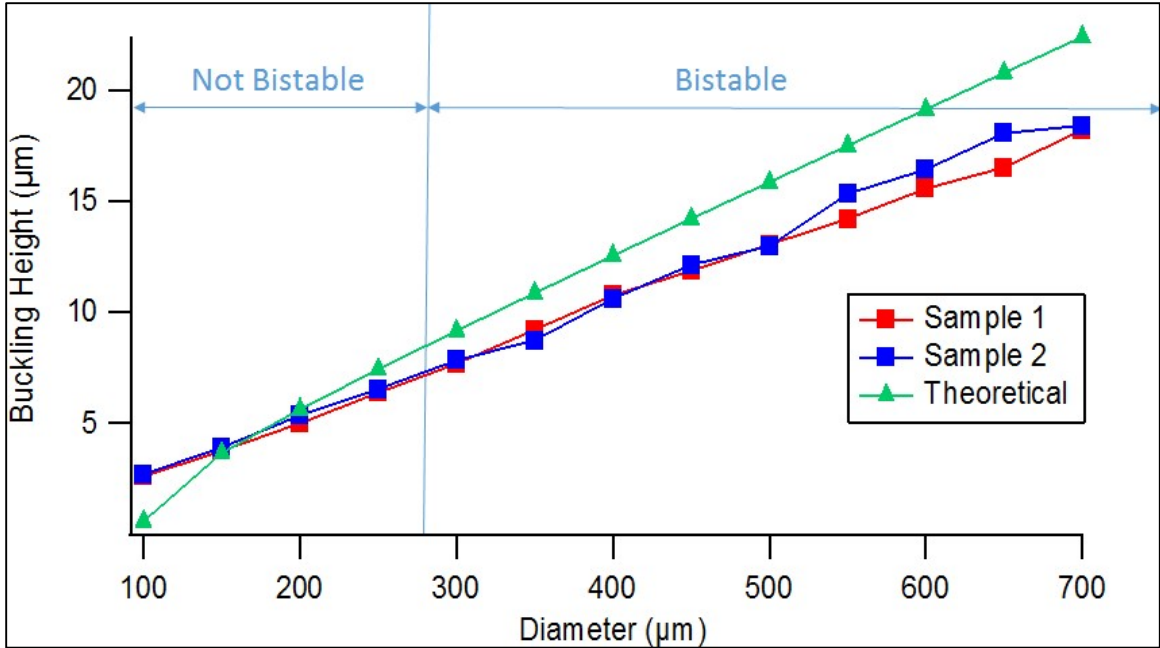


Figure 4.21. Comparison of experimental and theoretical buckling height vs. diaphragm diameter for $0.45\mu\text{m}$ oxide/ $1.7\mu\text{m}$ polyimide diaphragms. The bistability region labeled in the figure was determined experimentally by applying vacuum to the diaphragms.

Equation 4.18 introduced the critical stress term, which is a significant factor for buckling. Critical stress should be less than the residual stress so that the residual stress to critical stress ratio is always greater than one [55]. When the ratio is greater than one, the magnitude inside the square root of Equation 4.20 becomes positive and the diaphragms will buckle. Figure 4.22 compares the variation of residual stress and critical stress to diaphragm diameter. If the critical stress for each diaphragm is always less than the residual stress, it will accomplish the requirement for buckling. These results confirm our experimental observations. If the critical stress exceeds the residual stress (i.e. the residual stress to critical stress ratio is less than one) the height becomes an imaginary value and the diaphragms do not buckle according to the theoretical calculation. Figure

4.22 predicts that diaphragms with a diameter less than 100 μm will never buckle. Unfortunately, our photomask did not include designs less than 100 μm in diameter.

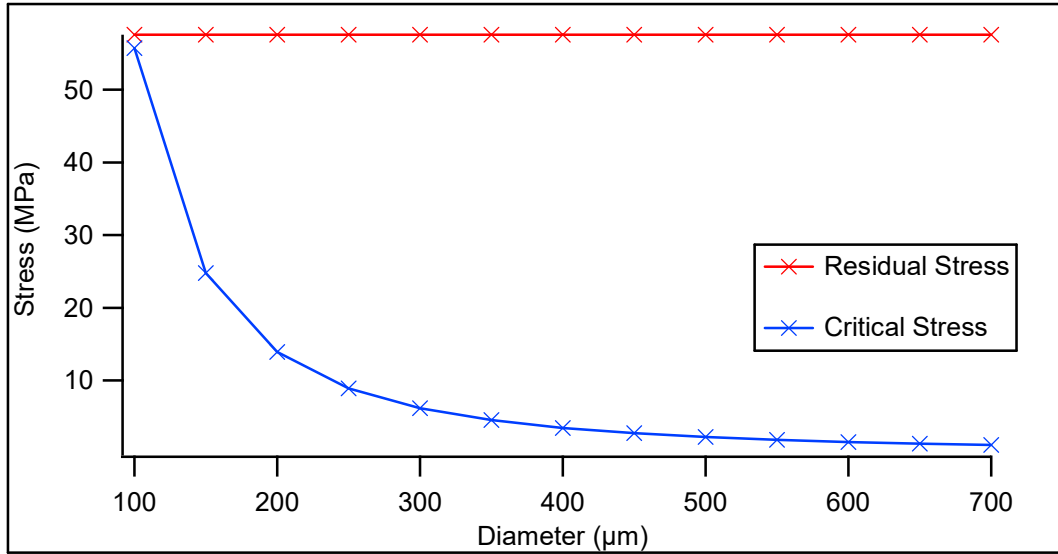


Figure 4.22. Residual stress and critical stress vs diaphragm diameter.

4.5.2 Oxide-Al diaphragm

A polyimide layer was not used for this fabrication experiment. Instead we explored the possibility of using a thick aluminum layer as a structural layer in place of the polyimide. The diaphragm bilayer was composed of 0.45 μm thick oxide layer and a variable thickness of aluminum. We experimented with various thicknesses of aluminum until we observed buckling. When the aluminum thickness was 0.45 μm and 0.675 μm , the aluminum thicknesses were not enough to produce dome-like buckled structures for the larger diameter diaphragms because it created in a fragile and non-uniform dome with a wrinkled pattern on its surface due to compressive stress as shown in Figure 4.23.

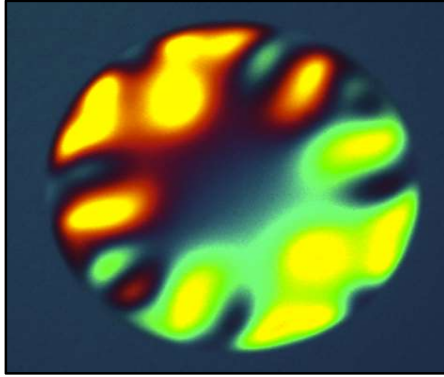


Figure 4.23. Optical image of a buckled diaphragm with a non-uniform wrinkled profile (DIC and brightfield illumination).

Figure 4.24 further explains this phenomenon by introducing a new term “dome factor” which is defined as “1” when the diaphragm produces smooth dome-like buckled structures, and “0” otherwise. A 0.90 μm thick aluminum was found to produce dome-like buckle diaphragms for all the structures, therefore diaphragms with 0.90 μm thick aluminum were studied here.

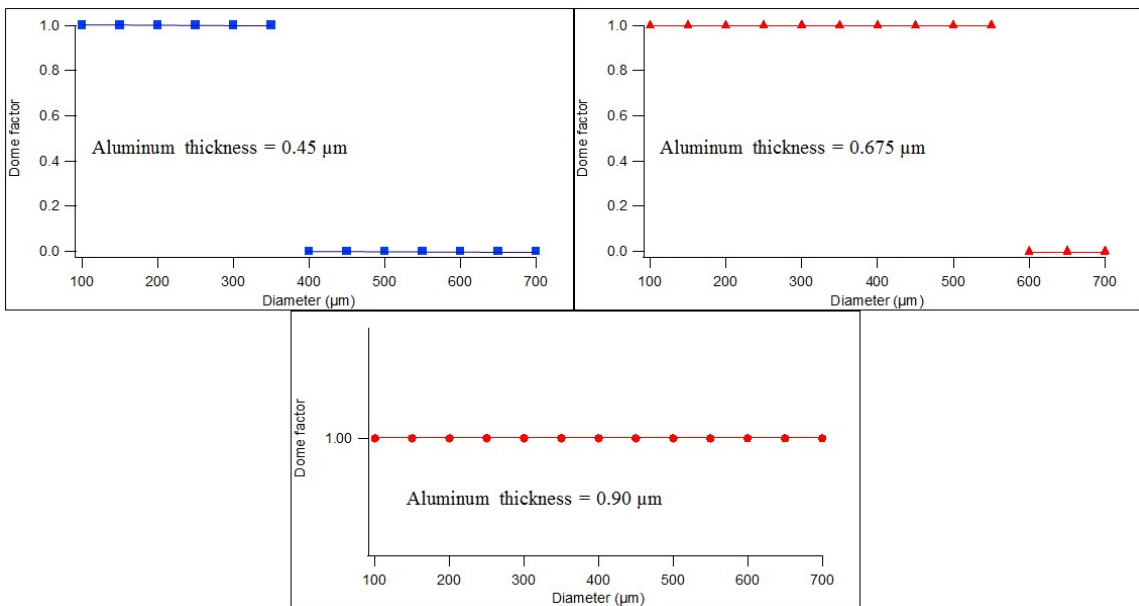


Figure 4.24. Dome factor vs. diameter of the diaphragm.

Once the **.45 μm oxide/9 μm Al** structures were released from the back using DRIE (as explained in Section 4.4), about 80% of diaphragms were buckled down and the rest of the structures were buckled up at room temperature. It was noticed that the larger diameters tended to buckle down, whereas the smaller diameters diaphragms tended to buckle up as shown in Figure 4.25.

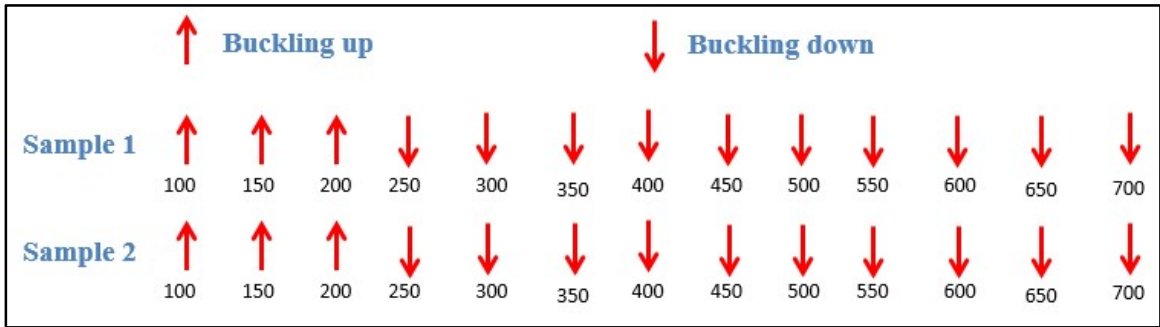


Figure 4.25. Buckling map: shows the buckling direction of released diaphragms.

As done in the previous section, the initial buckle height was measured using a Zygo profilometer and then a vacuum was applied on individual diaphragms to test their bistability. Equation 4.20 was used to calculate the initial buckling height for each diaphragm. Figure 4.26 compares the experimental and theoretical buckling height of each diaphragm and shows the experimentally-determined bistability region. The 200 μm to 700 μm diameter diaphragms were found to be bistable with the applied vacuum, while diameters below 150 μm do not show bistable behavior.

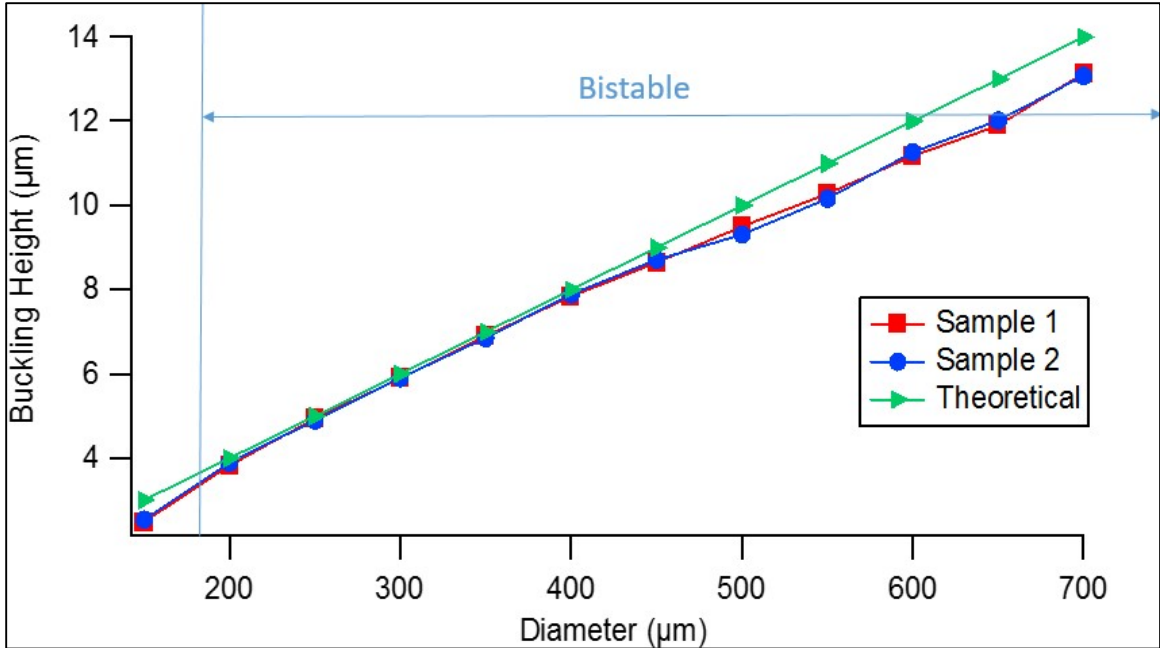


Figure 4.26. Comparison of experimental and theoretical buckling height vs. diaphragm diameter for .45 μm oxide/.9 μm aluminum diaphragms. Also shown is the experimentally-determined bistability transition point vs. diaphragm diameter.

A Linkam THMS600 Thermal Stage was used to heat the samples. This thermal stage was placed on an optical microscope stage to observe the diaphragms. Figure 4.27 shows optical images of the buckled diaphragm using the DIC (differential interference contrast) feature of an Olympus BX 51 high-power optical microscope. As the diaphragm flips to its complementary stable state, one can observe an interesting change in the color pattern of the image and from that determine the direction of buckling (buckling up/down). This technique was used to observe the state of the diaphragm while raising the temperature. However, none of the diaphragms switched from its 1st stable state to its 2nd stable state when the temperature was increased up to 150°C.

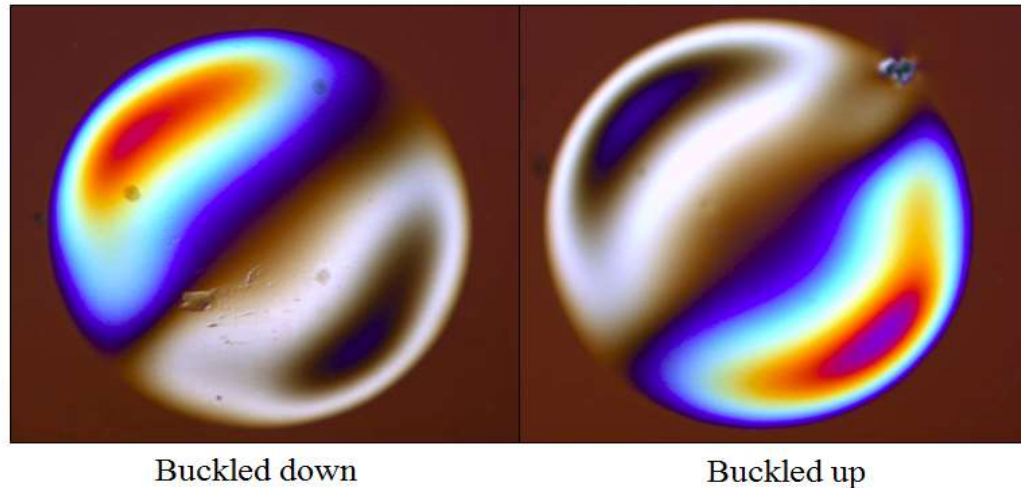


Figure 4.27. Optical images of the buckled diaphragm using DIC and brightfield illumination.

Next, the diaphragms were observed using the Zygo profilometer instead of the optical microscope to study the topology of the diaphragm with increasing temperature. Buckled diaphragms with larger diameter (above 450 μm) had a fragile, wrinkled pattern on their diaphragms while the smaller diameters produced nice uniform dome-like buckled structures as shown in Figure 4.28 (left). This was attributed once again due to increasing compressive stress on the composite film with raising temperature. To test this hypothesis, the stress on a single aluminum film and the stress on the bilayer film (oxide/aluminum) were studied using the Toho Thin Film Stress Measurement System (KLA Tencor FLX-2320, USA). Figure 4.29 presents the resulting measured stress on (a) a single aluminum film which was deposited on top of the oxidized wafer and (b) the stress on the bilayer film (oxide/alum) while raising the temperature up to 150°C. The initial stress on the aluminum is **+56 MPa** (i.e. right after the deposition), and the film

gets more compressive with increasing temperature as shown in Figure 4.29 (i.e. stress value goes negative with increasing temperature).

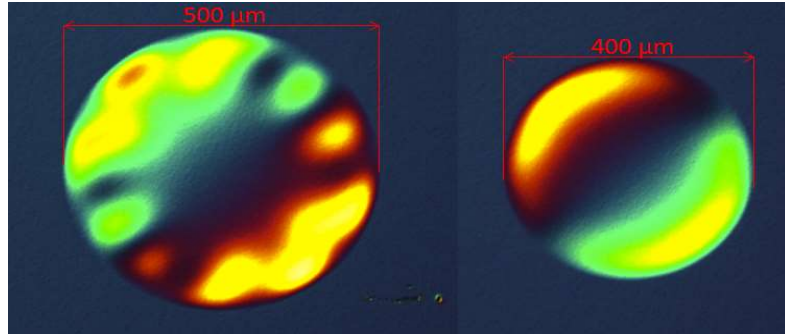


Figure 4.28. Optical images of 500 μm and 400 μm in diameter buckled diaphragms using DIC and brightfield illumination.

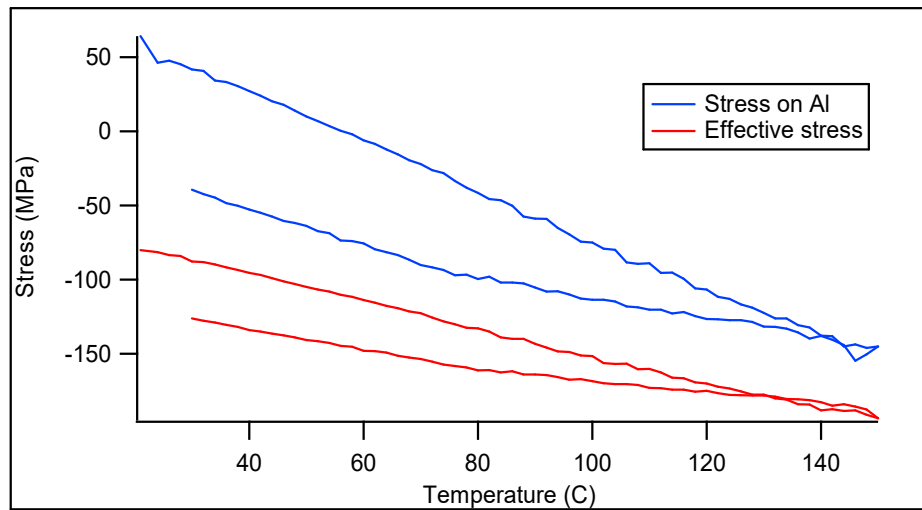


Figure 4.29. Measured stress in the 0.90 μm aluminum film (deposited on top of the oxide) in blue, and the measured stress in the bilayer film (0.45 μm oxide/0.90 μm alum) in red as a function of temperature.

Samples were further heated by increasing the temperature up to 300°C using a hot plate. After the heat treatment, the profiles of the diaphragms were measured using the Zygo

Profilometer. These measurements were taken once the sample cooled back to room temperature. Figures 4.30 to 4.34 show the 3D and cross sectional profiles of the diaphragms before and after the 300 °C heat treatment. The elevated heat treatment caused the buckle heights of the larger diameter diaphragms (650 μm , 600 μm and 550 μm) to be dramatically reduced producing very insignificant initial deflections (1-2 μm) at room temperature (Figures 4.30 to 4.34). This was attributed due to the reduction of the initial compressive stress on the oxide/alum bilayer due to the elevated heat treatment. However, interestingly enough, the smaller diameter diaphragms (200 μm and 150 μm) were able to remain dome-like and buckled even after the elevated heat treatment, although their buckle height was reduced by about 50% by the heat treatment (Figures 4.33 and 4.34). This indicated that the composite bilayer film retained enough compressive stress through the heat treatment to allow nice buckling!

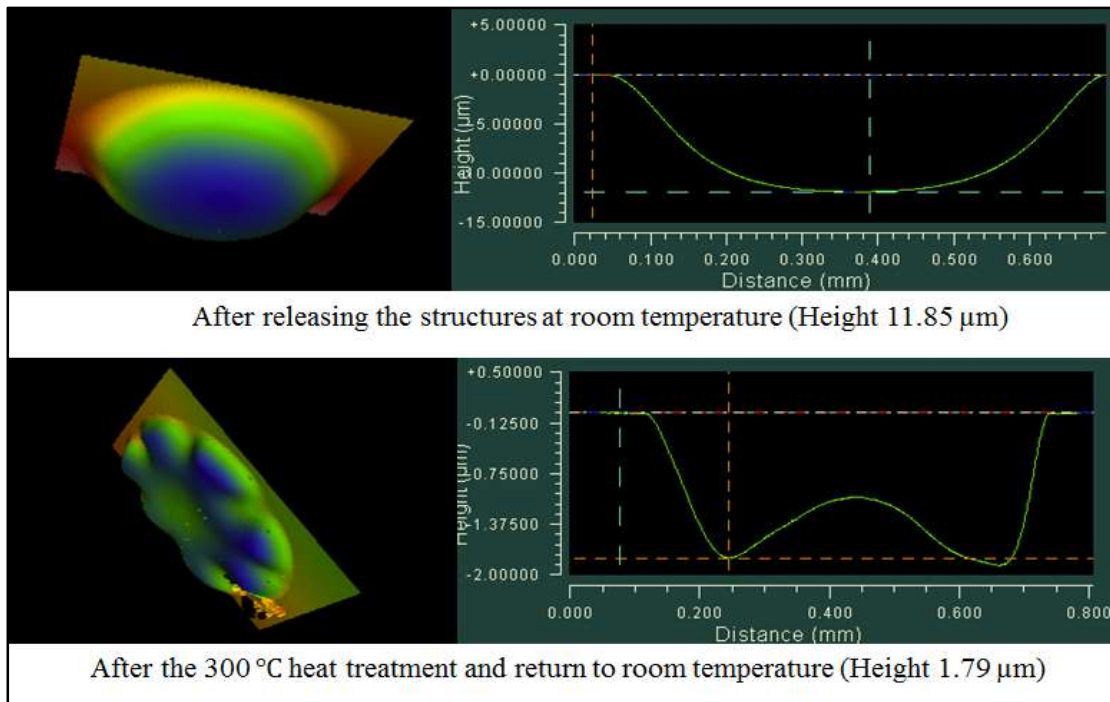


Figure 4.30. 3 dimensional and cross sectional view of 650 μm oxide/alum diaphragm.

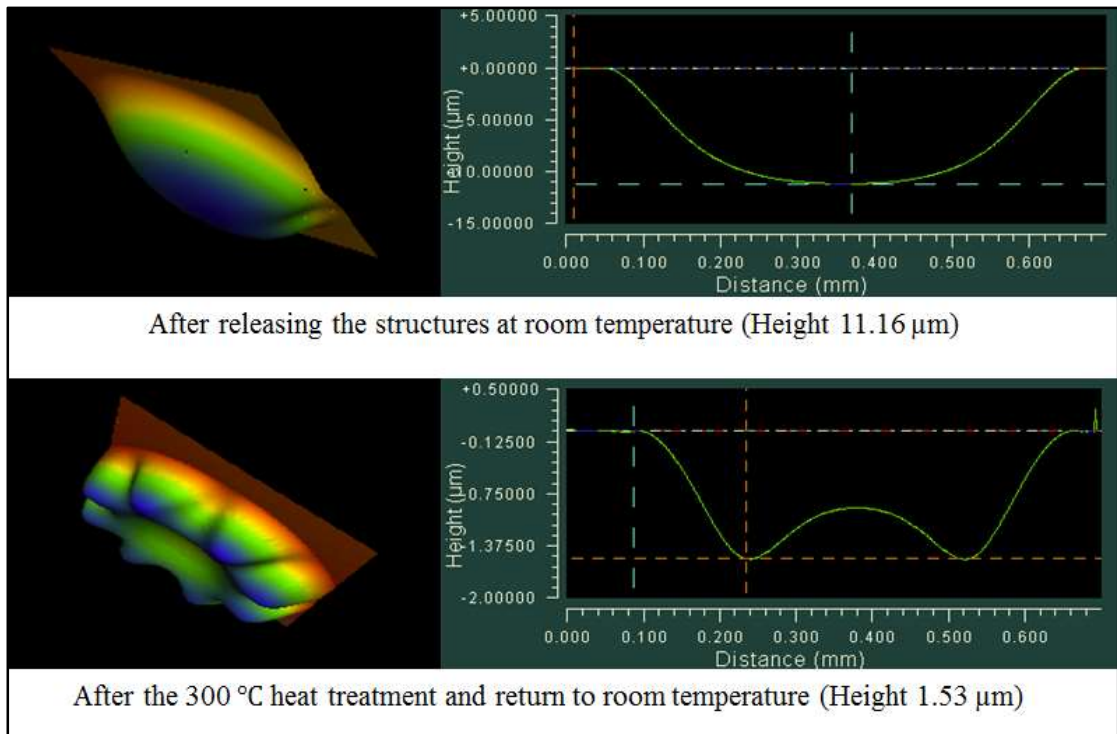


Figure 4.31. 3 dimensional and cross sectional view of 600 μm oxide/alum diaphragm.

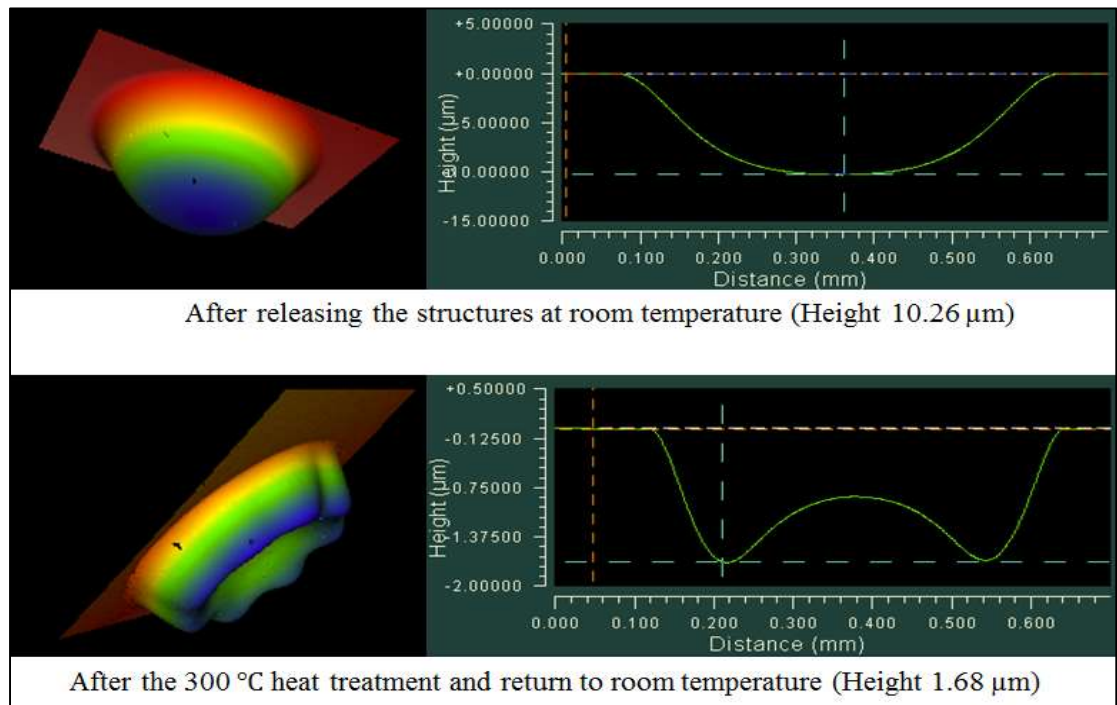


Figure 4.32. 3 dimensional and cross sectional view of 550 μm oxide/alum diaphragm.

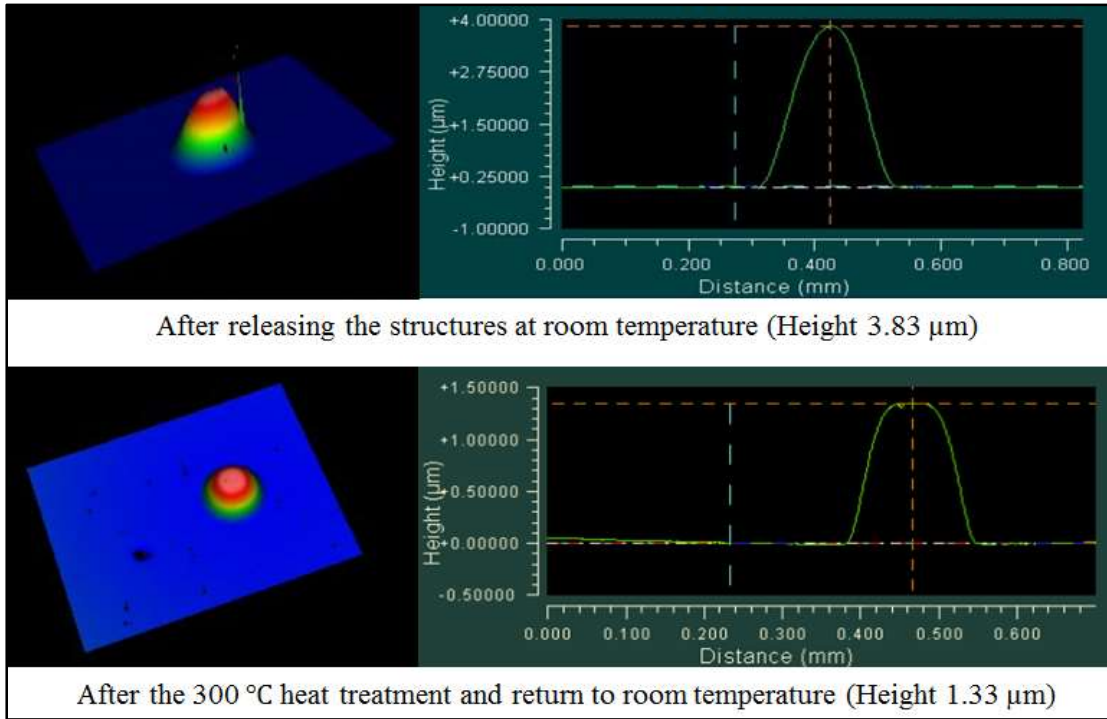


Figure 4.33. 3 dimensional and cross sectional view of 200 μm oxide/alum diaphragm.

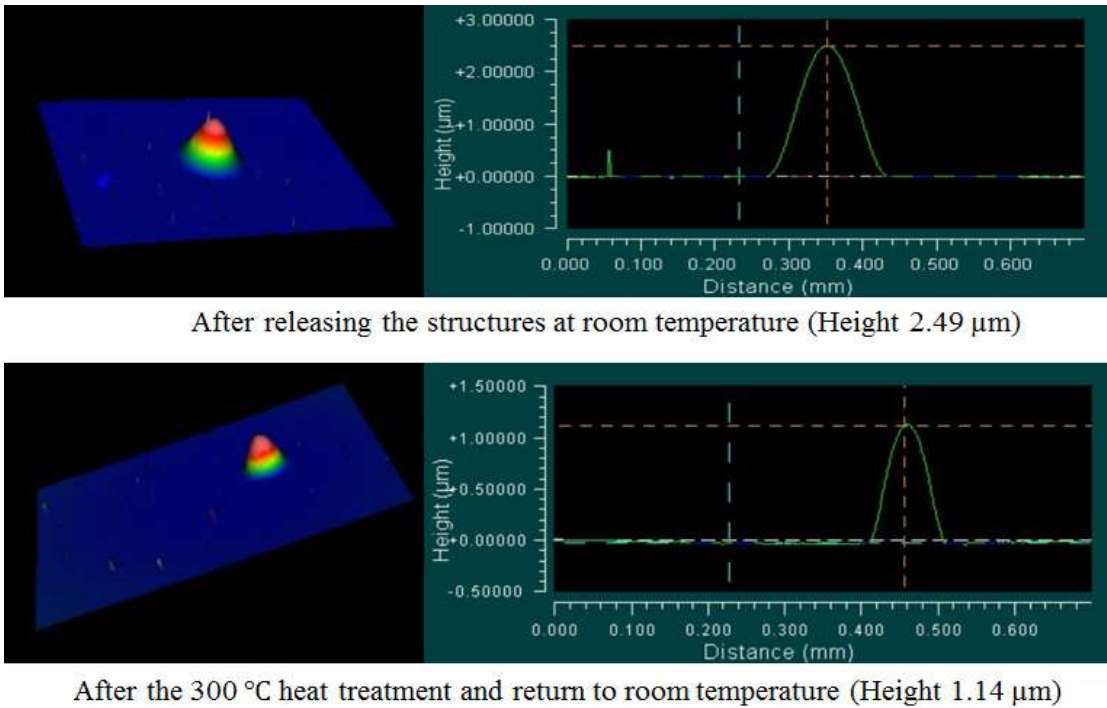


Figure 4.34. 3 dimensional and cross sectional view of 150 μm oxide/alum diaphragm.

To test the above discussed hypothesis, the same sample which was used to analyze stress on the aluminum film (0.90 μm) which was deposited on thermal oxide (0.45 μm) was annealed at 350°C for one hour using forming gas atmosphere ($H_2 = 3 \text{ sccm}$ and $N_2 = 34 \text{ sccm}$). After that, stress on the aluminum was further studied using the Toho Thin Film Stress Measurement System and the results are shown in Figure 4.35. The 350°C heat treatment caused the stress in the aluminum film to become much more tensile (blue curve in Figure 4.35), and that led to switching the effective stress on the bilayer from compressive to tensile. According to the literature, aluminum films reach their limit of their elastic region around 150°C, and then the films tend to be compressive after 150°C [69]. Once the elastic region is exceeded, irreversible deformation of the aluminum occurs. This causes the aluminum film to have a higher tensile stress when it is cooled back to room temperature after the annealing process.

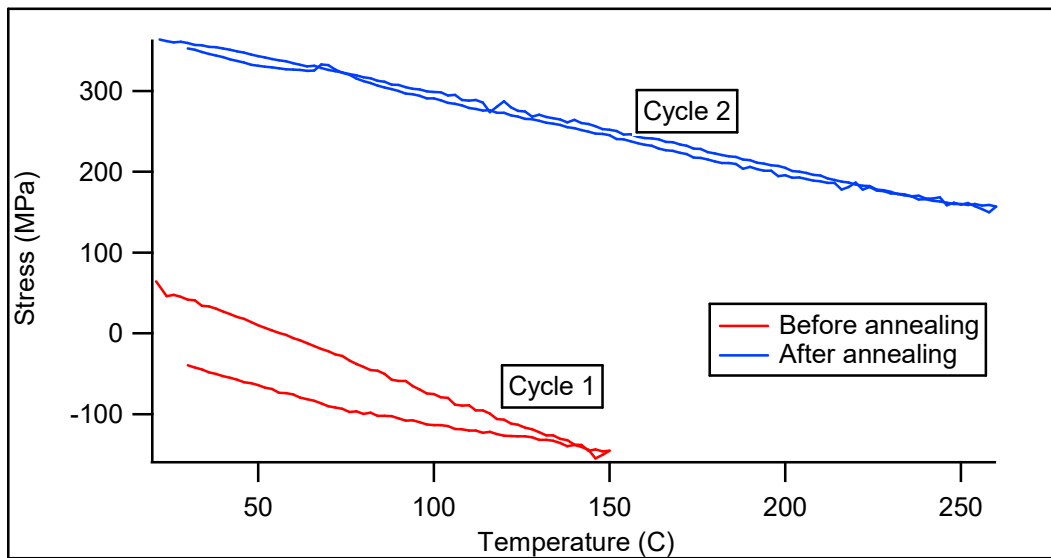


Figure 4.35. Stress as a function of temperature for sputtered aluminum.

4.5.3 Oxide-Al-PI diaphragm

Due to inability to create smooth domes that would survive temperature testing using just aluminum and oxide, we decided to add a polyimide layer to serve as a stress-free temperature-insensitive mechanical structure. These Oxide-Al-PI diaphragms were fabricated using 0.45 μm thick oxide, 0.5 μm thick aluminum and 1 μm thick polyimide. The trilayer structures were released from the backside using DRIE as explained in Section 4.4. Interestingly enough, none of the diaphragms appeared to buckle at room temperature upon their release. However, a very small deflection (0.1 μm to 0.2 μm) was measured using the Zygo profilometer. Then the Linkam THMS600 Thermal Stage was used to heat the samples, and the Zygo profilometer was used to observe the deflection of the diaphragms. The sample was heated up to 150 $^{\circ}\text{C}$ which is the limit of the elastic region for aluminum. The ramp rate was 5 $^{\circ}\text{C}/\text{min}$ and displacement was recoded every 5 $^{\circ}\text{C}$. The Figure 4.36 shows height of the diaphragm as a function of temperature for the diaphragm with diameter 550 μm .

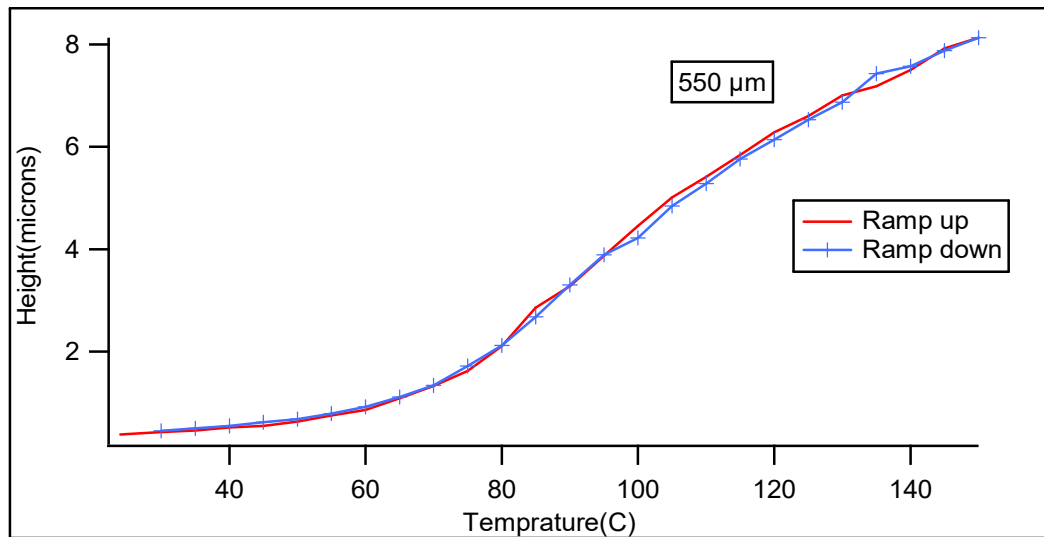


Figure 4.36. Height of the Oxide-Al-PI diaphragm as a function of temperature.

The height of the diaphragm gradually increased with raising temperature and returned to its original position upon cooling as shown in the Figure 4.36, exhibiting very little hysteresis. The profiles of the diaphragms were similar to a smooth buckled diaphragm as shown in Figure 4.37, but no sudden deflection of the diaphragms was observed with raising temperature.

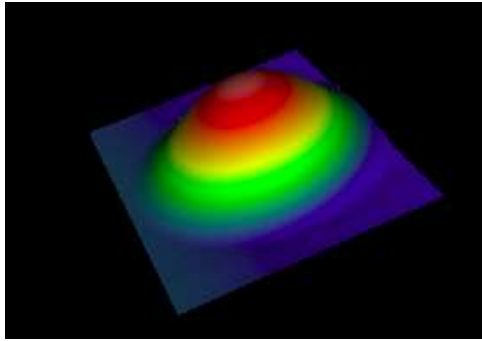


Figure 4.37. Profile of the diaphragm (550 μm) at 125°C.

Another sample was fabricated with the same composition except an aluminum thickness of 0.30 μm was used instead of 0.5 μm to reduce stiffness of the diaphragm. Interestingly enough, all of these structures buckled with about 40% of diaphragms buckled up and the rest of them were buckled down at room temperature. The stress in the thermal oxide and sputter deposited Al was determined to be **-275 MPa** and **+40 MPa** respectively using the Toho Thin Film Stress Measurement System. Equation 5.27 was then used to calculate the effective stress of the trilayer diaphragm to be **-63 MPa**.

The initial buckle height was measured using the Zygo profilometer and then vacuum was applied on individual diaphragms to test their bistability. Equation 4.20 was used to calculate initial buckling height for each diaphragm. Figure 4.38 compares the experimental and the theoretical buckling height of each diaphragm and shows the

bistability region. The diaphragms are found to be bistable with the applied vacuum from 300 μm to 700 μm while they do not show bistable behavior below 300 μm .

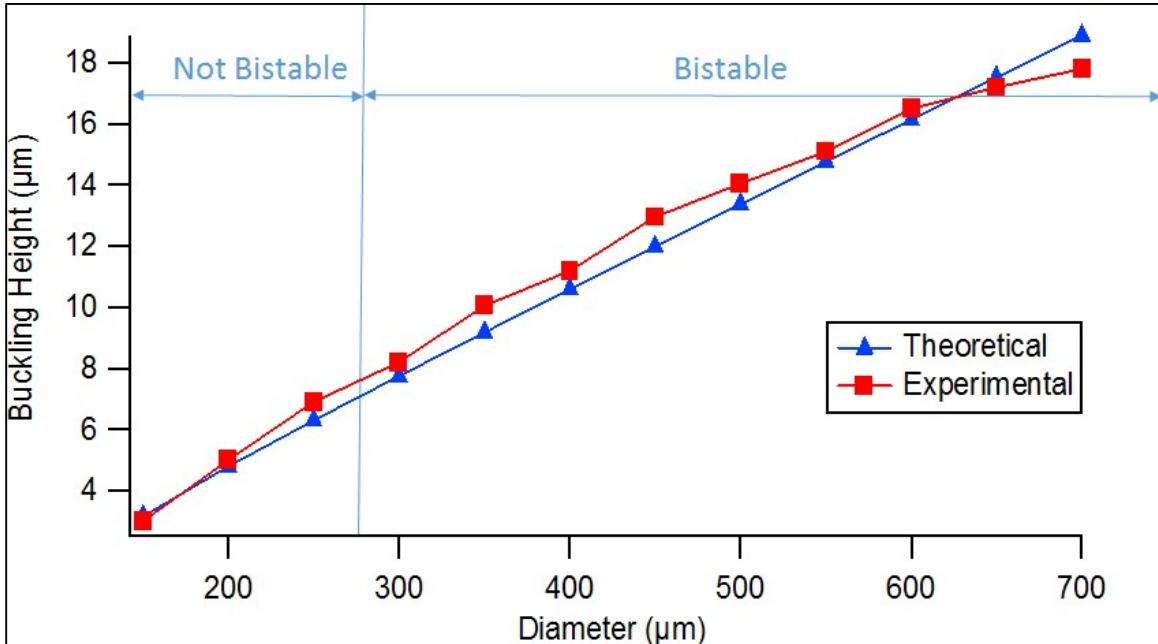


Figure 4.38. Comparison of experimental and theoretical buckling height vs. diaphragm diameter for 0.45 μm oxide/0.5 μm alum/1 μm PI diaphragms. Also shown is the experimentally-determined bistability transition point vs. diaphragm diameter.

Next the Linkam THMS600 Thermal Stage was used to heat the samples and placed on an optical microscope stage to observe the diaphragms. About 50% of the 400 μm diameter diaphragms switched its state from buckled down to buckled up with raising temperature. The switching temperature was between 100 $^{\circ}\text{C}$ to 110 $^{\circ}\text{C}$. **This was our first observation of temperature induced bistability!** However, this appeared to be a onetime effect, as the process was not repeatable for those diaphragms tested. The buckling height of the other diaphragms further increased with raising temperature, and those diaphragms didn't switch their state. *While not a complete success, this proved to*

be an encouraging partial success and the 1st step towards a temperature sensitive bistable domed actuator.

We next modeled the predicted thermal actuation temperature for our successful 400 μm diameter diaphragms to compare with the above experimental result. The predicted buckling height of the 400 μm diameter diaphragm is **10.58 μm** using equation 4.20. Furthermore, the height of the buckled diaphragm at the point of snapping (h_{snap}) is calculated to be **6.11 μm** using equation 4.22.

The residual stress of the diaphragm is changed as a function of the temperature. Equation 4.20 can be modified to calculate the temperature at which the diaphragm buckles (i.e. when the buckling height becomes 6.11 μm). The total residual stress on the diaphragm contains two major components and they are the initial effective stress and the thermal stress due to CTE (coefficient of thermal expansion) mismatch between aluminum and thermal oxide. As discussed in Section 4.3, the CTE of aluminum is $23 \times 10^{-6} K^{-1}$, and it is higher than the CTE of the oxide. When the temperature is introduced to the diaphragm, the aluminum layer attempts to expand at a much faster rate than the oxide layers. This thermal stress of the film can be calculated using equation 4.28.

$$\sigma_{Thermal} = \left(\frac{Y}{(1-\nu)} \right)_{Al} * (\alpha_{Al} - \alpha_{Oxide}) * \Delta T \quad 5.28$$

where;

$$\alpha_{Al} = \text{CTE of Al } (23 \times 10^{-6} K^{-1})$$

$$\alpha_{Oxide} = \text{CTE of thermal oxide } (0.5 \times 10^{-6} K^{-1})$$

$Y = \text{Young's modulus of Al } (70 \times 10^9 \text{ Pa})$

$\nu = \text{Poisson ratio of Al } (0.33)$

The actuation temperature required for snapping the diaphragm from its 1st stable state to 2nd stable state was determined by combining equations 4.20 and 4.28. The predicted actuation temperature was determined to be **44.31 °C** (assumed room temperature is 25°C).

Our experimental result of 100 °C was off by about a factor of approximately 2 from this theoretical prediction and this was attributed to not patterning the aluminum layer on the oxide film. Since the aluminum was deposited on the entire the wafer including the compressed area which is located at the edge of the diaphragm, it can affect the boundary conditions and assumptions made in developing the modeling equations, resulting in possibly a higher experimental temperature to switch its state. Literature described a similar behavior for Al/Si clamped, bimetallic beams where the sides and ends of the beams were free of aluminum [56, 75]. In that case, the upward deflection of the beam nearly doubled by removing the aluminum in the compressed areas. Their recommendation was to pattern the aluminum film so it only appears in the center of the diaphragm, leaving the edges of the diaphragm free of aluminum [56, 75]. This should result in a higher buckling height and improve the bistability of the diaphragms. This will be further discussed in the Recommendation Section of this research.

CHAPTER V

CONCLUSIONS AND RECOMMENDATIONS

This research investigated different materials and processing strategies for designing and fabricating a MEMS-based bistable thermal actuator. This included a material study for engineering compressive stress in candidate thin films that would uniformly buckle upon their release. Techniques for depositing stress free candidate materials were also explored along with processing strategies for forming three-dimensional templates onto which those films could be deposited for creating stress free bistable elements. Finally, lessons learned from the above investigations were implemented to fabricate and test a novel bistable domed-shaped thermal actuator.

5.1 Conclusions

With regard to the initial material study for engineering stress in candidate thin film materials for potential use as bistable mechanical element, silicon nitride and amorphous silicon were investigated using PECVD (plasma enhanced chemical vapor deposition). Novel strategies and custom processing recipes were developed to tune the intrinsic stress in these two materials from compressive to tensile, including stress free. For the case of PECVD deposited silicon nitride, the high frequency pulse time deposition parameter was adjusted from 55% to 100% producing films ranging from -870 MPa compressive to 274

MPa tensile respectively. Stress free PECVD silicon nitride thin films were obtained with a high frequency pulse time of 85%. For the case of PECVD deposited amorphous silicon, the substrate deposition temperature was adjusted from 150 °C to 300 °C producing a-Si thin films ranging from 159 MPa tensile to -152 MPa compressive respectively. Stress free PECVD amorphous silicon was obtained with a substrate temperature of 225 °C.

The second set of candidate materials explored for bistable MEMS structures involved Invar and titanium tungsten (TiW) thin films deposited using sputtering. With these materials, the sputtering pressure was adjusted to determine its effect on intrinsic stress. For the case of Invar thin films, the sputtering pressure was adjusted from 2 mTorr to 5 mTorr. This produced Invar thin films ranging from 500 MPa tensile to 1000 MPa tensile respectively. As seen from those data, we were unable to produce compressive Invar thin films by adjusting the sputter pressure. Since the ability to tune in compressive stress is a necessary characteristic for fabricating bistable mechanical structures, a second deposition parameter was added to the design matrix, namely the substrate bias. The above experiment was repeated with a 20W substrate bias and successful results were obtained. With a 20W substrate bias, -1600 MPa compressive Invar thin films were achieved at 2 mTorr and 300 MPa tensile films were produced at 5 mTorr. Stress free Invar thin films were produce at 3 mTorr using the 20W substrate bias. In general, the addition of substrate bias caused the deposited thin films to become more compressive. Elementary analysis of the sputtered Invar thin films showed that their material composition was slightly different from the bulk Invar sputter target. The sputtered thin films were 55% Fe, 41.5% Ni and 3.5% O while the original bulk sputter target was 64%

Fe and 36% Ni. Although slightly different in composition, the coefficient of thermal expansion (CTE) of the sputtered invar thin film (1.38 ppm/C) compared very favorably with that of bulk invar (1.2 ppm/C). With its experimentally characterized low CTE, this part of the research demonstrated that sputtered invar thin films from bulk invar targets were excellent candidate materials for the “passive” layer (i.e. low CTE layer) in bistable MEMS thermal sensors and actuators.

The same procedure that was used to deposit Invar thin films was also used to deposit sputtered TiW (titanium tungsten) thin films. For the case of titanium tungsten thin films, the sputtering pressure was adjusted from 2 mTorr to 5 mTorr. This produced TiW thin films ranging from -300 MPa compressive to 1500 MPa tensile respectively. However, with bias we could further increase compressive stress from -1300 MPa to -2300 MPa. The addition of the substrate bias allowed compressive stresses to be tuned into the films, which is the basic requirement for thin film buckling when released.

The next part of this research explored different strategies and approaches for fabricating three-dimensional (3D) non-planar structures using minimal processing steps. This is especially important when using stress free thin films to produce bistable MEMS structures. In this case, one cannot rely on the intrinsic compressive stress of released films to produce non planar structures. Instead, one needs to create a 3D non-planar “template” and deposit the stress free materials on top of it directly. The first approach explored used thermal/chemical reflow of photoresist from traditional single mask binary lithography to produce non-planar structures. It was experimentally determined that thermal-only reflow was adequate for producing hemispherical domes as long as the dome diameter was less than 400 μm . For larger diameter domes, which is typically

required for bistable MEMS, a combination of chemical and thermal reflow was needed. In this case, we investigated chemical reflow by exposing the developed resist to NMP vapor for 2-4 minutes followed by thermal reflow at 150 °C for one hour on a hotplate. It was shown that the two minute NMP vapor exposure was preferred for dome diameters up to 500 μm , three minutes for diameters up to 700 μm , and four minutes for diameters up to 1100 μm .

The second approach for producing 3D dome-shaped templates involved maskless grayscale lithography. 3D micro-structures were designed using SolidWorks, converted to a grayscale mask file by custom software, and fed into a Heidelberg 66FS Laser Pattern Generator (LPG) to selectively expose resist. AZ 4620 photoresist was fully characterized in this part of the research and shown to be an excellent candidate material for producing the hemispherical domes required for bistable MEMS, along with a wide variety of other demonstrated 3D non-planar structures.

The final phase of this research focused on fabricating several bistable dome-shaped diaphragms and determining if it was possible to switch their mechanical state thermally. Three different types of MEMS-based diaphragms were studied: oxide-polyimide diaphragms, oxide-aluminum diaphragms, and oxide-aluminum-polyimide diaphragms. In all cases, the compressive stress in the thermally-grown oxide layer was engineered to cause the released films to buckle. However, due to the thin oxide's fragile nature, it was determined that a stress free structural layer was needed to produce nice uniform hemispherical domes. Polyimide was shown to be an excellent candidate material for the structural layer. Arrays of oxide-polyimide bilayer domes with diameters ranging from 100 μm to 700 μm were fabricated and found to be mechanically bistable. Relatively

thick released aluminum was also investigated as the structural layer in place of polyimide. However, it was determined to be unsuitable for this application because the aluminum thin films became even more compressive with increasing temperature, resulting in fragile and wrinkled patterns on the diaphragms. Therefore, polyimide was ultimately selected as the structural layer. Although thick aluminum was found to be unsuitable as the structural layer, thin aluminum (i.e. 0.30 μm) with its mismatched CTE was found to be effective as the thermal actuating force as long as the temperature was limited to 150 $^{\circ}\text{C}$ which is the limit of its elastic region. It was shown that aluminum films became tensile after exposure to temperatures above 150 $^{\circ}\text{C}$ and suffered from irreversible deformation, making them ineffective as thermal actuators.

Therefore, the final design for the dome-shaped thermal actuators consisted of an oxide-polyimide diaphragm (0.45 μm oxide, 1.7 μm polyimide) uniformly coated with a thin layer of aluminum (0.30 μm). Arrays of these tri-layer diaphragms were created ranging in diameter from 100 μm to 700 μm . All devices were thermally tested and only the 400 micron diaphragms successfully changed state with temperature. Approximately 50% of the 400 μm diameter oxide-aluminum-polyimide diaphragms switched their states from buckled down to buckled up with temperature. The transition occurred between 100 $^{\circ}\text{C}$ to 110 $^{\circ}\text{C}$. Analytical modeling using equations predicted a transition temperature of 44 $^{\circ}\text{C}$. Although it was possible to thermally actuate these devices once, it was found that they would not thermally actuate a second time.

In summary, we demonstrated that it was possible to form bistable dome-shaped diaphragms using a) oxide-polyimide, b) oxide-aluminum, and c) oxide-aluminum-polyimide. All of these devices demonstrated mechanical bistability at room

temperature. With all three combinations of diaphragm materials, we experimentally found that there were two distinct regions of operation. All the structures with diameter from 300 μm to 700 μm were truly bistable and would remain in their 2nd state when mechanically switched using vacuum and then released. However, when the diameter was reduced to less than 250 μm , the structures were no longer bistable and would return back to their original state once the vacuum was removed. This research also introduced a new qualitative parameter called the “dome factor”, which was the ability of the structure to form an unwrinkled uniform buckled dome upon its release. We experimentally determined that the dome factor was directly dependent upon the thickness of the aluminum film deposited on the highly-compressive oxide diaphragm. Finally, an analytical equation (Eq. 4.20) was developed to model the initial buckling height of the bi- and tri-layer diaphragms, and those analytical predictions agreed well with the experimental results.

5.2 Recommendations

While future research can be extended to include other material systems for fabricating mechanically bistable structures, the trilayer diaphragm consisting of oxide-aluminum-polyimide showed great promise, especially with the 400 μm diameter domes. Some of the difficulty in thermally actuating the other diameter domes and the fact that our experimental switching temperature was a factor of ~ 2 larger than the predictions might be attributed to the fact that the aluminum was coated everywhere on the wafer, including in the critical perimeter regions where the diaphragms connect to the support structures. The highly compressive aluminum material in these regions may require a higher temperature to switch states. Literature described a similar behavior for Al/Si, clamped,

bimetallic beams where the sides and ends of the beams were free of aluminum [56, 75]. In that case, the upward deflection of the beam nearly doubled by removing the aluminum in the compressed areas. Therefore, one recommendation is that the aluminum film be patterned so that there is no aluminum along the diaphragm edges, as shown in Figure 5.1. The disadvantage of this recommendation is that it requires an additional photomask and more processing.

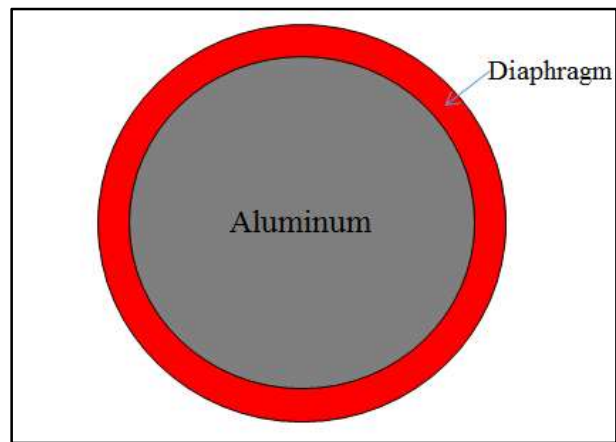


Figure 5.1. Patterned aluminum on the diaphragm.

REFERENCES

- [1] J. Bryzek. (2013, Roadmap for the Trillion Sensor Universe. [Presentation].
- [2] W. C. Hu, "An investigation of Switching Behaviors of Bimetallic-Disk Thermostats," 30 th of June 1978.
- [3] S. G. J. M. Timoshenko, *Theory of elastic stability*. New York: McGraw-Hill, 1961.
- [4] W. H. W. W. H. M. D. M. B. W. R. Wittrick, "STABILITY OF A BIMETALLIC DISK," *Q J Mechanics Appl Math The Quarterly Journal of Mechanics and Applied Mathematics*, vol. 6, pp. 15-31, 1953.
- [5] C. Ucke and H. Schlichting, "Revival of the jumping disc," *Physics Education*, vol. 44, p. 612, 2009.
- [6] K. Gi-Woo and K. Jaehwan, "Compliant bistable mechanism for low frequency vibration energy harvester inspired by auditory hair bundle structures," *Smart Materials and Structures*, vol. 22, 2013.
- [7] "The smallest chemical reaction system with bistability," *BMC Systems Biology*, vol. 3, 2009.
- [8] M. A. Huff, A. D. Nikolich, and M. A. Schmidt, "A threshold pressure switch utilizing plastic deformation of silicon," in *Solid-State Sensors and Actuators, 1991. Digest of Technical Papers, TRANSDUCERS '91., 1991 International Conference on*, 1991, pp. 177-180.

- [9] B. Ando, S. Baglio, G. L'Episcopo, and C. Trigona, "Investigation on Mechanically Bistable MEMS Devices for Energy Harvesting From Vibrations," *Microelectromechanical Systems, Journal of*, vol. 21, pp. 779-790, 2012.
- [10] D. S. Popescu, D. C. Dascalu, M. Elwenspoek, and T. Lammerink, "Silicon Active Microvalves Using Buckled Membranes For Actuation," in *Solid-State Sensors and Actuators, 1995 and Eurosensors IX.. Transducers '95. The 8th International Conference on*, 1995, pp. 305-308.
- [11] A. Nisar, N. Afzulpurkar, B. Mahaisavariya, and A. Tuantranont, "MEMS-based micropumps in drug delivery and biomedical applications," *Sensors and Actuators B: Chemical*, vol. 130, pp. 917-942, 2008.
- [12] B. J. Hansen, C. J. Carron, A. R. Hawkins, and S. M. Schultz, "Zero-power shock sensors using bistable compliant mechanisms," 2007, pp. 65251W-65251W-8.
- [13] B. Halg, "On a micro-electro-mechanical nonvolatile memory cell," *Electron Devices, IEEE Transactions on*, vol. 37, pp. 2230-2236, 1990.
- [14] E. Chan, K. Garikipati, and R. Dutton, "Complete characterization of electrostatically-actuated beams including effects of multiple discontinuities and buckling," *Proc. Modeling Simulation Microsyst*, pp. 194-197, 1999.
- [15] T. Lisee, S. Hoerschelmann, H. Quenzer, B. Wagner, and W. Benecke, "Thermally driven microvalve with buckling behaviour for pneumatic applications," in *Micro Electro Mechanical Systems, 1994, MEMS'94, Proceedings, IEEE Workshop on*, 1994, pp. 13-17.

- [16] Y. Zhu and J. W. Zu, "Enhanced buckled-beam piezoelectric energy harvesting using midpoint magnetic force," *Applied Physics Letters*, vol. 103, p. 041905, 2013.
- [17] M. McCarthy, N. Tiliakos, V. Modi, L. G. Frechette, C. International Mechanical Engineering, and Exposition, "Thermal buckling of eccentric microfabricated nickel beams as temperature regulated nonlinear actuators for flow control," *Sensors & Actuators: A. Physical*, vol. 134, pp. 37-46, 2007.
- [18] U. R. Gowrishetty, K. M. Walsh, and T. A. Berfield, "Fabrication of polyimide bi-stable diaphragms using oxide compressive stresses for the field of 'Buckle MEMS'," *J Micromech Microengineering Journal of Micromechanics and Microengineering*, vol. 20, 2010.
- [19] U. R. Gowrishetty, K. M. Walsh, and D. Jackson, "No-power vacuum actuated bi-stable MEMS SPDT switch," in *Sensors, 2010 IEEE*, 2010, pp. 1745-1749.
- [20] D. A. Porter, U. R. Gowrishetty, I. J. Phelps, K. M. Walsh, and T. A. Berfield, "Mechanics of Buckled Structure MEMS for Actuation and Energy Harvesting Applications," in *ASME 2012 International Mechanical Engineering Congress and Exposition*, 2012, pp. 49-54.
- [21] W. Kern, "The evolution of silicon wafer cleaning technology," *Journal of the Electrochemical Society*, vol. 137, pp. 1887-1892, 1990.
- [22] X. Feng, Y. Huang, and A. Rosakis, "On the Stoney formula for a thin film/substrate system with nonuniform substrate thickness," *Journal of Applied Mechanics*, vol. 74, pp. 1276-1281, 2007.

- [23] L. I. G. R. Maissel, *Handbook of thin film technology*. New York: McGraw-Hill, 1970.
- [24] J. K. K. O'Donnell, and R.S. Post, "Controlling Stress in Thin Films," 2002.
- [25] D. Ratnayake, M. D. Martin, U. R. Gowrishetty, D. A. Porter, T. A. Berfield, S. P. McNamara, *et al.*, "Engineering stress in thin films for the field of bistable MEMS," *Journal of Micromechanics and Microengineering*, vol. 25, p. 125025, 2015.
- [26] T. Hirano, L.-S. Fan, J. Q. Gao, and W. Y. Lee, "MEMS milliactuator for hard-disk-drive tracking servo," *Microelectromechanical Systems, Journal of*, vol. 7, pp. 149-155, 1998.
- [27] T. Hirano and L.-S. Fan, "Invar electrodeposition for MEMS application," 1996, pp. 252-259.
- [28] A. K. Dokania, B. Kocdemir, and U. Herr, "Thermal expansion of invar thin film for MEMS application," in *International Symposium of Research Students on Material Science and Engineering, Chennai, India*, 2004, pp. 20-22.
- [29] X. Feng, Y. Huang, H. Jiang, D. Ngo, and A. J. Rosakis, "The effect of thin film/substrate radii on the Stoney formula for thin film/substrate subjected to non-uniform axisymmetric misfit strain and temperature," *J. Mech. Mater. Struct.*, vol. 1, pp. 1041-1053, 2006.
- [30] D. Ratnayake and K. M. Walsh, "Invar thin films for MEMS bistable devices," in *SoutheastCon, 2016*, 2016, pp. 1-4.
- [31] N. e. A. Inc, "Invar," ed.

- [32] C. Chen-Kuei, T. Ming-Qun, T. Po-Hao, and L. Chiapyng, "Fabrication and characterization of amorphous Si films by PECVD for MEMS," *Journal of Micromechanics and Microengineering*, vol. 15, pp. 136-142, 2005.
- [33] Y. Xu, F. Fei, Z. Jin, and W. Yuelin, "Smooth Surface Morphology of Hydrogenated Amorphous Silicon Film Prepared by Plasma Enhanced Chemical Vapor Deposition," *Plasma Science and Technology*, vol. 11, p. 569, 2009.
- [34] A. International, *Standard test methods for measuring adhesion by tape test*. West Conshohocken, Pa. :: ASTM International, 2010.
- [35] Ansi, *Standard test method for peel adhesion of pressure-sensitive tape*. Philadelphia, PA, 2000.
- [36] M. Ohring, *The Materials science of thin films*. Boston [etc.]: Academic Press, 1991.
- [37] A. A. Volinsky, N. R. Moody, and W. W. Gerberich, "Interfacial toughness measurements for thin films on substrates," *Acta Materialia Acta Materialia*, vol. 50, pp. 441-466, 2002.
- [38] H. Shanks and L. Ley, "Formation of pin holes in hydrogenated amorphous silicon at high temperatures and the yield strength of a-Si: H," *Journal of Applied Physics*, vol. 52, pp. 811-813, 1981.
- [39] Y. Mishima and T. Yagishita, "Investigation of the bubble formation mechanism in a-Si: H films by Fourier-transform infrared microspectroscopy," *Journal of applied physics*, vol. 64, pp. 3972-3974, 1988.

- [40] Y. Fu, J. Luo, S. Milne, A. Flewitt, and W. Milne, "Residual stress in amorphous and nanocrystalline Si films prepared by PECVD with hydrogen dilution," *Materials Science and Engineering: B*, vol. 124, pp. 132-137, 2005.
- [41] T. Deschaines, J. Hodkiewicz, and P. Henson, "Characterization of amorphous and microcrystalline silicon using Raman spectroscopy," 2009.
- [42] M. Oikawa, K. Iga, T. Sanada, N. Yamamoto, and K. Nishizawa, "Array of Distributed-Index Planar Micro-Lenses Prepared from Ion Exchange Technique," *Japanese Journal of Applied Physics*, vol. 20, pp. L296-L298, 1981.
- [43] D. Xie, H. Zhang, X. Shu, and J. Xiao, "Fabrication of polymer micro-lens array with pneumatically diaphragm-driven drop-on-demand inkjet technology," *Optics Express*, vol. 20, pp. 15186-15195, 2012/07/02 2012.
- [44] N. Ph, R. Völkel, H. P. Herzig, M. Eisner, and S. Haselbeck, "Design, fabrication and testing of microlens arrays for sensors and microsystems," *Pure and Applied Optics: Journal of the European Optical Society Part A*, vol. 6, pp. 617-636, 1997.
- [45] H. Myung-Geun, P. Yoon-Jung, K. Seoung-Hoe, Y. Byueng-Su, and P. Hyo-Hoon, "Thermal and chemical stability of reflowed-photoresist microlenses," *Journal of Micromechanics and Microengineering*, vol. 14, pp. 398-402, 2004.
- [46] A. Emadi, H. Wu, S. Grabarnik, G. De Graaf, and R. Wolffenbuttel, "Vertically tapered layers for optical applications fabricated using resist reflow," *Journal of Micromechanics and Microengineering*, vol. 19, p. 074014, 2009.
- [47] D. Daly, *Microlens arrays*. London ;: Taylor & Francis, 2001.

- [48] D. V. Rosato, D. V. Rosato, M. G. Rosato, and D. V. Rosato, *Injection molding handbook*, 3rd ed. / ed. Boston :: Kluwer Academic Publishers, 2000.
- [49] Clariant, "AZ 400K Developer for AZ 4500 series," ed: MicroChemicals.
- [50] J. Loomis, D. Ratnayake, C. McKenna, and K. M. Walsh, "Grayscale lithography—automated mask generation for complex three-dimensional topography," *Journal of Micro/Nanolithography, MEMS, and MOEMS*, vol. 15, pp. 013511-013511, 2016.
- [51] H. INSTRUMENTS, "HEIDELBERG INSTRUMENTS DWL 66FS User Guide Part I," 2007.
- [52] U. Gowrishetty, K. Walsh, and T. Berfield, "Fabrication of polyimide bi-stable diaphragms using oxide compressive stresses for the field of 'Buckle MEMS'," *J. Micromech. Microeng.*, vol. 20, 2010.
- [53] E. P. EerNisse, "Stress in thermal SiO₂ during growth," *Applied Physics Letters*, vol. 35, pp. 8-10, 1979.
- [54] W. K. Schomburg and C. Goll, "Design optimization of bistable microdiaphragm valves," *Sensors & Actuators: A. Physical*, vol. 64, pp. 259-264, 1998.
- [55] W. K. Schomburg. (2011). *Introduction to microsystem design*. Available: SpringerLink <http://dx.doi.org/10.1007/978-3-642-19489-4>
- [56] R. Arya, M. Rashid, D. Howard, S. Collins, and R. Smith, "Thermally actuated, bistable, oxide/silicon/metal membranes," *Journal of Micromechanics and Microengineering*, vol. 16, p. 40, 2005.
- [57] X. Ding and et al., "A study on silicon-diaphragm buckling," *Tech. Dig. IEEE Solid-State Sensors and Actuators Workshop*, p. 128, 1990.

- [58] M. Morita, T. Ohmi, E. Hasegawa, M. Kawakami, and M. Ohwada, "Growth of native oxide on a silicon surface," *Journal of Applied Physics*, vol. 68, pp. 1272-1281, 1990.
- [59] R. Fondazione "Giorgio. (1976, Atti della Fondazione Giorgio Ronchi.
- [60] R. C. Jaeger, *Introduction to microelectronic fabrication*, 2nd ed. ed. Upper Saddle River, N.J. :: Prentice Hall, 2002.
- [61] Y. Murakami, T. Shiota, T. Shingyouji, and H. Abe, "Effect of oxidation ambient on the dielectric breakdown characteristics of thermal oxide films of silicon," *Journal of applied physics*, vol. 75, pp. 5302-5305, 1994.
- [62] B. El-Kareh, "Fundamentals of Semiconductor Processing Technology," ed. Boston, MA :: Springer US, 1995.
- [63] L. Filipovic, "Topography Simulation of Novel Processing Techniques," 2012.
- [64] G. Joyce, C. Moore, T. Perova, C. Beitia, A. Kocot, K. Berwick, *et al.*, "Structural Properties and Stress Analysis of SiO₂ Thin Films," 2000.
- [65] A. Szekeres and P. Danesh, "Mechanical stress in structures formed by thermal oxidation of amorphous and crystalline silicon," *Semiconductor science and technology*, vol. 11, p. 1225, 1996.
- [66] R. L. Hubbard, Z. Fathi, I. Ahmad, H. Matsutani, and T. Hattori, "Low temperature curing of polyimide wafer coatings," in *Electronics Manufacturing Technology Symposium, 2004. IEEE/CPMT/SEMI 29th International*, 2004, pp. 149-151.
- [67] H. MocoSystems, "PI-2600 Series-Low Stress Applications," 2009.

- [68] T. J. Kang, J.-G. Kim, H.-Y. Lee, J.-S. Lee, J.-H. Lee, J.-H. Hahn, *et al.*, "Modification of optical and mechanical surface properties of sputter-deposited aluminum thin films through ion implantation," *International journal of precision engineering and manufacturing*, vol. 15, pp. 889-894, 2014.
- [69] T. C. Hodge, S. A. Bidstrup-Allen, and P. A. Kohl, "Stresses in thin film metallization," *IEEE Transactions on Components, Packaging, and Manufacturing Technology: Part A*, vol. 20, pp. 241-250, 1997.
- [70] A. Sharma, F. M. Zaman, B. V. Amini, and F. Ayazi, "A high-Q in-plane SOI tuning fork gyroscope," in *Sensors, 2004. Proceedings of IEEE*, 2004, pp. 467-470 vol.1.
- [71] B. V. Amini, R. Abdolvand, and F. Ayazi, "Sub-micro-gravity capacitive SOI microaccelerometers," in *The 13th International Conference on Solid-State Sensors, Actuators and Microsystems, 2005. Digest of Technical Papers. TRANSDUCERS '05.*, 2005, pp. 515-518 Vol. 1.
- [72] R. Abdolvand and F. Ayazi, "An advanced reactive ion etching process for very high aspect-ratio sub-micron wide trenches in silicon," *Sensors and Actuators A: Physical*, vol. 144, pp. 109-116, 5/28/ 2008.
- [73] O. Ozsun, B. E. Alaca, A. D. Yalcinkaya, M. Yilmaz, M. Zervas, and Y. Leblebici, "On heat transfer at microscale with implications for microactuator design," *Journal of Micromechanics and Microengineering*, p. 045020, 2009.
- [74] O. Zohni, G. Buckner, T. Kim, A. Kingon, J. Maranchi, and R. Siergiej, "Investigating thin film stresses in stacked silicon dioxide/silicon nitride

structures and quantifying their effects on frequency response," *Journal of Micromechanics and Microengineering*, p. 1042, 2007.

- [75] P. J. Hesketh, H. G. Hughes, W. E. Bailey, and E. S. Meeting, *Proceedings of the Symposium on Microstructures and Microfabricated Systems IV*: Electrochemical Society, 1998.

CURRICULUM VITA

Dilan Ratnayake
Department of Electrical and Computer Engineering
University of Louisville
emailtodilan@gmail.com

SUMMARY

- An enthusiastic material scientist with extensive research experience in semiconductor microfabrication and MEMS/Microelectronics devices.
- Over 7 years of teaching experience with excellent assessments of my performance.

ACCOMPLISHMENTS

- **Designed and developed a process for grayscale lithography** to make **MEMS 3D structures**.
- Developed novel custom processing recipes to tune the **intrinsic stress in a-Si** using **PECVD** and obtain **sputtered highly compressive stress** on **TiW** and **Invar** thin films using **PVD 75** system.
- Developed processing recipes to **control the coefficient of thermal expansion (CTE)** in **co-sputtered Ni-Fe alloy** thin films using **PVD 75** system.
- Designed and simulated **buckled bistable bimetallic MEMS** temperature sensor.

EDUCATION

Ph. D., Electrical and Computer Engineering December 2016
University of Louisville, Louisville, KY USA
GPA 3.9/4.0

- Dissertation -” *STRATEGIES AND TECHNIQUES FOR FABRICATING MEMS BISTABLE THERMAL ACTUATORS*”

M. S., Physics May 2012
University of Louisville, Louisville, KY USA
GPA 3.6/4.0

B. S., Physics July 2009
University of Peradeniya, Peradeniya, Sri Lank

RESEARCH EXPERIENCE

Doctoral Candidate, Electrical and Computer Engineering Department Aug 2012-
Dec 2016

University of Louisville, Louisville, KY USA

- Designed and developed a process for grayscale lithography to make MEMS 3D structures to fabricate MEMS bi-stable devices and this process includes micro structure design using SolidWorks, converting to grayscale mask which is used in Heidelberg 66FS Laser Pattern Generator (LPG) and characterizing the photoresist and LPG parameters.
- Developed novel strategies and custom processing recipes to tune the intrinsic stress in amorphous silicon thin films from compressive to tensile (including stress free) using PECVD.
- Developed novel strategies and custom processing recipes to obtain sputtered highly compressive stress on TiW and Invar (alloy) thin films using physical vapor deposition (PVD 75).
- Developed processing recipes to control the CTE in co-sputtered Ni-Fe alloy thin films using PVD 75 system and characterized the stress on those films using a stress analyzer (Toho FLX 2320-S).
- Designed and simulated buckled bi-stable bimetallic MEMS temperature sensor using CoventorWare. Presently developing a fabrication process to prototype.

Internship: Research Engineer, Micro/Nano Technology Center May 2012 – Aug 2012

University of Louisville Louisville, KY

- Characterized the thermal oxidation growth and introduced new standard operating procedure for oxidation and maintenance and troubleshooting of oxidation furnace.
- Redesigned and developed a fabrication process for a graduate level fab class.

INSTRUMENT AND SOFTWARE EXPERIENCE

Technics 4604 sputtering system, KJL PVD75 sputtering system, Oxford PECVD PS100, Thermal oxidation furnace, Polyimide Yes Oven, Rapid thermal processor, SUSS Mask Aligner MA6/BA6, Heidelberg 66FS laser pattern generator (LPG), Deep reactive ion etching (DRIE), Trion metal etcher, Critical point dryer, Flimetrics thin film measurement, Veeco dektak profilometer, 4-Point probe, Zygo optical interferometer, Toho 2320-S stress analyzer, Zeiss axioskop optical microscope, Scanning electron microscope, EDAX, Atomic force microscope, Raman spectroscopy, L-Edit, CoventorWare, Comsol, SolidWorks, Silvaco, Matlab and Minitab.

TEACHING EXPERIENCE

Graduate Teaching Assistant, Electrical and Computer Engineering Department

Aug 2012 – Aug 2016

University of Louisville, Louisville, KY USA

- Managed a Senior/graduate-level laboratory courses in **microfabrication & MEMS**. Class met in a state-of-the-art class 100/1000 cleanroom at the University of Louisville.
- Students are provided with a hands-on cleanroom experience in various areas of microfabrication like oxidation, anneal, ion implantation, lithography, wet etching, dry etching (DRIE) and thin film deposition while fabricating different MEMS devices (Bulk Micromachining Piezoresistive Pressure Sensor, Accelerometer, Gyroscope, Flow sensor and actuator etc.).

Instructor for ECE252 (Introduction to Electrical Engineering), Electrical and Computer Engineering Department

University of Louisville, Louisville, KY USA

- Was responsible for the complete management of the class including course material, assignments, quizzes, tests and examinations as well as guiding and managing the graders.

Graduate Teaching Assistant, Department of Physics

Aug 2010 - May 2012

University of Louisville, Louisville, KY USA

- Conducted undergraduate general Physics laboratory classes and quiz classes.

PROFESSIONAL AFFILIATIONS

- **Volunteer Internship: Micro/Nano Technology Center** Jan 2012 - May 2012
University of Louisville, Louisville, KY USA
 - Updated the standard operating procedures (SOP's) of the cleanroom equipment.
 - Developed and implemented safety protocols.
- Member of IEEE and the editor of the Physical Society, University of Peradeniya, Sri Lanka.

MEETINGS AND PRESENTATIONS

- Oral presentation, “Invar thin films for MEMS Bistable Devices”, IEEE SoutheastCon, March 2016.
- Poster presentation, “*Three-dimensional micro-domes for MEMS using thermal and chemical reflow*” Research!Louisville, Louisville, KY, Oct 2015.
- Oral presentation, “*Experimental Micro/NanoTechnology Lab Class: Microfabrication of a MEMS Piezoresistive Pressure Sensor*”, 2013 Ky Nano Symposium, Louisville, KY, Aug 2013.

SCHOLARLY PUBLICATIONS

- **Dilan Ratnayake**, Michael D. Martin, Usha R. Gowrishetty, Daniel A. Porter, Thomas A. Berfield, Shamus P. McNamara and Kevin M. Walsh “Engineering stress in thin films for the field of bistable MEMS” published on JMM, November 2015.
- James Loomis, **Dilan Ratnayake**, Curtis McKenna and Kevin M. Walsh “Grayscale Lithography-Mask generation for complex 3D topography” published on Journal of Micro/Nanolithography, MEMS and MOEMS, March 2016.
- **Dilan Ratnayake**, and Kevin M. Walsh “Invar thin films for MEMS Bistable Devices” published on IEEE SoutheastCon 2016, March 2016.
- **Ratnayake, D.**; Dina Dasunata Arunallak, 2006, ISBN 955-99670-0-3, 529.3 DV 22. In this book I introduced a new calendar considering the correct revolution time of the earth.

ACHIEVEMENTS AND AWARDS

- The Graduate Dean's Citation Award, University of Louisville.
- Doctoral Dissertation Completion Award, University of Louisville.
- Graduate Teaching Assistantship, Department of Electrical and Computer Engineering, University of Louisville (August 2012 - August 2016)
- Graduate Teaching Assistantship, Department of Physics and Astronomy, University of Louisville (August 2010 - August 2012)